# High Resolution observations of spicules type II

Håkon Skogsrud
Master's thesis
Institute of Theoretical Astrophysics
University of Oslo
Norway


2010

# Acknowledgments

I wish to open this thesis by thanking all the individuals that made this thesis possible. Thank you Luc Rouppe van der Voort for giving me this fun and sometimes frustrating project, doing all the dirty work of preparing the datasets, patiently answering all my questions and for proofreading this manuscript a countless number of times. Thank you Bart De Pontieu for giving me your detection code which I learned a lot from. Thank you Benedikte for proofreading this manuscript, keeping me with company in the study hall, day and night, weekdays and weekends, and for pushing me to work when I'd rather do anything else than work. And thanks to the fellow students in the basement for all the non-physics conversations and movie nights.

# Contents

# Chapter 1

# Introduction

## 1.1 Introduction

Spicules are small, narrow and elongated structures that stick out above the edge of the solar disk as illustrated in Fig. 1.1. They are very dynamic and appear as jets that shoot out into the outer solar atmosphere. They were already observed before the 20th century (see e.g. Secchi, 1877) and the early literature is reviewed by Beckers (1968). Spicules were reported to show: successive upward and downward motion with apparent velocities of about 30 km/s, some disappearing at its maximum height, diameters of around 800 km, lifetimes between 8 and 15 minutes and typically occurring in magnetic regions outlining the solar super-granulation.

Because of their small physical sizes and relatively short lifetimes, it has been difficult to precisely characterize their properties and get a complete picture of the driving mechanisms. Up until recently, in the era before adaptive optics and advanced image post-processing techniques, variable seeing conditions and limited telescope aperture sizes did not allow for major advancement in the understanding of the nature of spicules. Limited observational constraints led to the proposition of a multitude of theoretical models, each with their own specific problems. For a review on theoretical models based on the traditional observational spicule literature, see Sterling (2000).

Major progress was made when Hansteen et al. (2006) and De Pontieu et al. (2007a) showed that active region dynamical fibrils exhibit the same dynamical evolution as spicules. The authors elaborated on a model proposed by De Pontieu et al. (2004) and combined high spatial and temporal resolution observations from the Swedish Solar Telescope (SST; Scharmer et al., 2003a)) along with numerical radiative magneto hydro-dynamic (MHD) simulations.

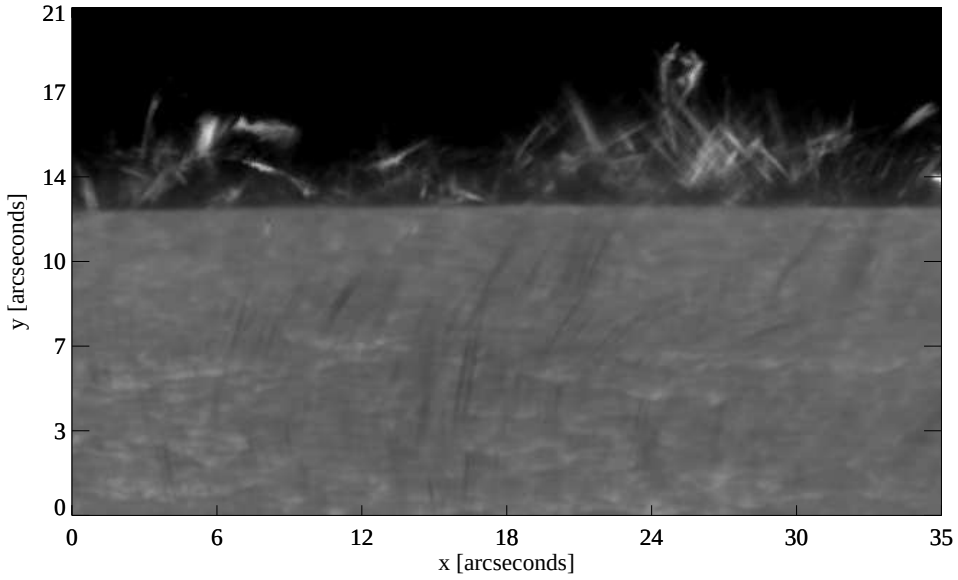


**Figure 1.1:** Image from the limb of the Sun in the H 6563 Å spectral line, henceforth called H$\alpha$. The image is taken at spectral position $-1.2$ Å from the line center through a narrow band filter. The type II spicules are the thin, elongated and bright structures off-limb. RBEs are the thin, elongated and dark features on-disk. The image is filtered to remove intensity gradients toward and off the limb.

The authors showed that the motion is driven by magneto-acoustic shocks generated by a variety of processes, such as leaking of waves into the chromosphere, convective buffeting, dissipation of magnetic energy and granular collapse. Langangen et al. (2008a) and Langangen et al. (2008c) showed from observations that the evolution of dynamical fibrils involves transport of plasma and Rouppe van der Voort et al. (2007) showed that a subset of quiet Sun mottles also have the same dynamical evolution. These on-disk phenomena are interpreted as the on-disk counterparts of the spicules.

The next major advancement came with the launch of the Hinode satellite (Kosugi et al., 2007) which incorporates the Solar Optical Telescope (SOT; Tsuneta et al., 2008). This telescope can study the chromosphere in the Ca II H 3968 Å line with a cadence down to around 5 s and spatial resolution of 0.16″. With a view unhampered by the turbulent atmosphere of the earth a new type of spicule was discovered. This new class of highly dynamic spicules was described by De Pontieu et al. (2007b) who label them as "type II" spicules, classifying the "classical" spicules as "type I" spicules.

The type II spicules were found to have the following properties: rapid formation in the order of 10 seconds, widths less than 200 km, lifetimes between 10 s and 150 s, apparent velocities of about 150 km/s and only

showing upward motion before rapidly fading from the observed passband in the order of 10 s. Before, spicules were studied with observations that typically had a cadence of about one minute. This means that this new type of spicule was missed in old observations due to the short lifetime and size often smaller than the resolution limit of the telescopes. With the knowledge of the Hinode time sequences, this new type of spicules could be traced back in earlier ground-based observations in Rutten (2007), using observations from the Dutch Open Telescope (DOT; Rutten et al., 2004), who called the type II spicules "straws".

Finding an on-disk counterpart of a phenomenon is very important as observations on-disk have much less line-of-sight superposition effects and it can help reveal the formation mechanism more easily than off-limb observations where the exact location of the root of the phenomenon is hard to determine. In search for the disk counterpart of type II spicules, Langangen et al. (2008b) investigated short-lived spectral asymmetries of the Ca II 8542 Å line. These events, or "rapid blue-shifted excursions" (RBEs), are a sudden widening of the line profile on only the blue side of the wing. These events were found to have the same dynamical evolution as spicules type II, and were suggested as the on-disk counterpart. For this study the authors used the Interferometric BI-directional Spectrometer (IBIS; Cavallini, 2006) mounted at the Dunn Solar Telescope.

IBIS is a tunable narrowband filter similar to the CRisp Imaging SpectroPolarimeter (CRISP) installed at the SST, a system using dual Fabry-Pérot interferometers as described by Scharmer (2006). Rouppe van der Voort et al. (2009) improved on the work by Langangen et al. (2008b) by using CRISP at the SST. Combined with the adaptive optics system at the SST (Scharmer et al., 2003b) and the image restoration technique Multi-Object Multi-Frame Blind De-convolution (MOMFBD; van Noort et al. (2005)) it was possible to obtain diffraction limited observations with high temporal and high spectral resolution. Rouppe van der Voort et al. (2009) studied the RBEs in both the H$\alpha$ line and Ca II 8542 Å line and established a firm connection between the off-limb spicules type II seen in Ca II H by Hinode and the RBEs observed on disk in H$\alpha$ and Ca II (8542 Å) lines. Their work provided detailed properties and gave important constraints to what the formation mechanism of these type II spicules can be.

Before 1939, the extremely high temperatures of the solar corona were not known. From the spectra of the Sun there was observed some unknown spectral lines that were thought to be from a new element, dubbed "coronium". Grotrian (1939), Edlén (1941) and Edlén (1942) showed that these lines came from many times ionized iron, suggesting a temperature in the corona of more than one million degrees. Why the temperature of the corona

is about 200 times hotter than the temperature in the photosphere has been a mystery for a long time and is commonly known as the "coronal heating problem". Today the problem revolves around how much the individual heating mechanism contributes to the heating of the corona. With the discovery of the supersonic solar wind described by Parker (1958) and the associated mass-loss from the Sun the detailed transport of mass in the solar atmosphere was beginning to be studied.

Spicules were quickly thought to play an important part in both the heating of the corona and in the mass transport. Pneuman & Kopp (1978) and Athay & Holzer (1982) studied the classical spicules as possible discrete coronal heating events. Withbroe (1983) estimated that the spicules could propel mass two orders of magnitude larger than the solar wind mass flux to coronal heights. However, a coronal counterpart of the spicules was not found and their role in heating the corona was dismissed as unlikely by Withbroe (1983). Recently De Pontieu et al. (2011) found direct evidence for a strong correlation between RBEs in the H$\alpha$ line observed by Hinode and brightenings in various transition region and coronal lines observed with the Atmospheric Imaging Assembly (AIA) on board the Solar Dynamics Observatory (SDO). The authors estimated that the mass transported to the corona is of the order of the solar wind mass loss and the energy transported to the corona is of the order that is required to sustain the energy lost from the active-region corona.

### 1.1.1 The Primary Thesis Goals

With the possible large contribution from spicules type II to the heating of the corona and their possible important role as mass carriers in the solar atmosphere, it is important to study the type II spicules in detail. This thesis will analyze two unique datasets observed with the SST in 2009 from the limb of the Sun. This was the first time the limb could be studied effectively with the SST and combined with CRISP, the SSTs adaptive optics system and the MOMFBD image restoration technique it was possible to obtain high spatial, spectral and temporal resolution at the same time.

This thesis will expand on the work of Rouppe van der Voort et al. (2009) from disk center and analyze RBEs close to the limb and spicules off-limb to provide more statistics on the properties of spicules type II. We define two primary goals (PG) for this thesis:

- PG1: check that the physical properties of the RBEs observed in the wings of H$\alpha$ from this thesis match the previously reported properties of RBEs.

- PG2: determine the type of the off-limb H$\alpha$ spicules seen in the H$\alpha$ spectral line wings.

The working hypothesis is: RBEs and off-limb spicules seen in the wings of H$\alpha$ are spicules type II.

### 1.1.2 Terminology

For simplicity, RBEs, type II spicules and the spicules off-limb seen in the line wings of H$\alpha$ are collectively referred to as "spicules".

### 1.1.3 Thesis Layout

The assumed reader of this thesis has a bachelor degree in astronomy.

- Chapter 2 gives a brief overview of the solar atmosphere and the tools used to obtain the observations analyzed in this thesis.
- Chapter 3 elaborates on the observations analyzed and explains in detail how the spicules were detected and how their properties were measured.
- Chapter 4 starts by showing examples of spicule motion seen in the observations and follows up with all the results. A discussion of previous articles that provide statistics spicules type II properties is given and at the end the results are interpreted and discussed.
- Chapter 5 contains the conclusion and suggestions for future observing campaigns.

# Chapter 2

# Background Material

## 2.1 The Atmosphere of the Sun

Like the atmosphere of the earth, the atmosphere on the Sun is artificially divided into several layers; the photosphere, the chromosphere, the transition region and the corona, each explained below. Figure 2.1 shows the temperature as function of height in the theoretical 1D VAL3C atmosphere (Vernazza et al., 1981).

### 2.1.1 The Photosphere

The photosphere is the innermost atmospheric layer situated on top of the convection layer. The photosphere is defined to range from 100 km below where $\tau_{500\text{nm}} = 1$ and up to about 525 km. The temperature at $-100$ km is about 9400 K[1] and the temperature at the top is about 4400 K. The photosphere is where the Sun turns from being opaque to being transparent at the continuum specter at 5000 Å, hence it is the furthest down in the solar atmosphere one can see in the visible spectrum. The general appearance of the Sun in the photosphere is a spotted background, Fig. 2.2, with some sunspots and pores sometimes visible.

The granulation pattern is the spotted background pattern seen in a continuum image. Bubbles of hot gas rise from the hotter convection layer, cool and expand, and the cool gas falls back down between the granules in what

[1] The temperatures and heights of the different atmospheric layers are taken from Ostlie & Carroll (1996).

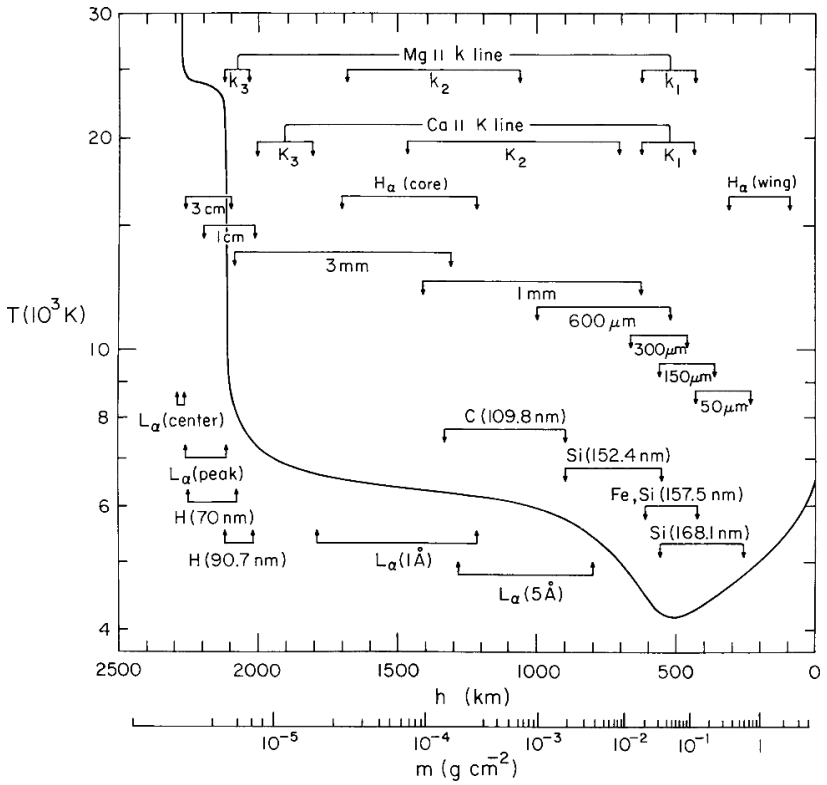


**Figure 2.1:** Temperature as function of height in the VAL3C 1D atmosphere model. The approximate formation region of H$\alpha$ is overplotted. The height scale is relative to where $\tau_{500\mathrm{nm}} = 1$. From Vernazza et al. (1981).

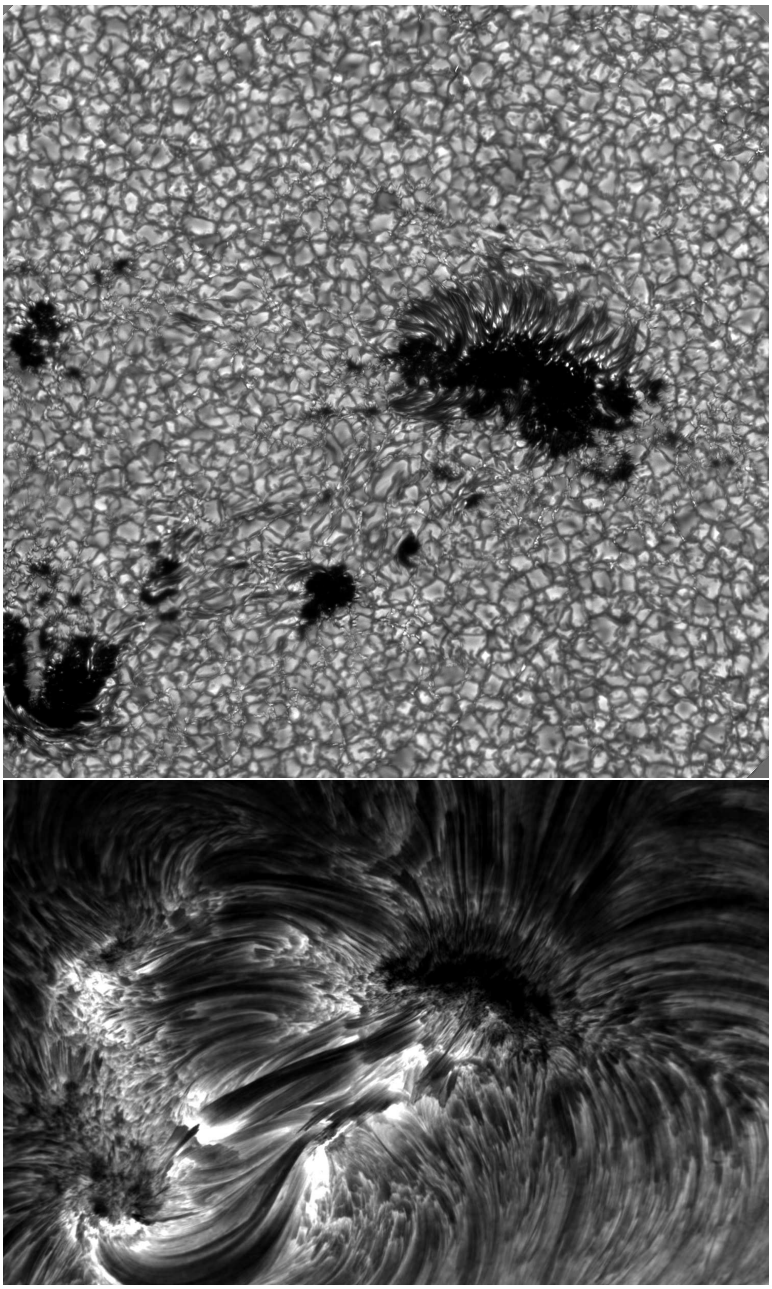

**Figure 2.2:** A group of sunspots and pores seen in the photosphere (top) and in the chromosphere (bottom). Top image: continuum image at 4264 Å. A sunspot with a partial penumbra is visible on the right and some smaller pores are visible to the left. Bottom: the fibrilar structures and regions of plage seen in H$\alpha$ line center. The image scale is about $80'' \times 80''$ for the top image top and about $80'' \times 50''$ for the bottom image. The images were taken at the SST on August 22, 2003, and were post-processed by Luc Rouppe van der Voort.

is called the intergranular lanes which appear slightly darker. The typical diameter of a granule is about 700 km.

Sunspots are much larger than a typical granule in size. They appear dark because strong magnetic fields rise up from the surface. Magnetic fields suppress the convection resulting in less efficient heat transfer. This reduces the temperature in the gas compared to the surrounding gas, and the sunspots appear darker as a result. The darkest center of a sunspot is called the umbra and the transition layer between the umbra and the granulation pattern is called the penumbra, on average brighter in appearance than the umbra, but darker than the granulation pattern. Pores are small sunspots lacking the penumbra.

Bright points appear as small bright points in the intergranular lanes. They are much smaller than a typical granule and are also caused by strong magnetic fields standing up from the surface.

### 2.1.2 The Chromosphere

The chromosphere (Figs. 2.2, 2.4 and 3.9) is positioned on top of the photosphere, extending approximately 1600 km upward (2100 km above $\tau_{500\mathrm{nm}} = 1$). The temperature is rising from 4400 K to about 10000 K at the top of the chromosphere. Easily visible in images from the chromosphere are the fibrils, filaments, spicules and plage regions. Fibrils are the dark and elongated features and the longest of the fibrils are called filaments. Large filaments when seen off-limb is called prominences. The bright areas, where the fibrils often are rooted are regions of plage which is the area in the chromosphere above the bright points. Spicules dominate the chromosphere when observing at the limb.

The fibrils form a "blanket" over the photosphere. This has the consequence that the chromospheric limb is located further out compared to the photospheric limb. Both the blanket and the line-of-sight confusion are illustrated in Fig. 2.4. The top panel is an image of the limb of the Sun at spectral position $-1.2$ Å from line center in H$\alpha$ showing spicules off-limb. The three next panels are from the same spatial position, but with the spectral position shifted closer to the line center in steps of 0.4 Å. For each spectral position closer to line center more fibrils become visible, and the spicules from the top panel are not possible to identify in the other panels. This happens because one sees through much more atmosphere along the line-of-sight direction. An illustration showing the different types of fibrils constituting the chromosphere is shown in Fig. 2.3. The fibrils are standing upright and forming a canopy spanning over larger regions, hence the term "blanket".

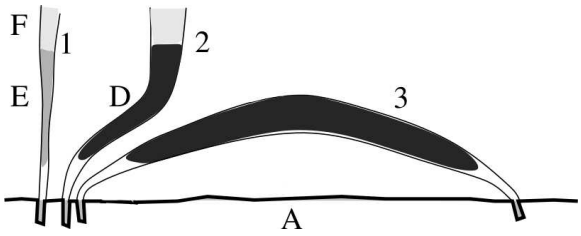


**Figure 2.3:** Different types of fibrils constituting the chromosphere. Rough temperatures: D$\sim 10^4$ K, E$\sim 10^5$ K and F$\sim 10^6$ K. A = The photosphere. Adapted from Rutten (2007).

### 2.1.3 The Transition Region and the Corona

The transition region is a thin layer, approximately 100 km thick, positioned between the chromosphere and the corona. The temperature rises from 10 000 K to approximately 100 000 K. In the corona, the temperature continue to rise until is exceeds one million degrees. The corona reaches out into space and has no well defined outer boundary.

## 2.2 The Swedish 1-meter Solar Telescope

The information about the SST and its most important optical systems are taken from Scharmer et al. (2003a), Scharmer et al. (2003b), Scharmer et al. (2003c) and Scharmer (2006). General telescope information is taken from Stix (2004).

The SST became operational in May 2002, and superseded the existing 50 cm Swedish Vacuum Solar Telescope (SVST), doubling the aperture diameter.

### 2.2.1 Location

The SST is located on the island of La Palma, Spain, outside the coast of Africa, see Fig. 2.5. The SST is run by the Institute for Solar Physics of the Royal Swedish Academy of Sciences and the SST is part of the observatory park Observatorio del Roque de los Muchachos operated by Instituto de Astrofísica de Canarias. Observatorio del Roque de los Muchachos one of the best known location for solar telescopes, see for instance Ardeberg (1984) who discusses the location and climate of La Palma in detail with respect to image quality.

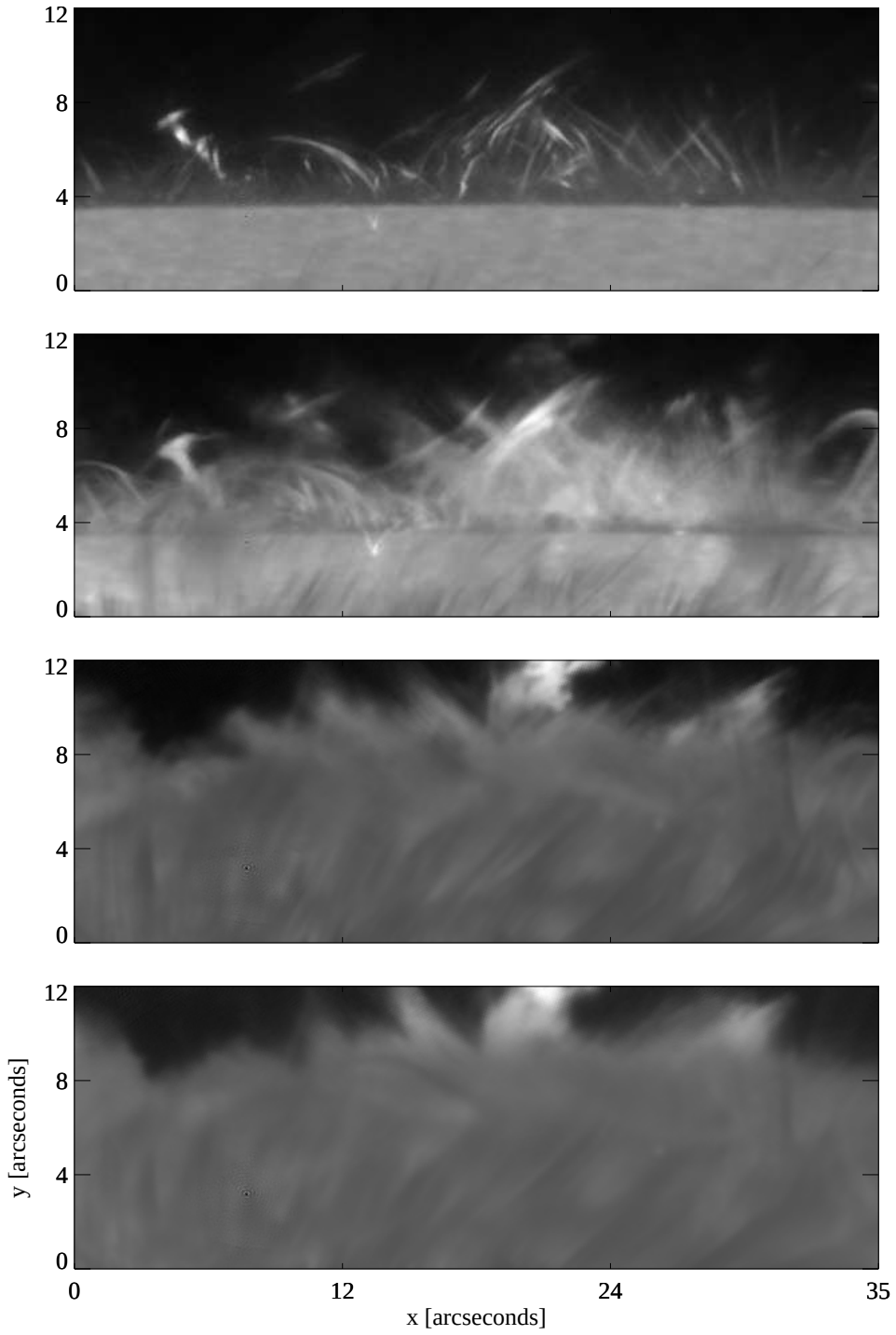


**Figure 2.4:** Four cutouts from the blue-wing at spectral position showing the chromospheric "blanket" at $-1.2$ Å, $-0.8$ Å, $-0.4$ Å and 0.0 Å from line center, respectively. The cutouts are at the same spatial position and the images are filtered to remove gradients toward and off the limb.

### 2.2.2 Seeing

Seeing is the degradation of the image quality due to atmospheric turbulence that causes changes in the diffraction index in the light path. In everyday language, one talks about good and bad seeing. Good seeing means that the atmospheric conditions are favorable with little degradation of the image quality while bad seeing means the opposite. The primary sources for atmospheric distortions are turbulence high up in the troposphere, and turbulence close to the telescope, arising from heating of the ground and the telescope itself by the Sun. The choice of the location for a telescope is important to counter the turbulence in the atmosphere. On La Palma, the steady trade winds from the ocean ensure that the flow of air is more laminar, and since La Palma is the north-west most of the Canary islands the airflow is not disrupted by the other islands. To counter the local convection, arising from heating of the ground around the telescope and the telescope itself, it is advantageous to elevate the telescope at least 15 meters above the ground. The telescope building on the SST and the ground around it is painted white to deflect heat.

Even in very good seeing the image quality is noticeable degraded by the atmosphere. The adaptive optics (AO) system installed at the SST is designed to compensate, in real time, for atmospheric turbulence. The principle behind the AO system is to expand the incoming wave front into Karhunen-Loève (KL) functions and use a deformable mirror to correct for as many of the lowest order KL-coefficients as possible. The KL functions are orthogonal and defined on a unit circle. The lowest order functions corresponds to pure focus, coma, astigmatism and spherical aberrations (see e.g. Scharmer et al., 2003b).

### 2.2.3 The Vacuum Tower

An image of the vacuum tower at the SST, with the positions of some of the main optical systems marked, is shown in Fig. 2.6. The SST is a tower telescope with the primary lens being positioned about 15 m meters above ground level. A high tower is advantageous as it makes it easier to accommodate the long focal length of the primary lens of 20.4 m and it elevates the lens above the local turbulence close to the ground. The tower is evacuated down to about 3 mbar to prevent turbulence arising inside the tower itself. The entrance window to the evacuated tower is the primary lens which has a diameter of 1 m. The pressure difference is taken into account for the shape of the primary lens. The lens is free of coma but has chromatic aberration. To obtain an achromatic image at primary a Schupman corrector is placed in the light path inside the tower.

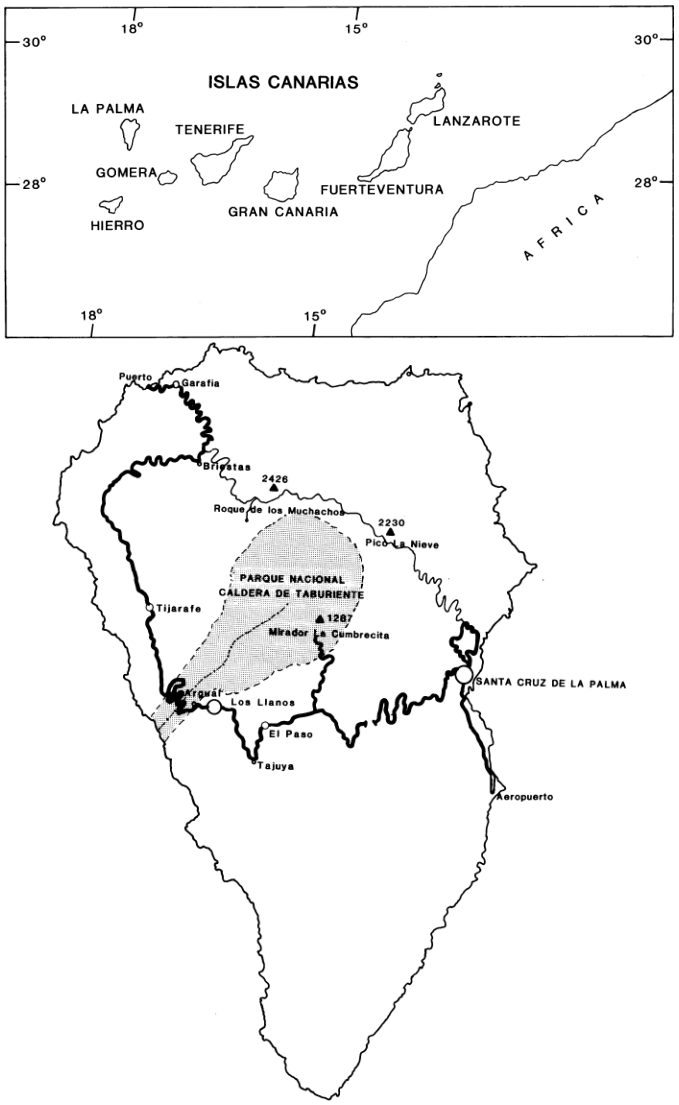


**Figure 2.5:** Top: map of the Canary Islands. On the axis are the longitudinal and latitudinal coordinates. Bottom: map of La Palma with the volcano crater "Caldera de Taburiente" is sketched in gray in the middle and the observatory park is marked with "Roque de los Muchachos". The thick and thin lines are the roads. From Ardeberg (1984).

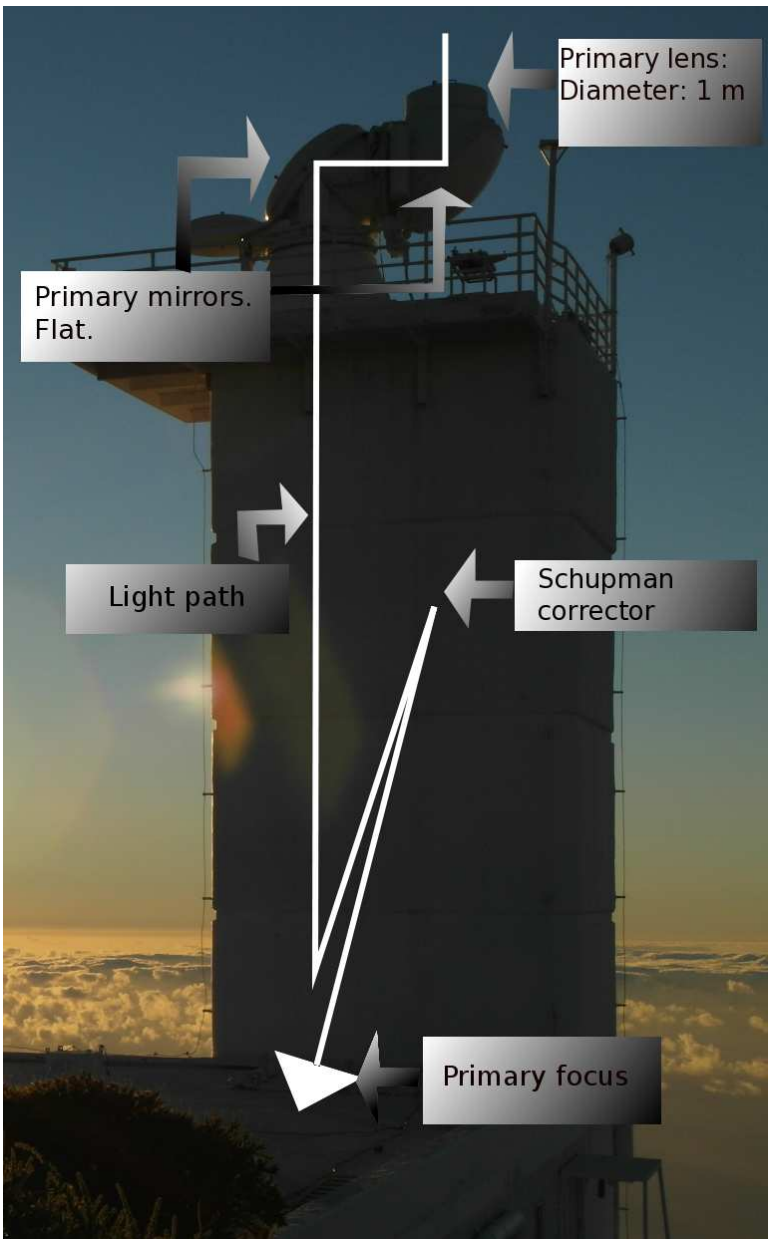


**Figure 2.6:** The vacuum tower of the SST on La Palma.

### 2.2.4 The Adaptive Optics System

The adaptive optics (AO) system is designed for compensating for the seeing. The AO is positioned outside the evacuated tower, after the primary focus, on the optical table. A small portion of the light received is diverted and sent through a Shack-Hartmann sensor, that consists of an 2D array of lenses focusing the light onto a CCD-sensor. Each of the small lenses creates an image and from the displacement of these images, due to atmospheric turbulence, it can be computed how the wave front is distorted. This information is passed onto a 37-electrode bi-morph mirror that changes shape 50 times per second to correct for the KL coefficients. The deformable mirror is positioned in the path of the light.

When the AO system can correct for many KL-coefficients one says that the AO is locking. The AO system only works well if the seeing is fairly good and cannot compensate for bad seeing.

After the AO system the light is sent to a dichroic beam splitter separating light into a red and blue beam. The red beam is sent into CRISP.

### 2.2.5 CRISP

CRisp Imaging SpectroPolarimeter (CRISP), Fig. 2.7, is a dual Fabry-Pérot interferometer (FPI) installed at the SST in 2008 that also can perform polarimetric observations of the Stokes parameters. The FPIs works as a tunable narrowband filter, and can shift the transmitting wavelength passband to a new spectral position in less than 0.25 s. For H$\alpha$ the full width at half maximum (FWHM) to the transmission profile is 6.6 pm.

In CRISP the light first passes through an optical chopper which synchronizes the three fast, low-noise CCD-cameras. One camera is located just after the filter wheel, referred to as the wide-band channel, and the remaining cameras are located after the FPIs. The cameras operate at a frame rate of 35 frames per seconds and use an exposure time of 17 ms for each frame. The size of the sensors is 1024×1024 pixels. The filter wheel contains the prefilters which does the first selection of the transmitting wavelengths. For H$\alpha$ the FWHM of the prefilter is 0.49 nm centered around 6563.8 Å. After the prefilter the light passes through a beam splitter which sends a portion of the light to the wide-band channel camera, and the remaining light is sent through the liquid crystals before the FPIs performs the interferometry. The liquid crystals are used when performing polarimetric observations and they remained unused for the observations in this thesis. The last optical system

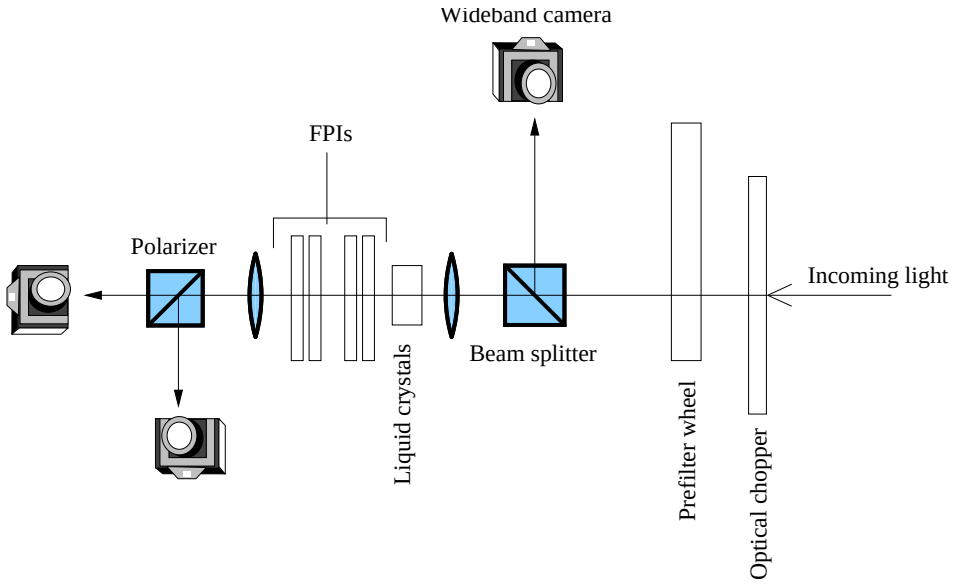


**Figure 2.7:** Schematic setup of CRISP.

the light passes is a polarizing beam splitter and the two beams are recorded on separate cameras.

### 2.2.6 MOMFBD

The setup of the AO system and CRISP are optimized for the image restoration technique Multi-Object Multi-Frame Blind De-convolution (MOMFBD) explained in van Noort et al. (2005) and van Noort & Rouppe van der Voort (2008).

Multi-object refers to the different images recorded on the three cameras due to differences in the optical setup in the light path before each camera. If three cameras are used as shown in Fig. 2.7, this translates into three "objects". Multi-frame means that 8 frames are recorded during which the Sun in the FOV is assumed to remain unchanged. Blind de-convolution refers to the image restoration technique used to determine the appearance of the FOV unaltered by both atmospheric seeing and the optical equipment. The word "blind" means the unaltered appearance of the Sun is unknown in the de-convolution process along with the degradation caused by the seeing.

Each CRISP scan is individually MOMFBD-restored the following way: the Sun is assumed to remain unchanged during the scan. Many images are recorded at each spectral position, and between each image the seeing changes but not the Sun. Due to the optical chopper, the images recorded

on the different cameras are subjected to equal seeing effects. This means one has 8 images of the same scene that are distorted differently by the variable seeing. All images are then split into many overlapping sub-images where the seeing is assumed to be the same for the entire sub-images. This is true if the sub-images are smaller in size than the isoplanatic patch. Blind de-convolution is applied to each of the sub images and in the end mosaicked into the full image. As a result of the restoration the narrowband images are aligned using the wideband image as 'anchor' image to ensure precise alignment.

The mounting of the telescope is the altitude-azimuth, alt-az, mounting which requires the adjustment of both the altitude and azimuth direction to follow the Sun across the sky. The alt-az mount combined with the earths rotation causes the Sun to rotate in the images as it crosses the sky. This rotation must be removed in the post-MOMFBD processing along with aligning of the individually MOMFBD restored CRISP scans.

# Chapter 3

# Methods

## 3.1 The Observations

The observations analyzed in this thesis are from May 10, 2009. It consists of two different datasets, different only in targeted area, duration and time acquired. The spectral line H$\alpha$ was scanned at 25 line positions, symmetric around the line center, with steps of 0.1 Å, yielding a total spectral range of $\pm$1.2 Å. A spectral profile of H$\alpha$ is plotted in Fig. 3.1 with plus signs marking the spectral positions of the CRISP scan. In terms of Doppler velocity this equals $\pm$55 km/s. The first dataset was observed between 08:50:12 - 09:37:15 UTC, having a duration of 47 minutes and 3 seconds, with a cadence of 6.4 s. The second dataset was observed between 09:38:06 - 10:15:07 UTC, having a duration of 37 minutes and 1 second, and the same cadence. The FOV was 59″×59″ with a pixel size of 0.0592 ″/pixel. A line scan is illustrated in Fig. 3.3 showing every second spectral line position in the first scan of the first dataset.

This was the first time one could effectively observe the limb with the SST. Before, the AO system could not lock on to features close to the limb. In the beginning of 2009 changes were made to the AO software which improved the overall performance. On the day of the observations, there was an active region close to the limb which provided many good targets for the AO system to lock on to. After observing the limb for 47 minutes the target area was moved further out to include more off-limb features while locking on faculae closer to the limb.

Both datasets were restored by Luc Rouppe van der Voort with the MOMFBD technique explained in section 2.2.6 and the images were aligned so that the limb was fixed in time. The datasets suffered from highly variable seeing

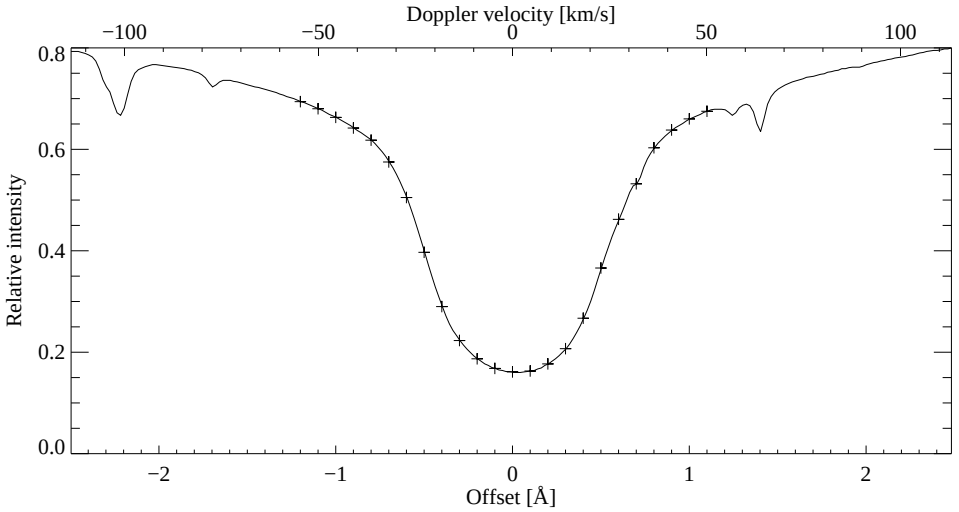


**Figure 3.1:** Average disk center intensity profile from the FTS (Neckel & Labs, 1984) atlas showing the H$\alpha$ spectral line with the CRISP scan positions marked with plus signs.

but the moments between the blurry frames have good seeing. The contrast is often used as a measure of the seeing and is defined as the standard deviation divided by the expectation value of a region. The disk-contrast for the two datasets is shown in Fig. 3.2 overplotted with asterisks that mark which frames that was discarded. 20 % of the time steps were discarded from the first dataset and 33 % from the second dataset.

The detection and measurements were performed on the images $\pm 1.2$ Å from line center. On these spectral positions the forest of chromospheric fibrils is less dense, which reduces the line-of-sight confusion and makes the spicules stand out more clearly (illustrated in Fig. 2.4, see also section 2.1.2) for more details. To ensure that no artifacts were introduced in the creation of the Doppler images, $\mathrm{Image}_{\mathrm{blue-wing}}$-$\mathrm{Image}_{\mathrm{red-wing}}$ , both the blue wing and red wing images were analyzed at every time step searching for frames with bad seeing. Images with insufficient seeing quality were discarded along with the corresponding image from the other side of the spectrum. The faint spicules on-disk close to the limb served as a visual measurement of the seeing. If they were difficult to distinguish from the background by eye that time step was discarded. This was a strict definition, but it was necessary to have the best possible input to the detection code. The images not discarded had good quality with many images close to the resolution limit of the telescope. The Rayleigh criterion is used as the definition of the resolution, and it is given as

$$\text{Angular resolution} = 1.22\frac{\lambda}{D} \approx 0.17 \text{ arcseconds} \tag{3.1}$$

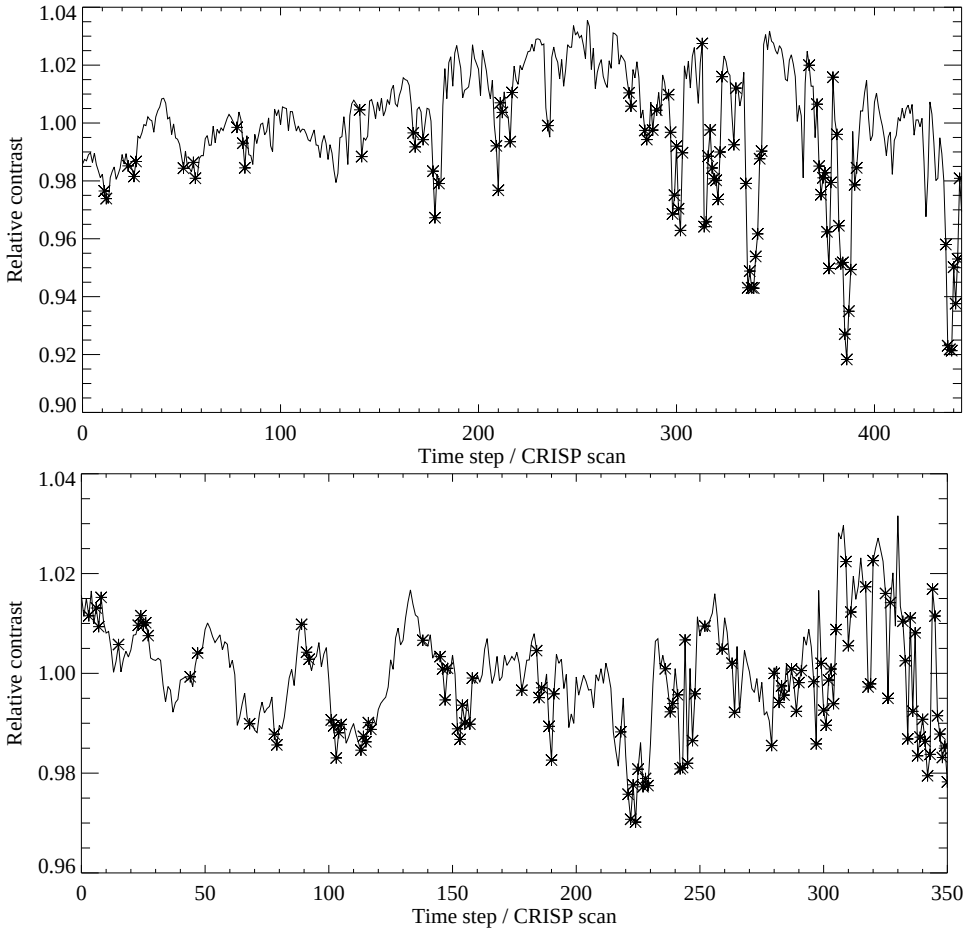


**Figure 3.2:** Disk-contrast of wide-band channel for the two datasets overplotted with asterisks marking which frames that were discarded. Top panel: the first dataset. Bottom panel: the second dataset.

where $\lambda$ is the wavelength and $D$ the aperture diameter.

The Sun was in a minimum of the activity cycle during the time of the observations and the targeted area was one of the rare regions with enhanced magnetic activity. The region included extended areas with bright faculae and a few pores. A few days later the region was classified as AR11017 by NOAA/USAF. The observed region was approximately located at the heliocentric coordinates $x_{\rm hel}, y_{\rm hel} \approx -900''$,$250''$.

## 3.2 The Detection Algorithm

The detection algorithm used in this thesis is developed by B. De Pontieu and was used to detect RBEs in Rouppe van der Voort et al. (2009). It is a threshold based detection which searches for thin, elongated areas with large gradients. The detection was performed on a wavelet transformed image where steep gradients are enhanced. Unwanted features in the background can effectively be eliminated by using the (unnormalized) Doppler image. Spicule edges are further enhanced by the wavelet transformation procedure. The detection was performed once for the negative values of the Doppler image and once for the positive values, so the sign of the Doppler signal was known at all times. The algorithm can be summarized as:

1. Create unnormalized Doppler image.
2. Apply threshold to attenuate the background signals.
3. Perform wavelet transformation to enhance edges.
4. Apply threshold: keeping only the values above the threshold.
5. Thin remaining regions to pixel lines.
6. Apply selection filters to discard short and curved lines.

Each step in the detection algorithm is illustrated in Fig. 3.5. In the figure, A is the blue-wing image and B the red-wing image. C is the Doppler image where only the positive values are shown. This image contains on-disk spicules that are blue-shifted and off-limb spicules that are red-shifted. D is the Doppler image with a threshold filter applied to dampen the Doppler signal from the background. E is the absolute value of the wavelet transformed image. A signal in this image means a gradient in the image above. F shows the wavelet transformed image with a threshold filter applied. G

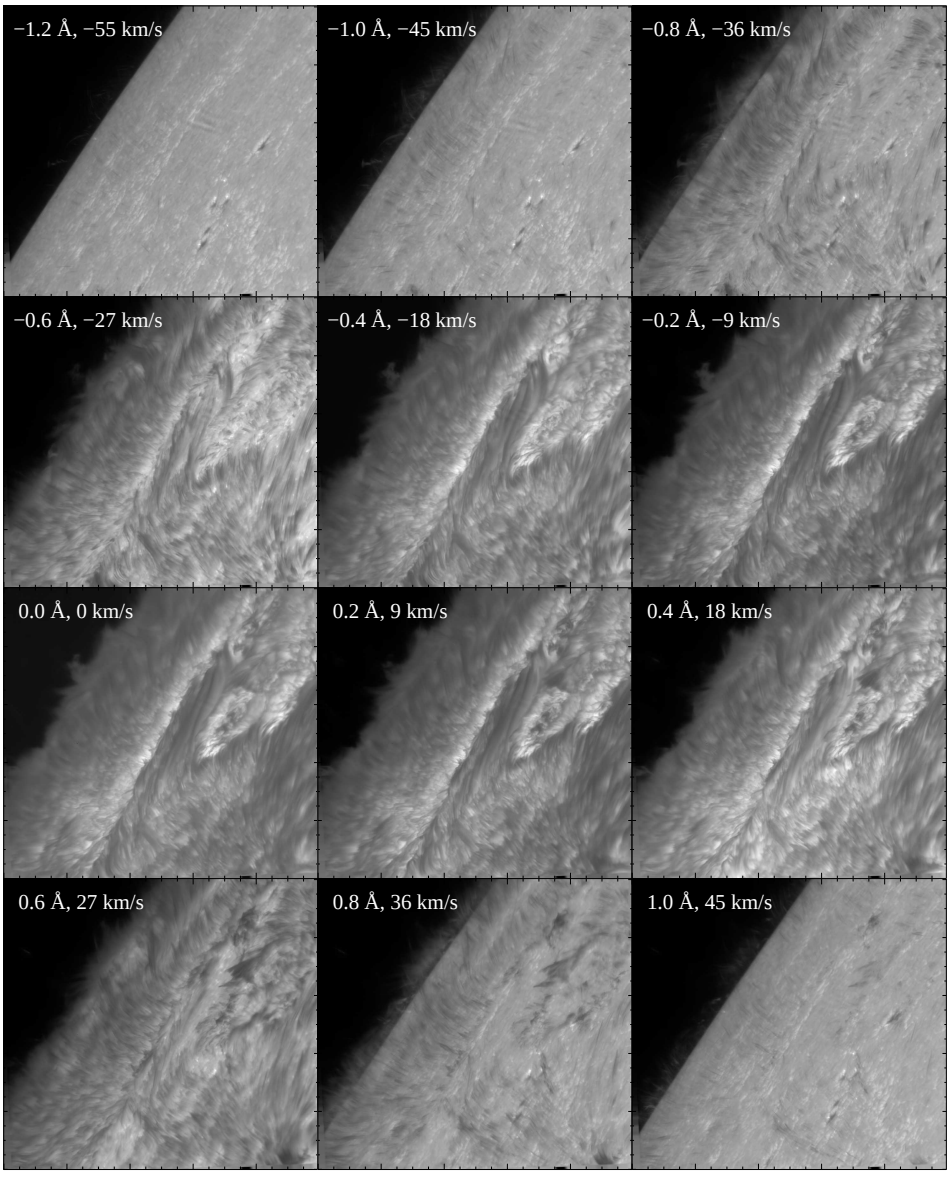


**Figure 3.3:** The first H$\alpha$ line scan of the first dataset. Every second spectral position is shown. The scan is shown in row-major order with the offset from line center and corresponding Doppler velocity printed in the upper left corner of each image. Each image is $59'' \times 59''$ in size.

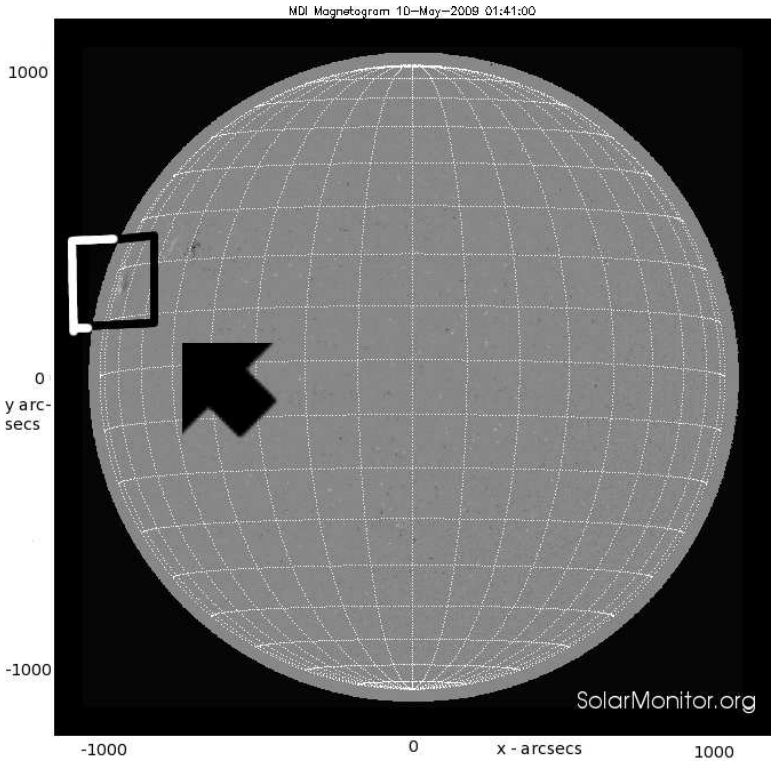


**Figure 3.4:** Full disk magnetogram of the Sun on the day of the observations. The magnetogram is taken by the Solar and Heliospheric Observatory (SOHO) and is provided by SolarMonitor.org. The image shows magnetic activity as a white and black signal. The square is the approximate position of the FOV for both datasets. The axis have heliocentric coordinates.

shows the features from the previous image thinned to pixel lines and in H all lines shorter than 15 pixels have been removed. In I, the too curved lines have been removed and the lines left are the detected spicules.

The unnormalized Doppler image was created as:

$$\text{Image}_{\text{blue-wing}} - \text{Image}_{\text{red-wing}}. \tag{3.2}$$

This unnormalized image is used rather than the normalized one:

$$\frac{\text{Image}_{\text{blue-wing}} - \text{Image}_{\text{red-wing}}}{\text{Image}_{\text{blue-wing}} + \text{Image}_{\text{red-wing}}}, \tag{3.3}$$

because in the latter, any features off-limb, no matter how faint, are scaled very close to 1 or $-1$. This amplification of faint signals was unwanted, and the easiest way around the problem was to perform the detection on the unnormalized image, henceforth called the Doppler image.

The wavelet transformation was the *á trous*-transformation which is described in detail, with references, in Starck et al. (1998). Briefly summarized, the transformation applies a blurring operator of varying degrees and subtracts the blurred images from one another. This has the effect of enhancing change in value, i.e. edges, and attenuates smooth areas because in a smooth area the pixel values are mostly unaffected by blurring.

Different thresholds were used on the negative part and on the positive part of the Doppler image. The blue-shifted part of the disk has much "Doppler-noise", i.e., Doppler-signatures from other phenomena and mechanisms than spicules. Because of this, the threshold was stricter for the negative part of the Doppler image. The difference in appearance is illustrated in Fig. 3.6 where the positive and negative values of the Doppler images are shown separately. In the lower image the disk appears in general much brighter and the background signals do not have the thin and elongated shape of a Doppler signal from a spicule.

Even though the background was mostly eliminated in the Doppler image, there were signatures left in the image that were not from spicules, but were detected as spicules. The regions where they most frequently occurred were masked out, and every detected feature inside one of those areas were discarded. The different regions masked out are shown in Fig. 3.7. The most typical reasons for masking out a region were coronal rain in the bottom right corner of both datasets, CRISP filter artifact in the middle of all images and persistent bright areas not in the typical spicular shape. It was only necessary to mask out regions for the positive values of the Doppler image. The stricter threshold on the negative values proved to be sufficiently effective to prevent non-spicules being detected as spicules.

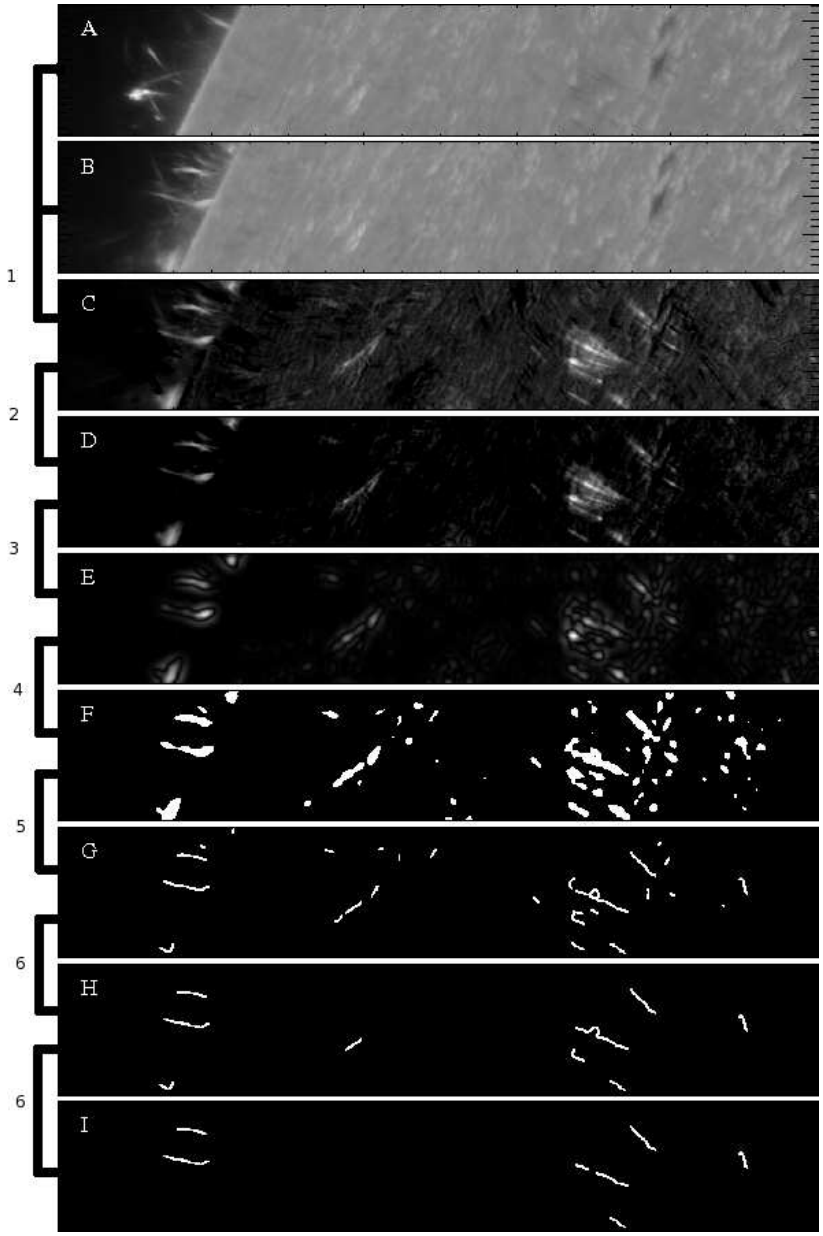


**Figure 3.5:** The detection algorithm explained visually. The numbers on the left side correspond to the steps in the detection algorithm in the text. A: Blue-wing image. B: red-wing image. C: the positive values of the Doppler image. D: C with threshold filter applied. E: wavelet transform applied to D. F: threshold applied to wavelet transformed image. G: F with regions thinned to pixel lines. H: removed lines shorter than 15 pixels. I: removed too curved lines. The lines left are the detected spicules. The images are a $59'' \times 9''$ cutouts and in G, H, and I the lines have been widened to three pixels to be more visible on paper.

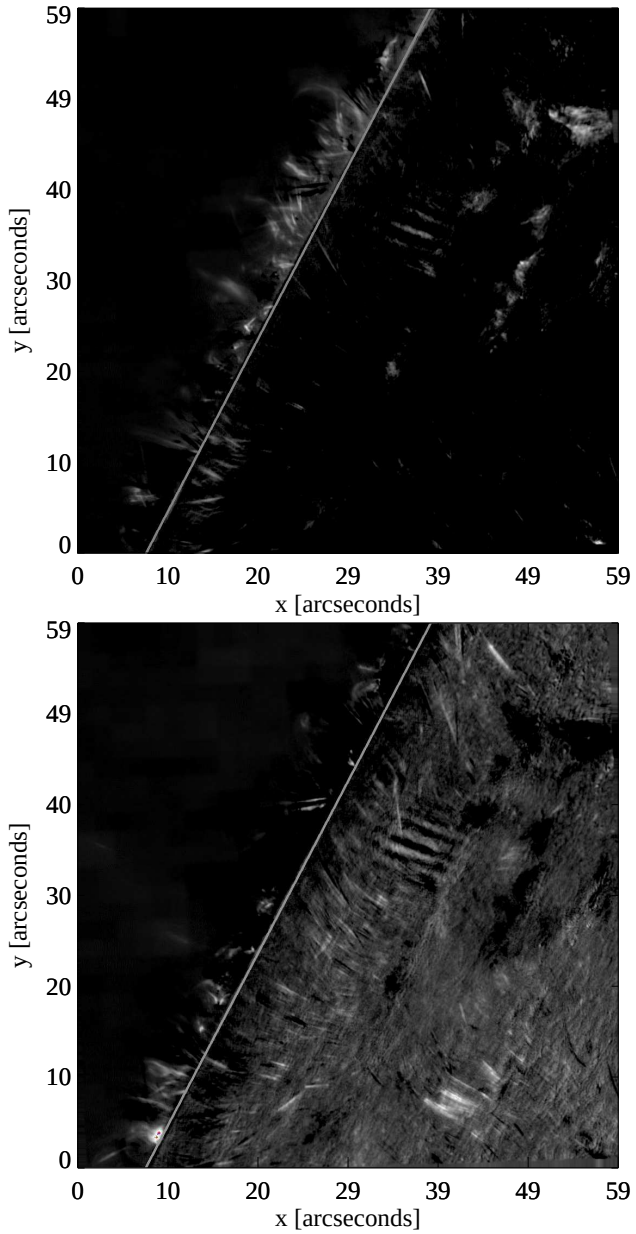


**Figure 3.6:** The positive values and the negative values of the unnormalized Doppler image shown on the top and bottom, respectively. The negative image has reversed color table. For both: black is zero Doppler signal and the straight, inclined line marks the approximate position of the limb. The disk is to the right of the limb. Top image: the off-limb features are blue-shifted and the on-disk features are red-shifted. Bottom image: the off-limb features are red-shifted and the on-disk features are blue-shifted. Both images are saturated at a lower value to more clearly show the features.

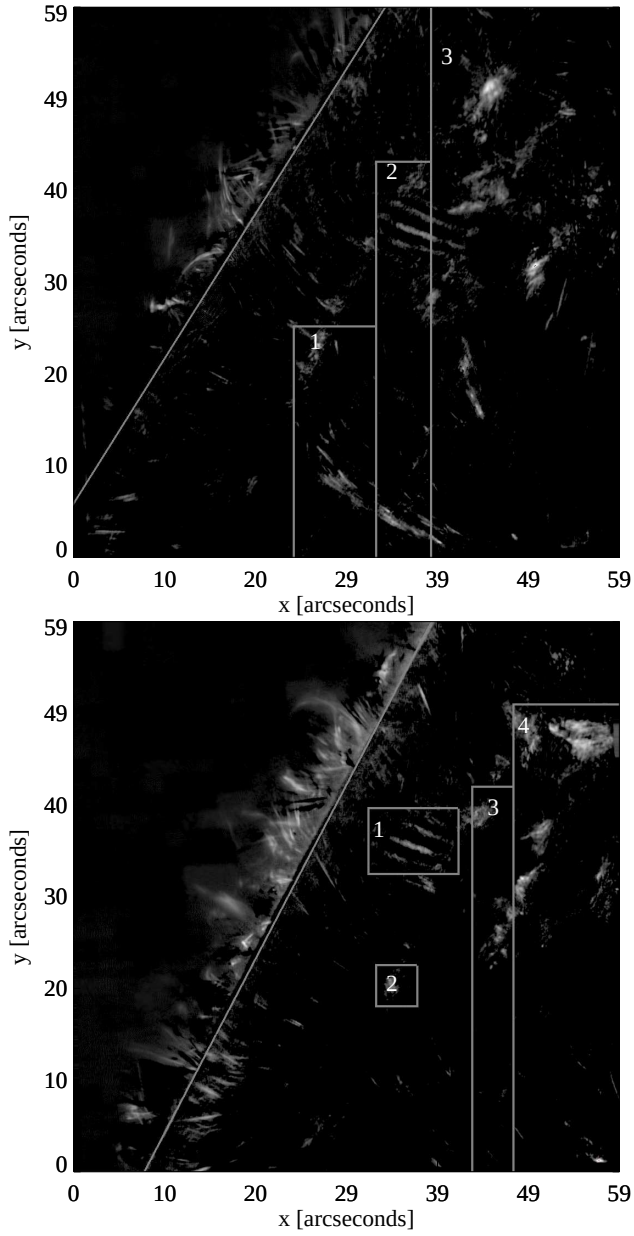


**Figure 3.7:** Masked out regions numbered for the first dataset on the top, and for the second dataset on the bottom. Only the positive values of the Doppler image are shown. Top image: the bottom part of regions 1, 2 and 3 removed regions with strong coronal rain. The top of region 2 removed a CRISP filter artifact and the top of region 3 removed areas with mostly non-typical spicule shape. Bottom image: region 1 removed the CRISP artifact artifact. Region 2 removed an area that was bright for extensive periods of time. Bottom of region 3 and 4 removed regions with strong coronal rain and the top of region 3 and 4 removed persistently bright areas that were not from spicules. Both images are saturated at a lower value to more clearly show the features.

To provide as unbiased statistics of the elongated features as possible, effort was made to apply only the most necessary selection filters, to filter out the unwanted features that were detected as spicules. A minimum length of 15 pixels and a maximum curvature of 90 degrees on the remaining pixel lines were imposed. The length filter removed lines from areas in the Doppler image that were not thin and long before the thinning was applied, but more circular or irregular in shape. The curvature filter removed primarily lines that started on one spicule and ended on another because of overlapping. The effect of these filters is shown in practice in the bottom images in Fig. 3.5. The length criterion of 15 pixels was the same criterion as used in Rouppe van der Voort et al. (2009) while the curvature criterion was added as an extra criterion. Attempts were made to split the line where it had a kink and only keep the segments with similar directions, but that did not work in many cases. In those cases it was difficult to distinguish between the overlapping features with visual inspection, and it was decided to discard the idea.

## 3.3 Obtaining the Spicule Spectra

In both datasets there was for every pixel, an H$\alpha$ spectrum sampled at 25 spectral positions. To isolate the spicule spectrum from the measured spectrum, it was assumed that the spicules were moving on top of a background profile, illustrated in Fig. 3.8, reminiscent of the cloud model (Beckers, 1964). To obtain an approximation of the spicule spectra one can subtract the background spectrum from the observed spectrum at every pixel position. In Rouppe van der Voort et al. (2009), the authors subtracted the spectrum averaged over the entire field of view. This worked well for their dataset where the authors targeted a coronal hole at disk center providing a relatively homogeneous solar scene. For regions with more spectral variation, such as sunspots, pores or close to the limb, a single spatially averaged profile is not a good approximation for the background spectrum in every pixel in the FOV. We were forced to adapt this method to cope with data close to and on the limb.

On both datasets, the images could be split into three parts with roughly equal visual appearance: off-limb, on-disk close to the limb and on-disk far from the limb, see Fig. 3.9. The average spectrum was computed differently for each of the three regions:

- Off-limb: the limb was assumed to be a linear inclined line. For each pixel distance from the limb, for instance between 3 and 4, an average

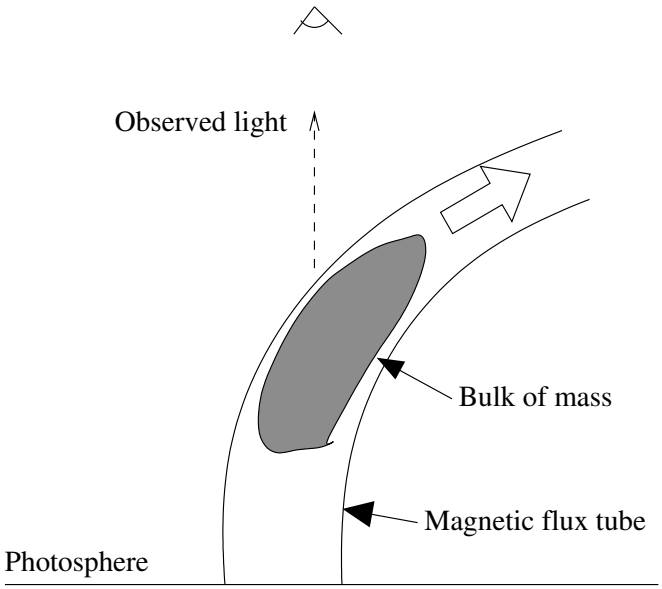


**Figure 3.8:** An illustration of the spicule moving on top of a background profile.

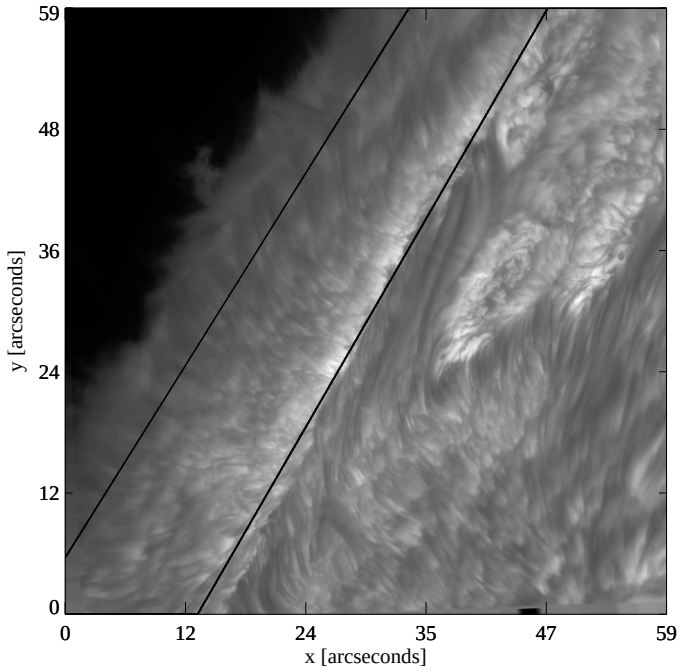


**Figure 3.9:** The three regions where the average spectrum was computed differently. The leftmost line marks the approximate position of the limb and the rightmost line separates two regions on-disk where the general direction of the fibrils are different. The image is from the blue wing of H$\alpha$ 0.3 Å from line center.

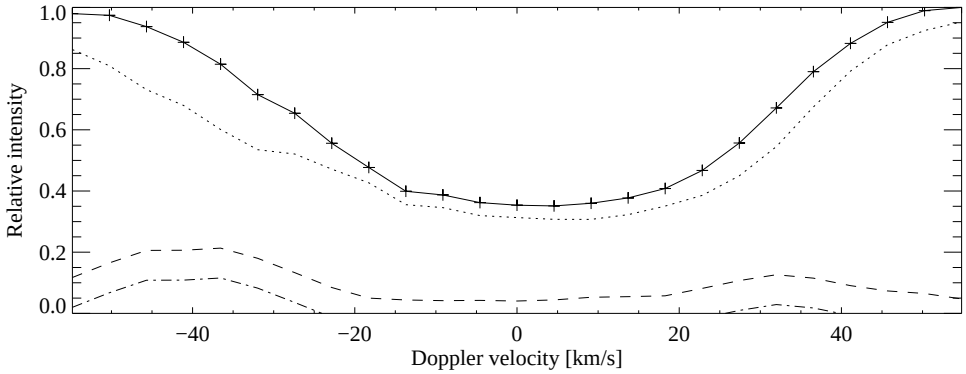


**Figure 3.10:** The effect of the limb darkening shown for a spicule with its middle pixel 77 pixels away from the limb. The solid line is the average spectrum computed for the region close to the limb on-disk, with the plus signs marking the CRISP spectral scan positions. The dotted line is the spectrum of the middle pixel in the spicule. The dashed line is the computed spicule spectrum and the dash-dot line is the spicule spectrum where the average of the spicule spectrum itself is subtracted. The computed Doppler width of the dashed line is 13.8 km/s and for the dash-dot line 7.1 km/s.

spectrum was computed including two distances closer to and two further out from the limb. This gave an average spectrum which was a function of the pixel distance from the limb. This was repeated for the first 10 time steps to obtain more pixels and thus a more accurate average. The average of these functions was computed and used as the average spectrum.

- On-disk close to the limb: the average spectrum was the average of all pixels between the approximation of the limb and the separation line on the disk. In addition, if the midpoint of the spicule was closer than 100 pixels to the limb, the average of the spectrum itself was subtracted. This was an attempt to correct for the limb darkening occurring close to the limb. The effect of the limb darkening was that the spicule spectrum was positive for all spectral values causing a too large Doppler width being calculated. The subtraction causes the computed width to be too small, but to a smaller extent. Figure 3.10 illustrates this by plotting the spicule spectrum and the spicule spectrum modified by subtraction of the average value for a spicule close to the limb.

- On-disk far from the limb: the average spectrum was computed as the average of all pixels to the right of the separation line.

## 3.4 Measuring the Spicule Properties

Every property except the Doppler width and Doppler velocity were measured in the intensity images from spectral position ±1.2 Åfrom line center.

### 3.4.1 Physical Length and Physical Width

The output from the detection, the spicules lines, provided the basis for the measurement of the length. 20 pixels were padded to the line at each end in the direction defined by a straight line connecting the end points. The intensity was retrieved from the data for every pixel in the extended line resulting in an intensity profile, an absorption profile for on-disk features and an emission profile for off-limb features. In order to calculate the full width at half maximum (FWHM) of the profile one needs to know the pixel values right outside the spicule. This is because the maximum value is relative to the intensity value in the absence of the spicule. This reference value is difficult to compute since spicules often occur close to each other, side by side, and therefore one cannot take an average value of some pixels in the close vicinity of the spicule. The most reliable method was to measure the maximum relative to the average level on the same pixel line in the opposite H$\alpha$ wing position.

The maximum value for the determination of the FWHM was defined as the highest value in the center part of the pixel line not closer than 10 pixels from the end points. This was to avoid the chance occurrence of a higher maximum in the padded part of the line which was unrelated to the spicule. The length of the detected line from the detection algorithm was a relative good measure of the length and it is unlikely that the maximum value of the spicule was outside this length.

Once the reference value was known, the FWHM of the intensity profile could be calculated. The profile was interpolated using the cubic spline algorithm to locate the exact position of the half maximum value (HMV) with sub-pixel accuracy. The line intensity profiles varied in appearance and no typical shape was apparent by visual inspection, hence it was considered to be fruitless to attempt fitting of curves. In addition, the profile was often erratic and could at more than two positions be equal to the HMV. Most spicules appear to the side of each other and extremely rarely on top or below (in the length direction), due to this observation, the outermost HMV positions found were used. If the HMV value at one of the end points could not be found, the corresponding end point from the detected line was used and the spicule was flagged to have ill defined length.

Before calculating the physical width, a line perpendicular to every pixel on the spicule line was created. The direction of a pixel was defined as the direction of the straight line connecting the two neighboring pixels. Because only two pixels were used, there were a limited number of angles, but enough to create a good estimate of the perpendicular line. The intensity was retrieved on the new lines resulting width intensity line profiles. The reference value was the same value used to compute the length of that spicule.

As with the length, there was diversity in the shape of the width profiles, not as much as for the length profiles, but no curves was fitted for the width profiles either. The suspected reason for the asymmetry in the profiles, are two or more spicules appearing so close together that they are not distinguishable and overlapping spicules due to the large line-of-sight effects. 10 pixels on either side of the spicule-line were used on the perpendicular line, and cubic spline was used to interpolate between the points to increase accuracy. On numerous occasions the HMV was reached more than two times. Because spicules most often occur at the side of each other, the FWHM-positions closest to the spicule line were used to increase the likelihood of measuring the width on only one spicule at a time. If one of the end points could not be located, that pixel on the spicule line was flagged to have ill defined width. If neither of the end points could be located, the width was defined to be 1 pixels wide.

Because the width intensity profiles were more regular than the length profiles, the symmetry of the profile was measured. The symmetry was defined as the pixel distance difference between the position of the maximum intensity value and the HMV positions on either side averaged over the length of the spicule.

The length and width measurements were also performed on the Doppler image, there with an outside value equal to zero.

### 3.4.2 Doppler Velocity and Doppler Width

The Doppler velocity and the Doppler width were calculated from the spicule spectrum obtained from pixels on the spicule line.

The Doppler velocity was defined as the expectation value and the width as the standard deviation as shown in equations 3.4 and 3.5 for the on-disk spicules. Off-limb the equations are identical with the exception that

$(I_{\rm avg} - I)$ is changed to $(I - I_{\rm avg})$.

$$v_{\rm Doppler} = \frac{c}{\lambda_0} \frac{\int_{\lambda_{\rm min}}^{\lambda_0} (\lambda - \lambda_0)(I_{\rm avg} - I) {\rm d}\lambda}{\int_{\lambda_{\rm min}}^{\lambda_0} (I_{\rm avg} - I) {\rm d}\lambda}, \tag{3.4}$$

$$W = \frac{c}{\lambda_0} \sqrt{\frac{\int_{\lambda_{\rm min}}^{\lambda_0} (\lambda - \lambda_c)^2 (I_{\rm avg} - I) {\rm d}\lambda}{\int_{\lambda_{\rm min}}^{\lambda_0} (I_{\rm avg} - I) {\rm d}\lambda}}, \tag{3.5}$$

where c is the speed of light, $\lambda_0$ is the line center wavelength, $\lambda_c = \lambda_0 + \lambda_0 v_{\rm Doppler}/c$, $I$ is the observed intensity, $I_{\rm avg}$ is the average intensity from the specific region and $\lambda_{\rm min}$ is the most blue-ward wavelength for blue-shifted spicules and the most red-ward wavelength for the red-shifted spicules. The integration range was only on the red side of the spectrum if the spicule was red-shifted, and on the blue side if the spicule was blue-shifted. The integration is only performed for wavelengths where $(I_{\rm avg} - I) > 0$ on-disk and for where $(I - I_{\rm avg}) > 0$ off-limb. If on no spectral positions in the wings the relations $(I_{\rm avg} - I) > 0$ or $(I - I_{\rm avg}) > 0$ were true, the width and velocity were put to zero.

Many authors fit a Gaussian curve to the spectra to estimate these properties, but because of the inaccuracies of obtaining the spicule spectra this are not necessary. The measurements are crude and the difference in the methods little. Inversion techniques like Becker's classical cloud model (Beckers, 1964) might for some cases yield better results, especially far off-limb where one can consider the background to be zero. For more information on cloud modeling, readers are referred to Tziotziou (2007) with references therein.

### 3.4.3 Limb Distance, Angle with the Limb and Spicule Curvature

After the end points of the spicule were determined, it was straightforward to calculate the shortest and longest distances to the limb. Is was simply the length of a straight line from the limb to the end points, one for each, perpendicular to the limb. The angle of the limb was determined by fitting a straight line to the positions of the limb at the top and at the bottom of the image. The limb was defined to be where the disk intensity had dropped to half its average disk value at spectral position $-1.2$ Å relative to the off-limb value.

The direction of a spicule was defined as the direction of a straight line connecting the end points, from the footpoint to the top-point. The footpoint

and top-point were defined after the apparent direction from the motion of the spicules, which for all spicules were to the left in the images. This meant that for all spicules, the footpoint was the rightmost point.

To measure the curvature, the average direction of the first $1/x$ and last $1/x$ pixels of the spicule were calculated, where $x$ was $\{3, 4, 5, 6\}$. The averaged directions on either side were subtracted yielding a crude measure of the curvature of a spicule.

### 3.4.4 Lifetime

The lifetimes of the spicules were measured manually for 160 spicules, 40 from each group in the Doppler images. It was measured in the periods were the seeing was good for a long time, primarily in the first dataset around time step no. 110, 260 and 415. The lifetimes were measured on spicules that were isolated from other spicules, otherwise it was difficult to track the spicules for their entire lifetime. Almost all of the on-disk spicules that had their lifetimes measured were located outside the active region in the corner. The reason for the lifetimes being measured manually was because the detection algorithm often did not detect the spicules in all frames they were present in, yielding a too short estimate of the lifetimes.

# Chapter 4

# Results

## 4.1 Spicule Motion

To illustrate the motion displayed by spicules seen in the observations from this thesis, four spicules were chosen and their time evolution and spectral signatures are displayed below. The locations are in which they occurred is marked with numbers in Fig. 4.1. In region 1 an on-disk red-shifted spicule was selected, in region 2 an on-disk blue-shifted spicule was selected, in region 3 an off-limb blue-shifted spicule was selected and in region 4 an off-limb red-shifted spicule was selected.

### 4.1.1 An On-disk Red-shifted Spicule in Region 1

The time evolution of the spicule from region 1 is shown in Fig. 4.2. The top three rows are cutouts from the intensity images, while the 3 bottom-most rows are the same time steps, but instead the positive values from the Doppler images are showed. The cutouts are fixed spatially in time so the transverse displacement of the spicule is more easily seen. In the first time step, the spicule is not visible in the intensity image, but the Doppler image shows a small signal. Its full length is reached after 12 seconds and the spicule appears to move upward while being displaced toward the right.

At $t = 1341.3$ s, labeled $t = 0$ in Fig. 4.3, the spectrum from below the cross is plotted in Fig. 4.3. The top panel is a larger cutout from the intensity image. The middle panel shows the spectral evolution ($\lambda t$-slice) from the location in the spicule marked with the white cross in the top panel. In the middle panel a sudden widening of the spectral line is seen, only on the

red-wing around $t = 0$. No widening of the blue-wing is apparent directly afterward. In the bottom panel, the average spectrum is the top-most solid line and the spectrum from below the white cross is the dotted line. The solid line at the bottom is the computed spicule spectrum. It is double-peaked and has a clear maximum point at about 45 km/s. The cause of the double peaked spectrum is discussed more in detail in section 4.1.2 as the cause is more easily seen there. The full line scan around the spicule is shown in Fig. 4.4.

### 4.1.2 An On-disk Blue-shifted Spicule in Region 2

The time evolution of the spicule from region 2 is shown in Fig. 4.5, the spectral evolution is shown in Fig. 4.6 and a full line scan for a small region around the spicule is shown in Fig. 4.7. There are many spicule visible in the images in Fig. 4.5 and the time series illustrate the difficulties of measuring the lifetime of a spicule. There appears to be a small group of spicules that shoot toward the upper left corner, while being displaced toward the top right. The spicules are sometimes indistinguishable which also illustrates the difficulties of measuring the physical length and width of the spicules.

At $t = 686.6$ s, labeled $t = 0$ in Fig. 4.6, the spectrum from below the white cross is plotted in Fig. 4.6. The middle panel shows a $\lambda t$-plot and the bottom panel shows the spicule spectrum. The middle panel in Fig. 4.6 illustrates why these events are called "Rapid Blue-shifted Excursions" (RBEs). A sudden widening of the spectral line is seen, but only in the blue-wing. The spicule spectrum has two peaks, one in each wing of the spectrum. The cause of this double peaked appearance is visible in Fig. 4.7, which shows a line-scan around the spicules. One of the spicules is clearly seen in the upper left panel as a dark streak, but at the other side of the spectrum, at $\Delta\lambda = 0.6$ Å to 0.9 Å one sees that the white cross is positioned in the middle of a darker patch. This dark patch is a region where the fibrils are visible to further out in the wing than right outside the dark patch. The average spectrum is the average spectrum of pixels from a much larger area than the size of the patch. This means that small variations in the brightness in the images, happening because the fibrils are visible out to different wavelengths in the wing, is averaged out in the average spectrum. However, the integration range for the standard deviation and expectation value are only on the wing the absorption from the spicule occurs on, so the absorption peak on the other side of the spectrum is not in the calculations of the Doppler velocities and Doppler widths.

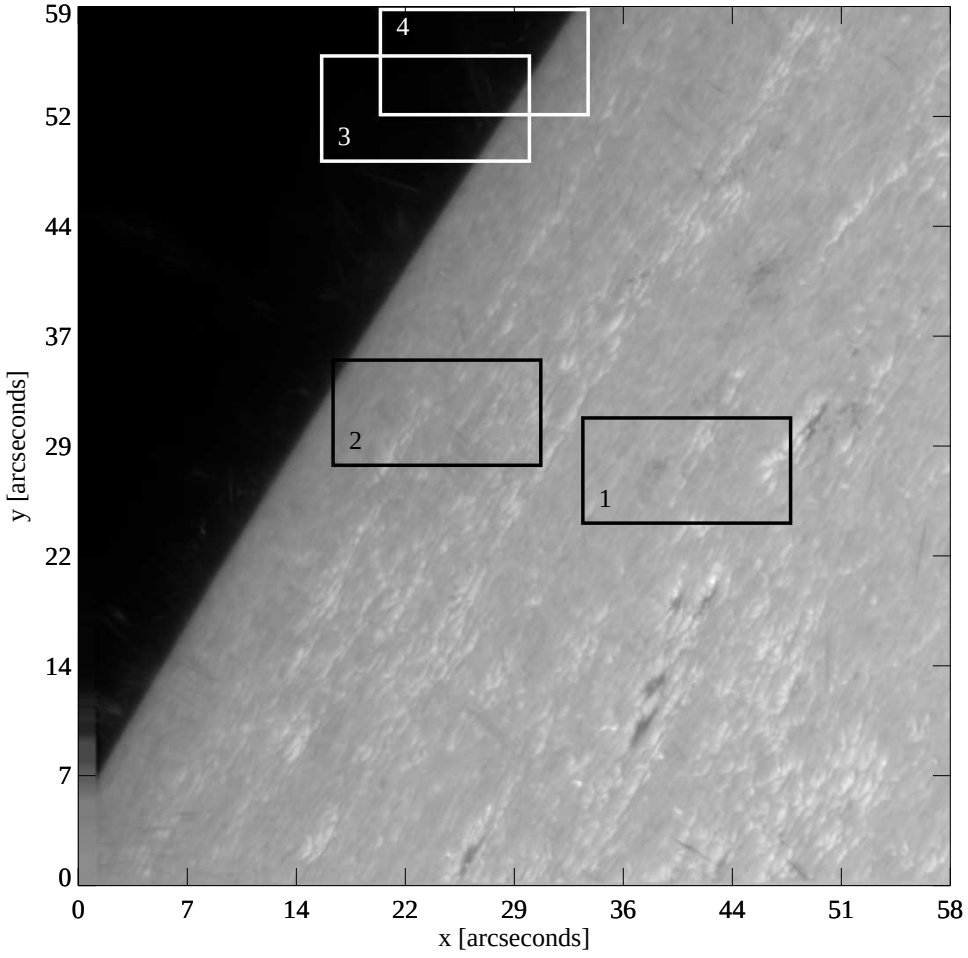


**Figure 4.1:** An image of the Sun showing the locations of the four example spicules. In region 1 a red-shifted spicule was selected, in region 2 a blue-shifted spicule was selected, in region 3 a blue-shifted spicule was selected and in region 4 a red-shifted spicule was selected. The size of the rectangles mark the cutouts displayed in Figs. 4.3, 4.6, 4.9 and 4.12.

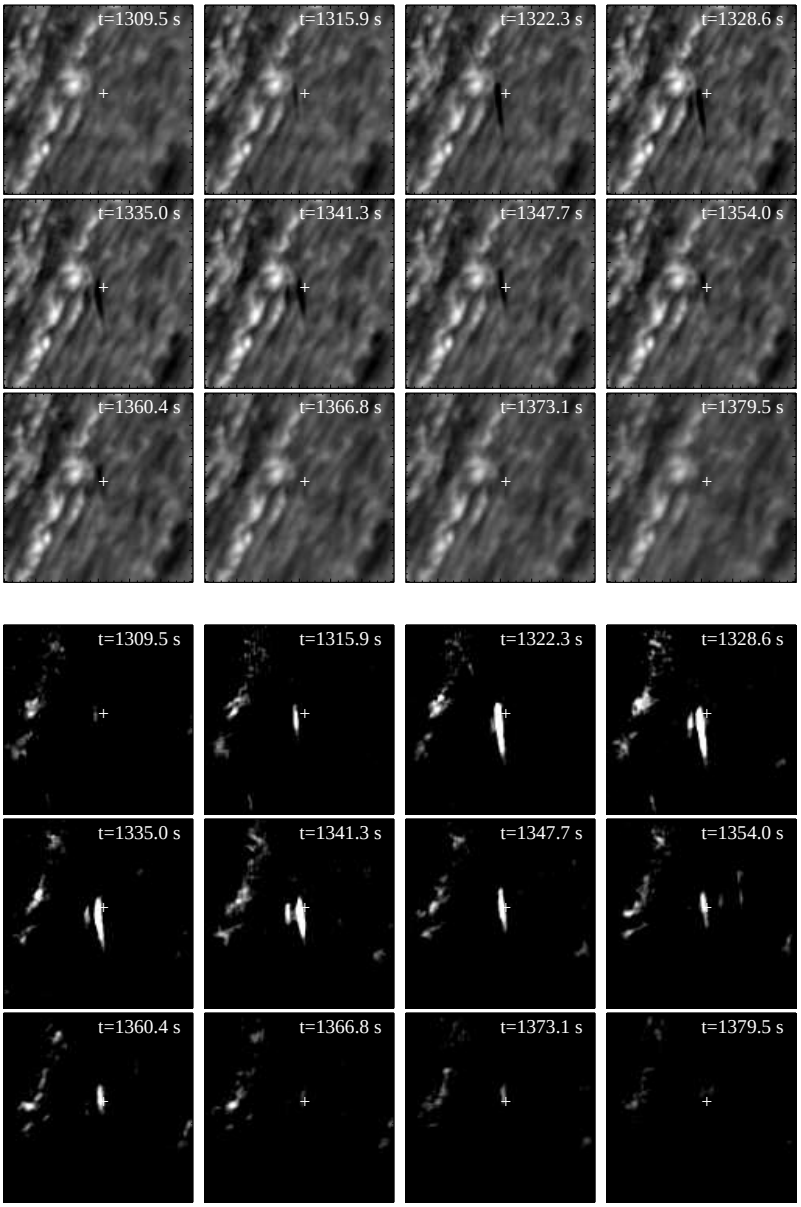


**Figure 4.2:** Time series showing the evolution of one red-shifted spicule in region 1, shown in row-major order. The top three rows are cutouts from the intensity images, while the 3 bottom-most rows are the same time steps, but instead the positive values of the Doppler images are displayed. The cutouts are fixed spatially in time so the transverse displacement of the spicule is more easily seen. The cutouts are $7'' \times 7''$ in size.

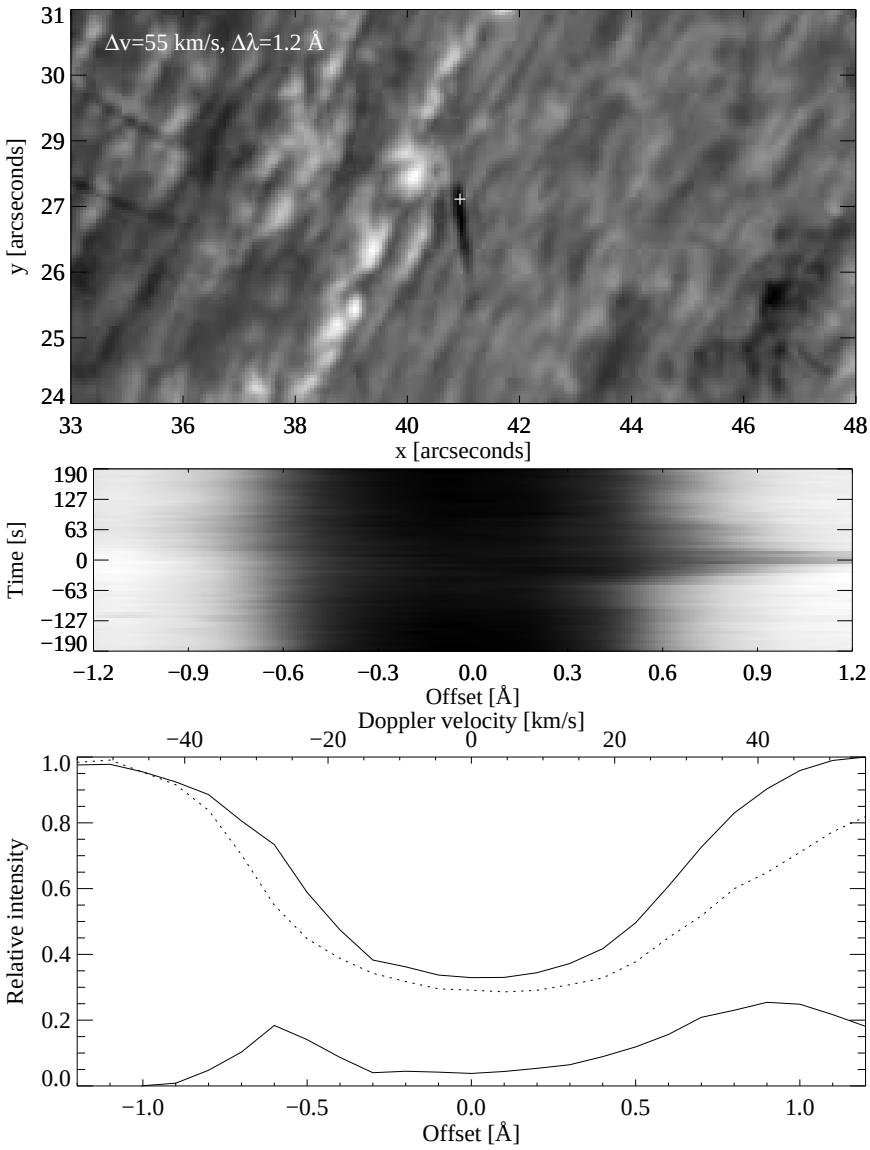


**Figure 4.3:** Details from one red-shifted spicule in region 1. Middle panel: spectral evolution ($\lambda t$-slice) from the location in the spicule marked with the white cross in the top panel. Bottom panel: spectral line profiles, the solid line is the average spectrum from the region where this spicule occurred, the dotted line is the spectrum observed at the cross at $t = 0$, and the bottom solid line is the difference between the two profiles, i.e., the derived spicule spectrum.

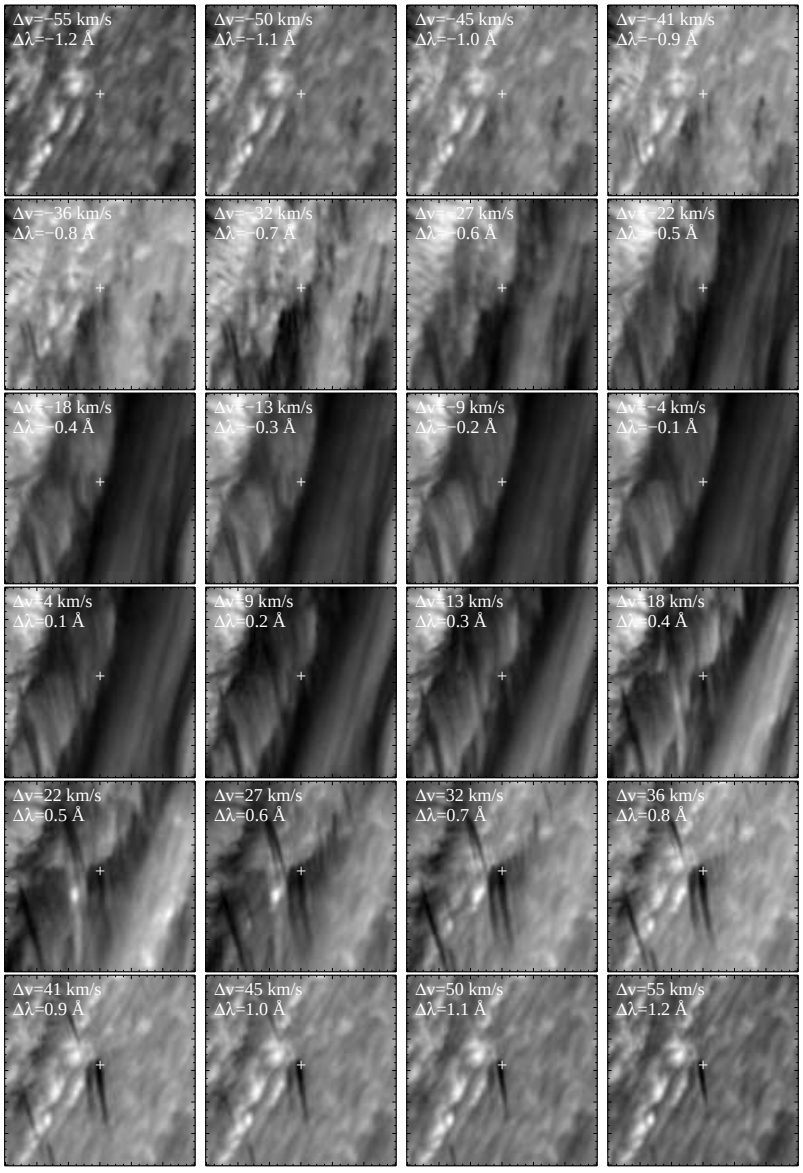


**Figure 4.4:** A full line scan on a 7″×7″ region around one red-shifted spicule in region 1. The cutouts remain fixed spatially in the scan which is displayed in row-major order.

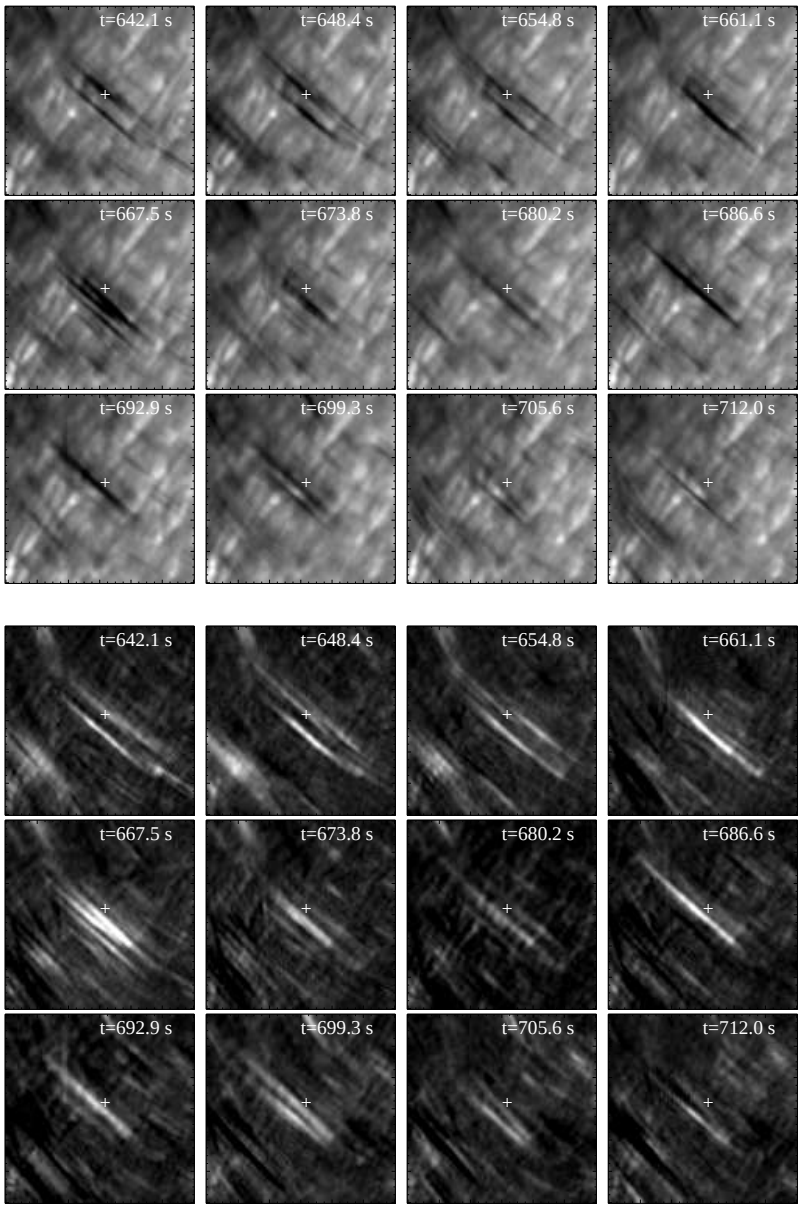


**Figure 4.5:** Time series showing the evolution of one blue-shifted spicule in region 2. The top three rows are cutouts from the intensity images, while the 3 bottom-most rows are the same time steps, but instead the negative values from the Doppler images are showed. The cutouts are fixed spatially in time so the transverse displacement of the spicule is more easily seen. The cutouts are $7'' \times 7''$ in size.

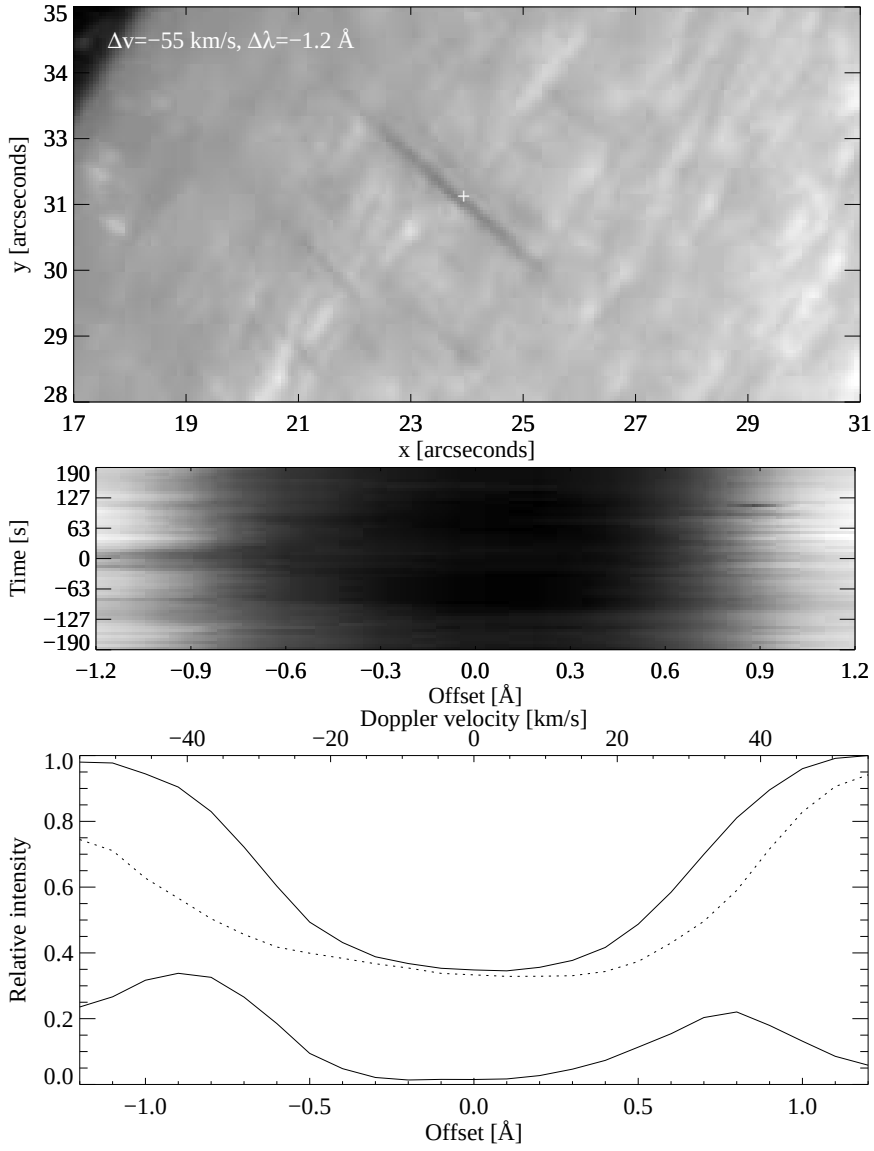


**Figure 4.6:** Details from one blue-shifted spicule in region 1. Middle panel: spectral evolution ($\lambda t$-slice) from the location in the spicule marked with the white cross in the top panel. Bottom panel: spectral line profiles, the solid line is the average spectrum from the region where this spicule occurred, the dotted line is the spectrum from the cross at $t = 0$, and the bottom solid line is the difference between the two profiles, i.e., the derived spicule spectrum.

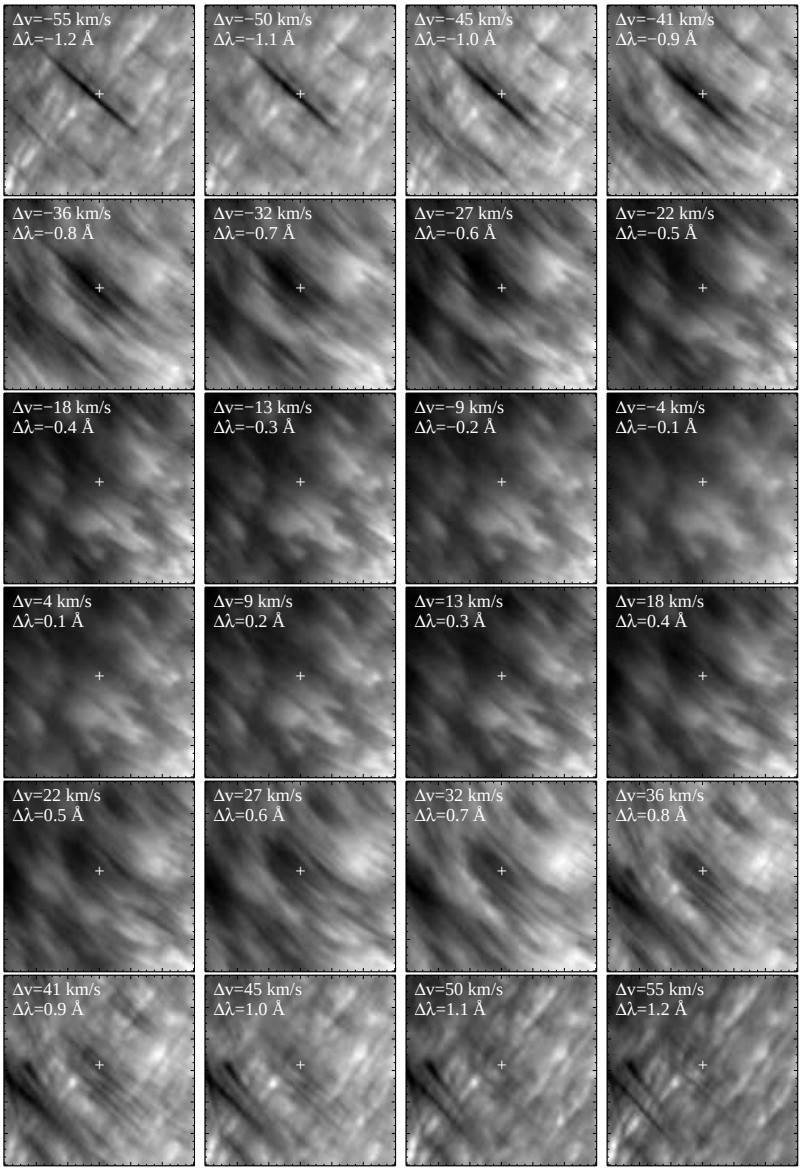


**Figure 4.7:** A full line scan on a 7″×7″ region around one blue-shifted spicule in region 2. The cutouts remain fixed spatially in the scan which is displayed in row-major order.

### 4.1.3 A Blue-shifted Spicule Off-limb in Region 3

The time evolution of a blue-shifted spicule from region 3 is shown in Fig. 4.8. The top three rows are cutouts from the intensity images, while the 3 bottom-most rows are the same time steps, but instead the positive values of the Doppler images are displayed. The cutouts are fixed spatially in time so the transverse displacement of the spicule is more easily seen. The spicule is not visible in the first 4 images. It reaches its full length in the second frame it is visible in, and is only visible for 5 frames.

At $t = 845.3$ s, labeled $t = 0$ in Fig. 4.9, the spectrum from below the cross is plotted in Fig. 4.9. In the middle panel in Fig. 4.9, a clear widening of the spectral line in the blue wing is seen at around $t = 0$. About 40 seconds later there is a corresponding widening on the red side, but due to the large line-of-sight effects at the limb it is not possible to determine its connection, if any, to the blue-shifted spicule. In the middle panel the lowest solid line is the spicule spectrum from the white cross at $t = 0$. This spectrum is not fully resolved resulting in incorrect Doppler velocity and Doppler width being computed.

### 4.1.4 A Red-shifted Spicule Off-limb in Region 4

The time evolution of the red-shifted spicule from region 4 is shown in Fig. 4.11, the spectral evolution is shown in Fig. 4.12 and a full line scan shown for a small region around the spicule in Fig. 4.13. In Fig. 4.11 the spicule is barely visible at $t = 692.9$ s and it is gone at $t = 743.8$ s.

At $t = 724.7$ s, labeled $t = 0$ in Fig. 4.12, the spectrum from below the cross is plotted in Fig. 4.12. In the middle panel of Fig. 4.12, a clear widening of the spectral line in the red wing is seen at $t = 0$. In the middle panel the lowest solid line is the spicule spectrum from the white cross at $t = 0$. The spicule spectrum is not fully resolved, resulting in incorrect Doppler velocity and Doppler width being computed. This spicule potentially has a Doppler velocity of $\sim 70$ km/s.

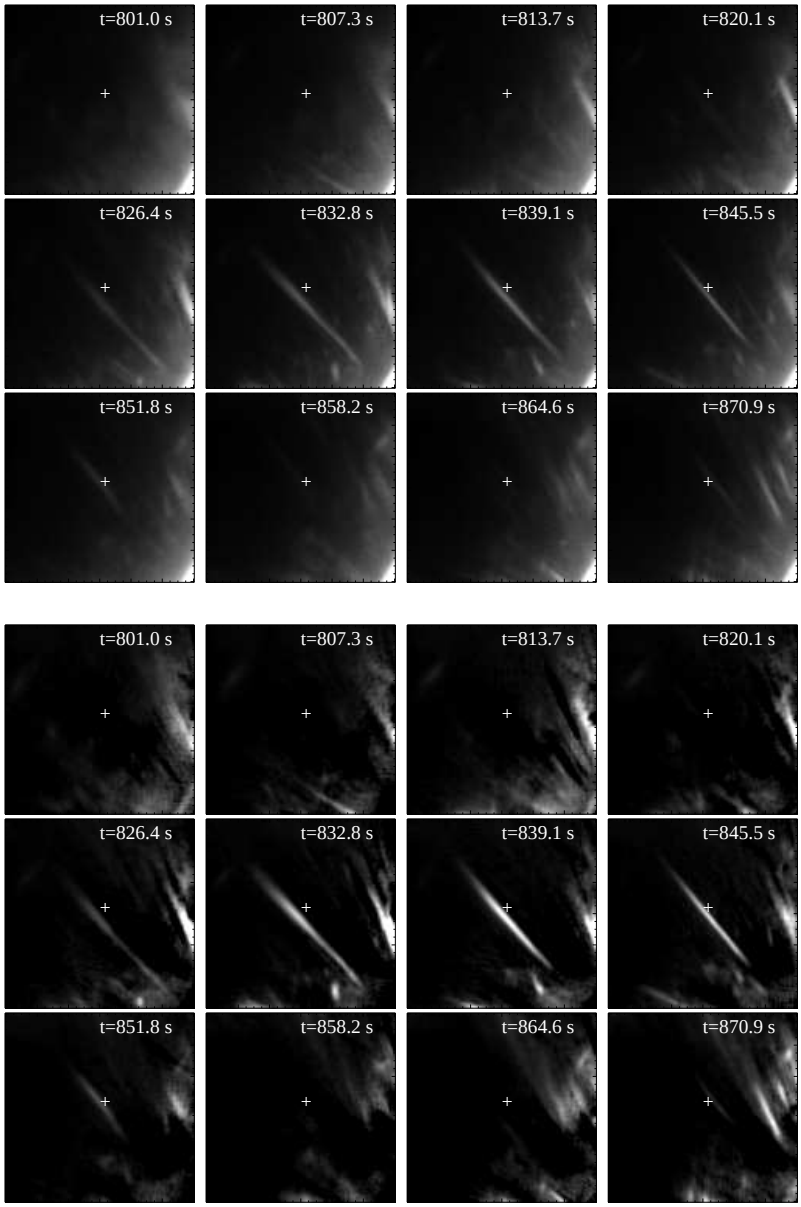


**Figure 4.8:** Time series showing the evolution of one blue-shifted spicule in region 3, shown in row-major order. The top three rows are cutouts from the intensity images, while the 3 bottom-most rows are the same time steps, but instead the positive values of the Doppler images are displayed. The cutouts are fixed spatially in time so the transverse displacement of the spicule is more easily seen. The cutouts are $7'' \times 7''$ in size.

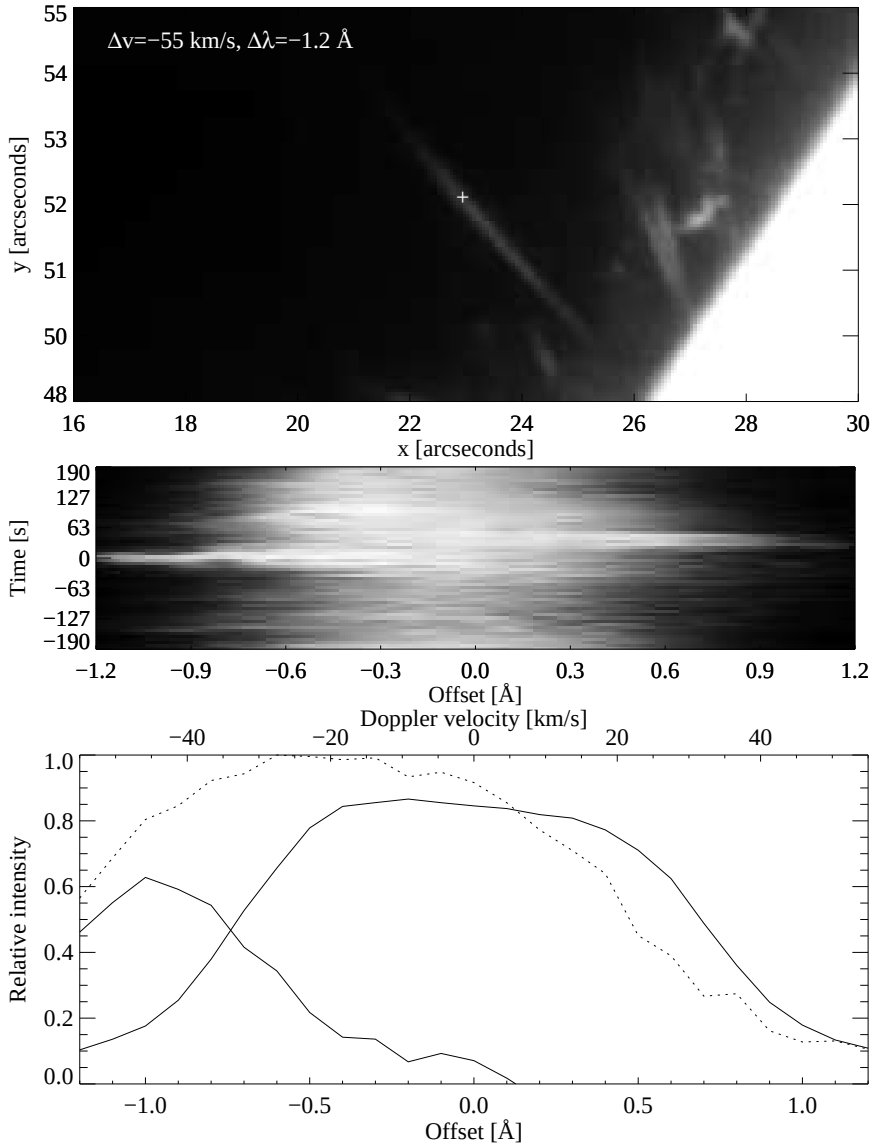


**Figure 4.9:** Details from one blue-shifted spicule in region 1. Middle panel: spectral evolution ($\lambda t$-slice) from the location in the spicule marked with the white cross in the top panel. Bottom panel: spectral line profiles, the solid line is the average spectrum from the region where this spicule occurred, the dotted line is the spectrum observed at the cross at $t = 0$, and the bottom solid line is the difference between the two profiles, i.e., the derived spicule spectrum.

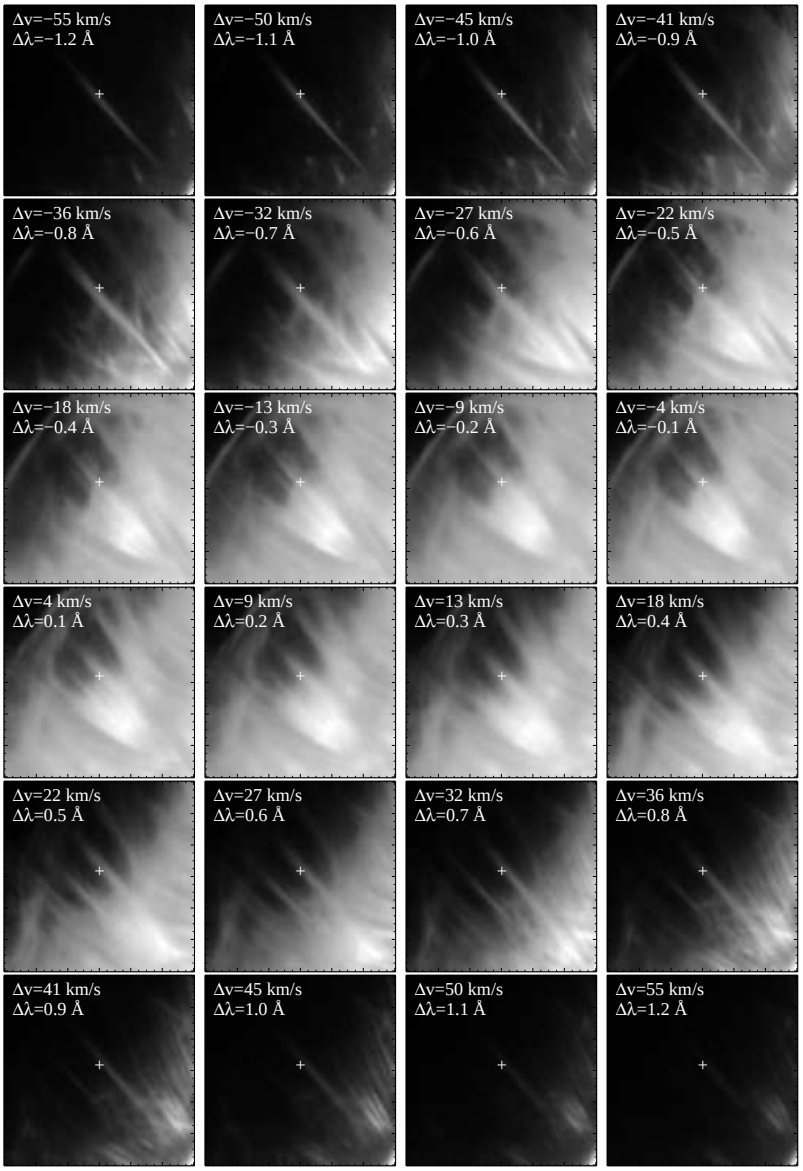


**Figure 4.10:** A full line scan on a $7'' \times 7''$ region around one blue-shifted spicule in region 3. The cutouts remain fixed spatially in the scan which is shown in row-major order.

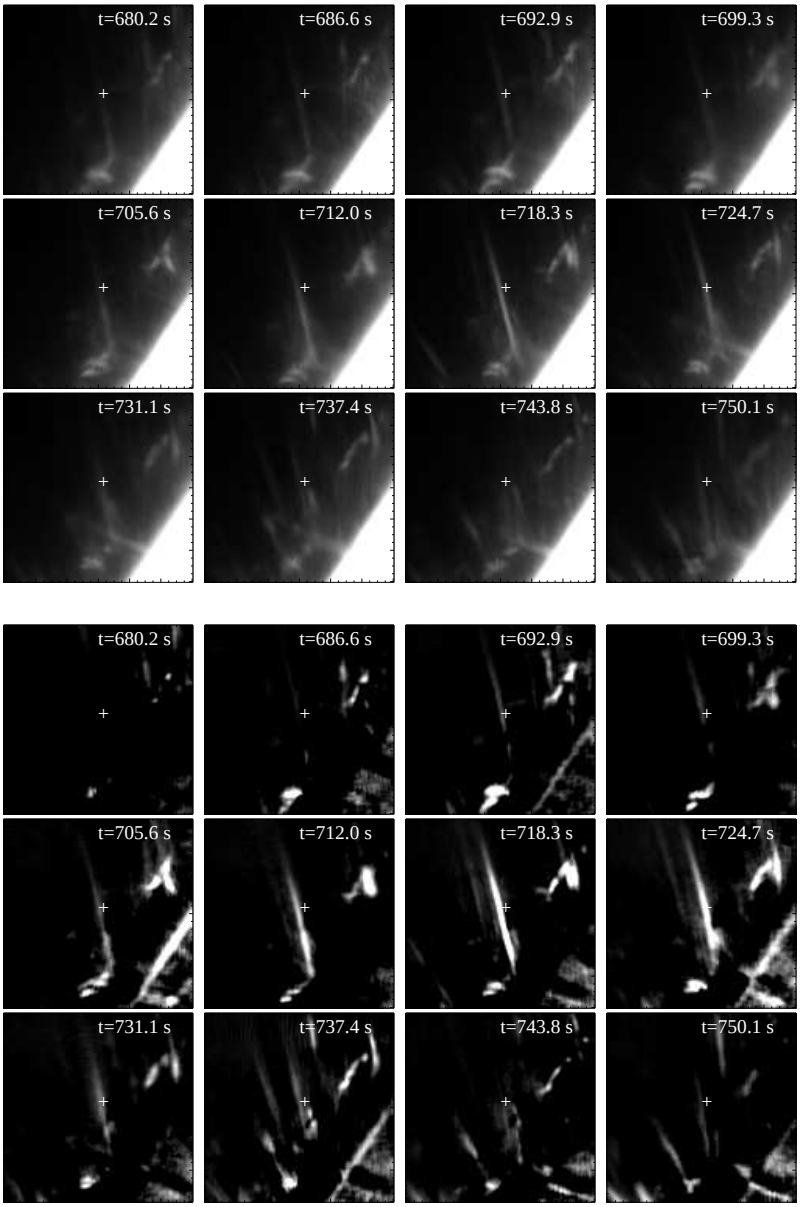


**Figure 4.11:** Time series showing the evolution of one red-shifted spicule in region 4, shown in row-major order. The top three rows are cutouts from the intensity images, while the 3 bottom-most rows are the same time steps, but instead the negative values from the Doppler images are displayed. The cutouts are fixed spatially in time so the transverse displacement of the spicule is more easily seen. The cutouts are $7'' \times 7''$ in size.

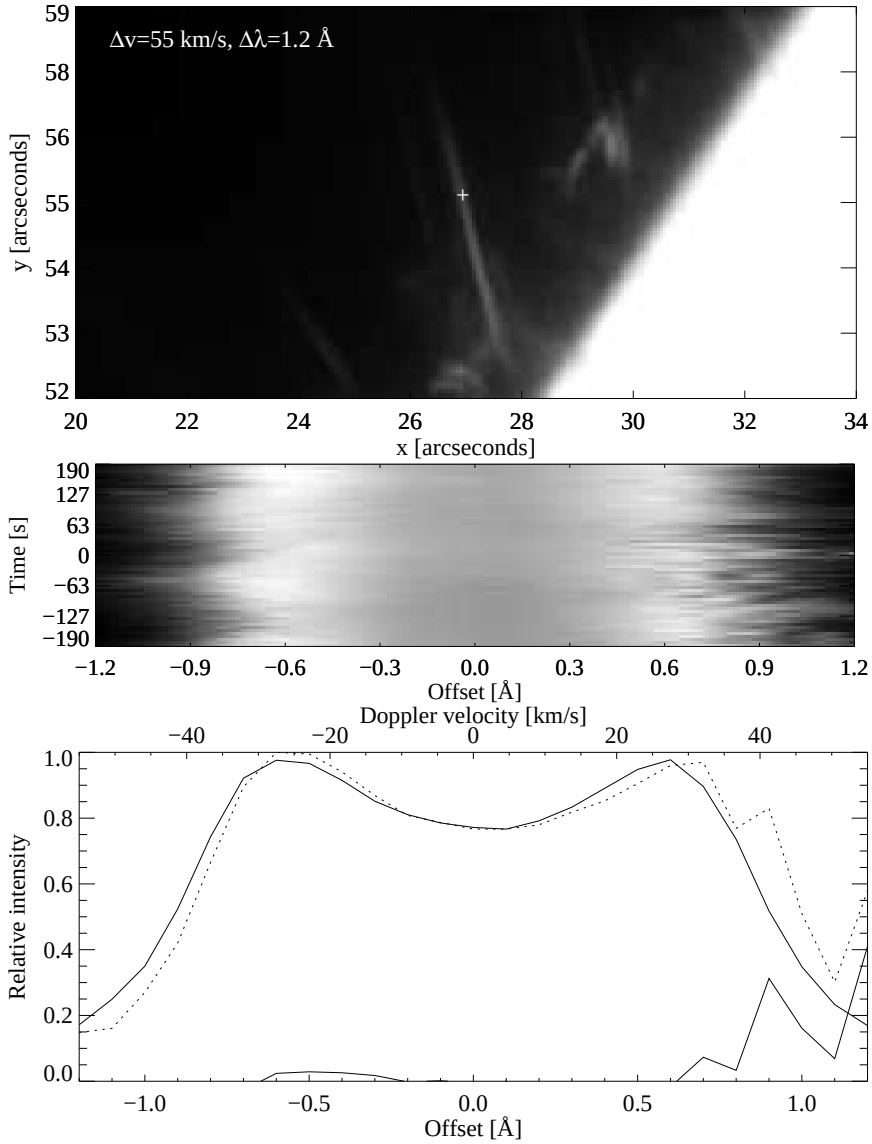


**Figure 4.12:** Details from one red-shifted spicule in region 4. Middle panel: spectral evolution ($\lambda t$-slice) from the location in the spicule marked with the white cross in the top panel. Bottom panel: spectral line profiles, the solid line is the average spectrum from the region where this spicule occurred, the dotted line is the spectrum observed at the cross at $t = 0$, and the bottom solid line is the difference between the two profiles, i.e., the derived spicule spectrum.

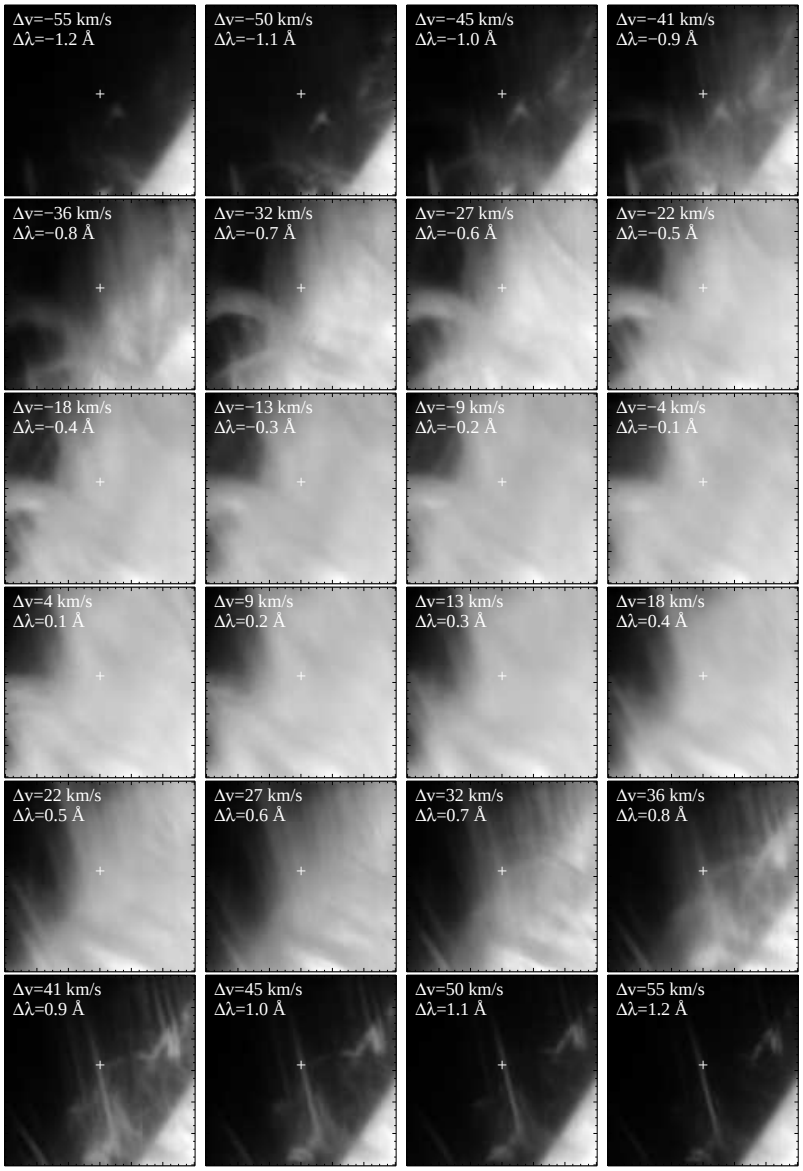


**Figure 4.13:** A full line scan on a $7'' \times 7''$ region around the red-shifted spicule from region 4. The cutouts remain fixed spatially in the scan which is shown in row-major order.

## 4.2 Measured Physical Properties

Some spicules were detected at roughly the same spatial position for several consecutive time steps. To ensure spicules are not counted multiple times in the statistics, only the first detected occurrence of a spicule was used. This first occurrence can be from any part of the lifetime of a spicule because spicules can form on a time scale shorter than the cadence of the observations. If for instance 2 time steps had bad seeing, a spicule living for three frames could form in the first bad frame, and the last frame it existed was when it was detected. Hence a histogram of a property is an implicit time average of that property. From all measured properties, only the length was found by visual inspection to exhibit a dramatic time evolution; large portions from the top of the spicule could disappear between two time steps.

The normalization constant used in a histogram is the total number of spicules combined from each group. Each histogram is individually divided by this constant. By group is meant for instance: the on-disk blue-shifted spicules. When the length is described as well defined it is meant that both end points could be identified using the FWHM procedure. The width at one pixel position on the spicule line is well defined if both end points on the width intensity profile could be identified using the FWHM procedure. A spicule has a well defined (average) width if more the 80 % of the pixels on the spicule line have well defined widths. The spicule line is the spicule thinned to a one pixel thick line.

Measurements of the projected lengths and widths were done in both the intensity images and in the Doppler images. Due to the elimination of the background in the Doppler images, the FWHM procedure succeeded more often compared to measurements in the intensity images. The complicated background found in the intensity images causes the procedure to fail often, resulting in sometimes few spicules in the statistics. The measurements from the intensity images are taken to be the proper results, which are augmented by the measurements from the Doppler images.

### 4.2.1 The detected number of spicules

The number of detected spicules in the different groups are shown in Fig. 4.14 for the intensity images and in Fig. 4.15 for the Doppler images. The location of the detected spicules combined for all time steps are illustrated separately for the red-shifted and the blue-shifted spicules in Fig. 4.16. The images also show how often the detected spicules were occurring at one location.

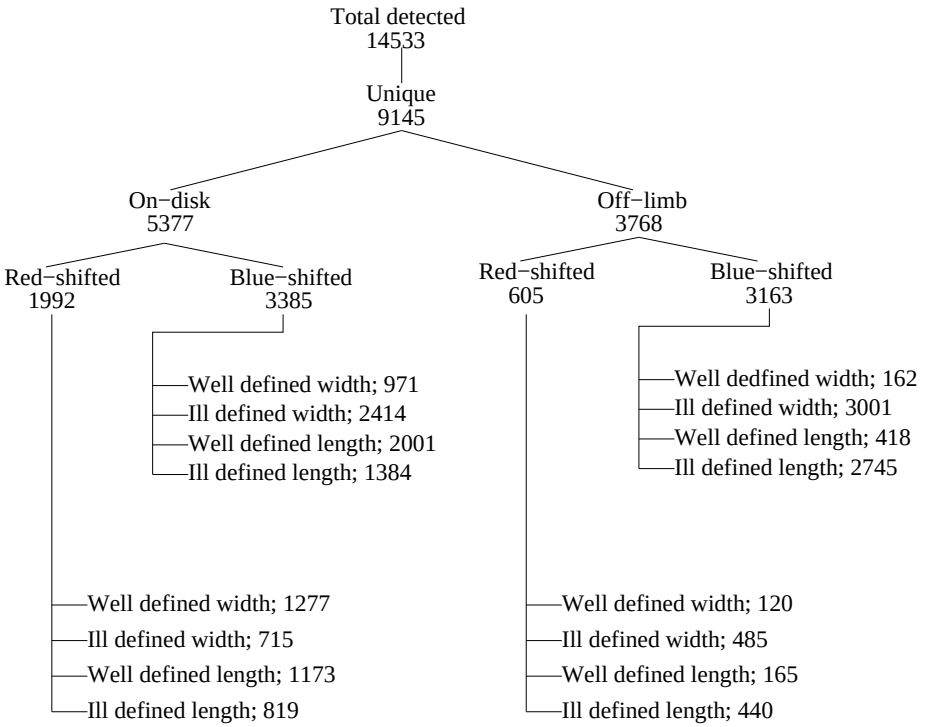


**Figure 4.14:** The number of detected spicules from the intensity images split into the different groups.

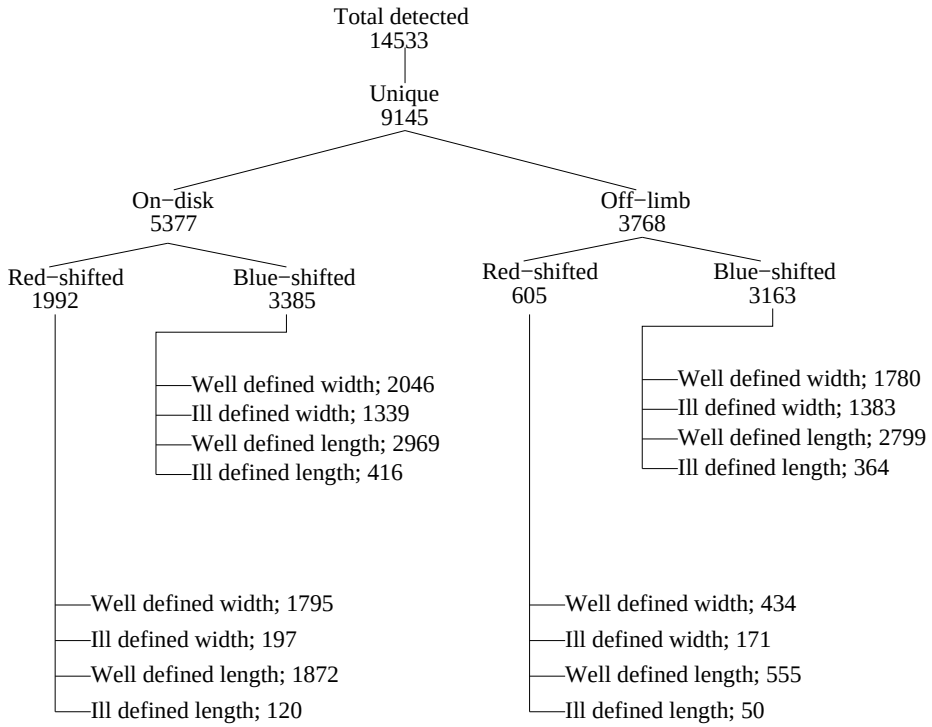


**Figure 4.15:** The number of detected spicules from the Doppler images split into the different groups.

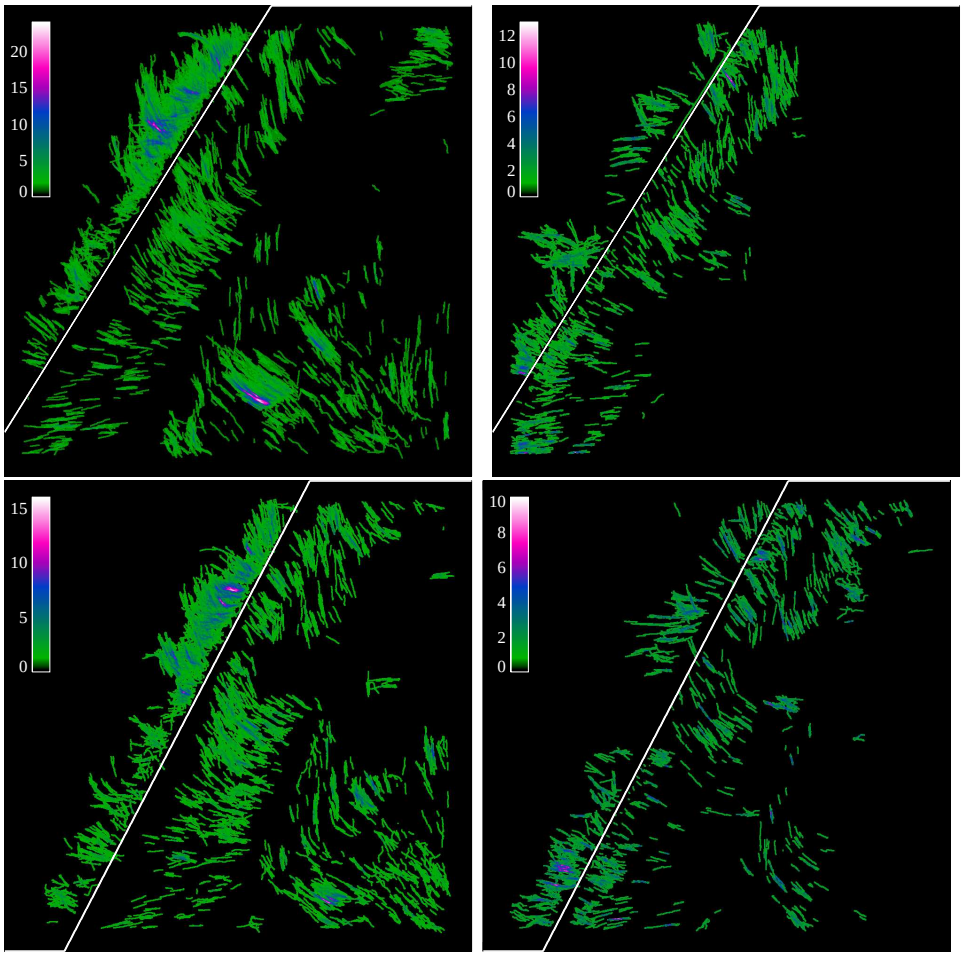


**Figure 4.16:** Color-coded image showing the number of times spicules were detected at one location. Top left: the blue-shifted spicules from the first dataset. Top right: the red-shifted spicules from the first dataset. Bottom left: the blue-shifted spicules from the second dataset. Bottom right: the red-shifted spicules from the second dataset. All images: the image size is 59″×59″and the color bar indicates the number of times spicules occurred at each pixel. The white inclined line marks the approximate position of the limb. The spicule lines are widened to three pixels to more clearly show on paper.

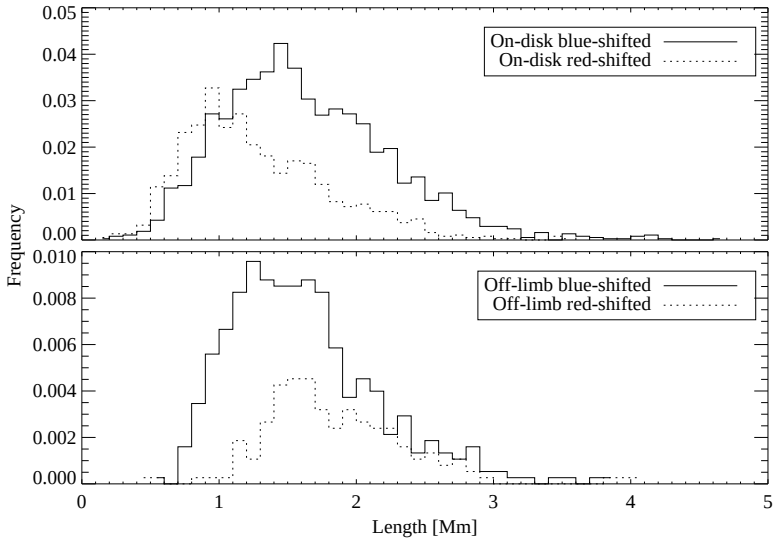


**Figure 4.17:** Length of the spicules measured in the intensity image. Only spicules were both end points were well defined are included in the histograms.

### 4.2.2 Projected physical length

The length of the spicules measured on the intensity images are plotted in Fig. 4.17. Only spicules with well defined lengths are included in the histograms. The expectation value ($\mu$), median value ($M$), standard deviation ($\sigma$) and number of spicules in the histograms for the different groups are: on-disk blue-shifted: 1.6 Mm, 1.6 Mm, 0.6 Mm and 2001. On-disk red-shifted: 1.3 Mm, 1.2 Mm, 0.5 Mm and 1173. Off-limb blue shifted: 1.6 Mm, 1.5 Mm, 0.5 Mm and 418. Off-limb red-shifted: 1.8 Mm, 1.8 Mm, 0.5 Mm and 165.

In the Doppler images, the limb was not visible which resulted in more spicules with well defined lengths. The histograms of the length measurements on the Doppler image are plotted in Fig. 4.18. The expectation value, median value, standard deviation and number of spicules in the histograms for the different groups are: on-disk blue-shifted: 1.9 Mm, 1.8 Mm, 0.5 Mm and 2969. On-disk red-shifted: 1.5 Mm, 1.4 Mm, 0.5 Mm and 1872. Off-limb blue shifted: 1.5 Mm, 1.5 Mm, 0.6 Mm and 2799. Off-limb red-shifted: 1.7 Mm, 1.7 Mm, 0.5 Mm and 555.

The difference in length when measured in the Doppler image and the intensity image was computed when the length was well defined in both images. The differences are plotted in Fig. 4.19 and are computed as intensity_length − Doppler_length. The expectation value, median value, standard deviation

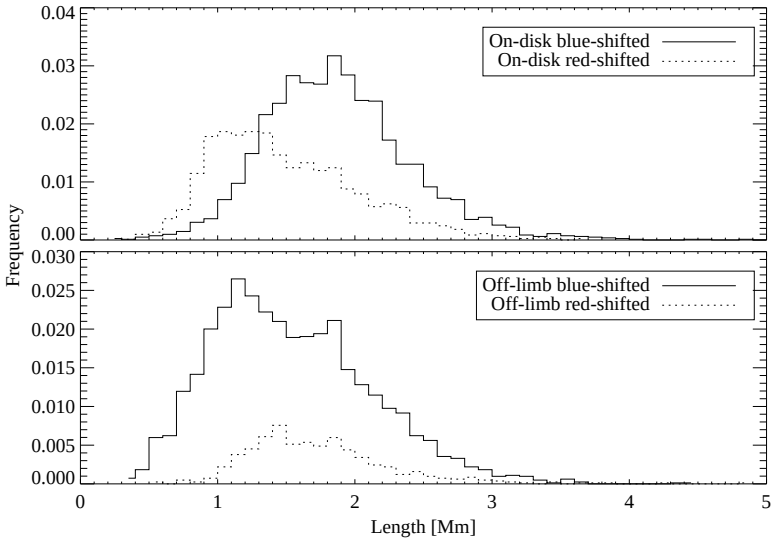


**Figure 4.18:** Lengths of the spicules measured in the Doppler images. Only spicules with well defined lengths are included in the histograms.

and number of spicules in the histograms for the different groups are: on-disk blue-shifted: −0.2 Mm, −0.2 Mm, 0.6 Mm and 1843. On-disk red-shifted: −0.2 Mm, −0.1 Mm, 0.6 Mm and 1128. Off-limb blue shifted: 0.4 Mm, 0.3 Mm, 0.3 Mm and 416. Off-limb red-shifted: 0.2 Mm, 0.2 Mm, 0.3 Mm and 163.

### 4.2.3 Projected physical width

The average value of the physical widths for each spicule is plotted in Fig. 4.20. Only spicules where more than 80 % of the pixels in the spicule line had well defined widths are included. The average value is calculated including only the well defined width pixels. The expectation value, median value, standard deviation and number of spicules in the histograms for the different groups are: on-disk blue-shifted: 0.3 Mm, 0.3 Mm, 0.1 Mm and 971. On-disk red-shifted: 0.2 Mm, 0.2 Mm, 0.1 Mm and 1277. Off-limb blue shifted: 0.4 Mm, 0.4 Mm, 0.1 Mm and 162. Off-limb red-shifted: 0.4 Mm, 0.4 Mm, 0.1 Mm and 120.

These measurements were also performed on the Doppler image plotted in Fig. 4.21. The expectation value, median value, standard deviation and number of spicules in the histograms for the different groups are: on-disk blue-shifted: 0.3 Mm, 0.3 Mm, 0.1 Mm and 2046. On-disk red-shifted:

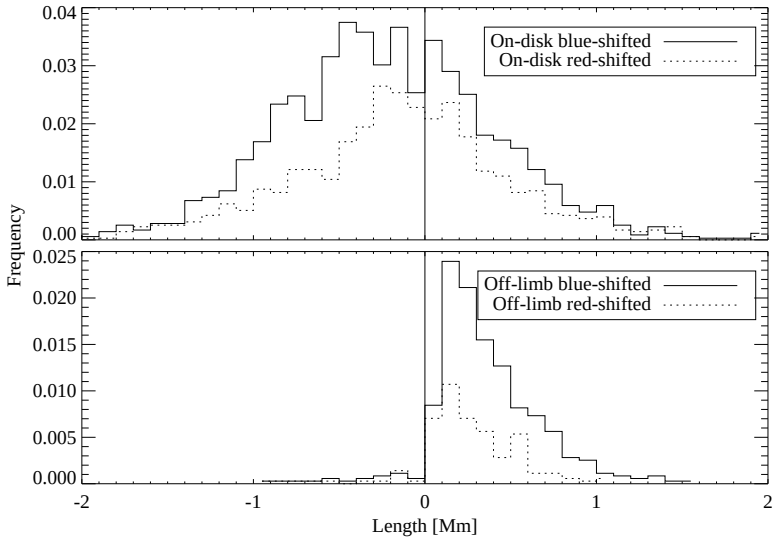


**Figure 4.19:** Differences of the lengths when measured in the intensity images and the Doppler images. The difference is computed as intensity_length − Doppler_length.

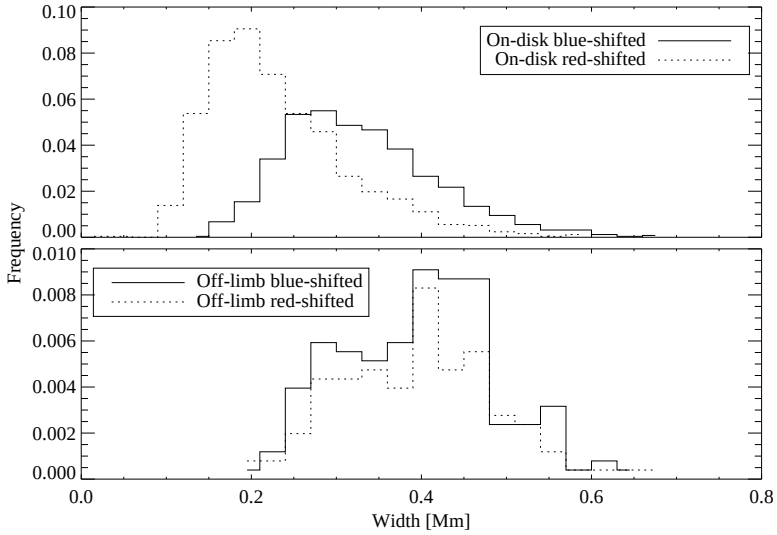


**Figure 4.20:** Average spicule width measured in the intensity image. Only spicules where more than 80 % of the pixels had well defined widths are included.

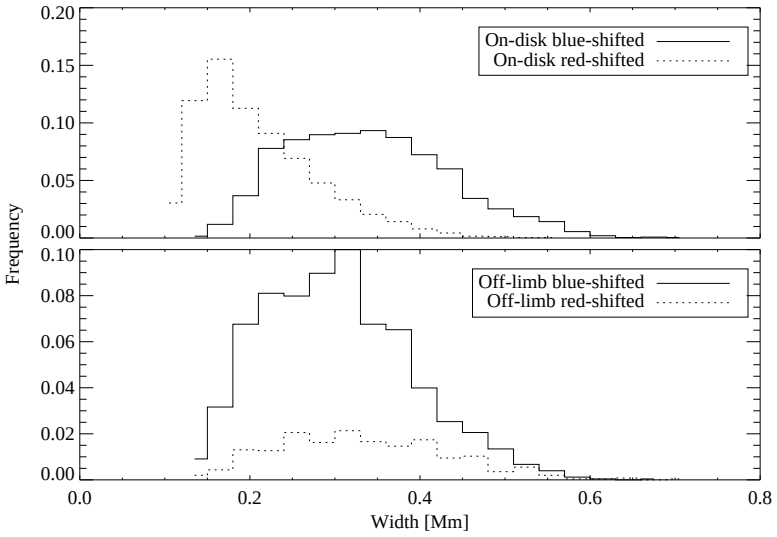


**Figure 4.21:** Average spicule width measured in the Doppler image. Only spicules where more than 80 % of the pixels well defined widths are included.

0.2 Mm, 0.2 Mm, 0.1 Mm and 1795. Off-limb blue shifted: 0.3 Mm, 0.3 Mm, 0.1 Mm and 1780. Off-limb red-shifted: 0.3 Mm, 0.3 Mm, 0.1 Mm and 434.

The variation of the width, for the intensity images, along the length for each spicule is shown in Fig. 4.22. The width at one pixel position is the average width of all the widths occurring on that pixel position.

The variation of the width along the length of the spicules is plotted in Figs. 4.23, 4.24 and 4.25. Only spicules with well defined average widths are included. The difference between the average values at the footpoint, midpoint and top-point was computed using the 5 pixels closest to the respective parts. A minimum length of 15 pixels was imposed to prevent overlap of pixels when the spicules are short. Figure 4.23 shows the difference in width between the top-point and the footpoint, calculated as: top-point−footpoint. Fig. 4.24 shows the difference in width between the midpoint and the footpoint, calculated as: midpoint−footpoint. Fig. 4.25 shows the difference in width between the top-point and the midpoint, calculated as: top-point−midpoint. The expectation values, standard deviations and numbers of spicules for the figures are tabulated in table 4.1.

These measurements were also performed on the Doppler image, shown in Figs. 4.26, 4.27 and 4.28. These figures have the same differences as Figs. 4.23, 4.24 and 4.25, respectively. The statistical properties are tabulated in table 4.2.

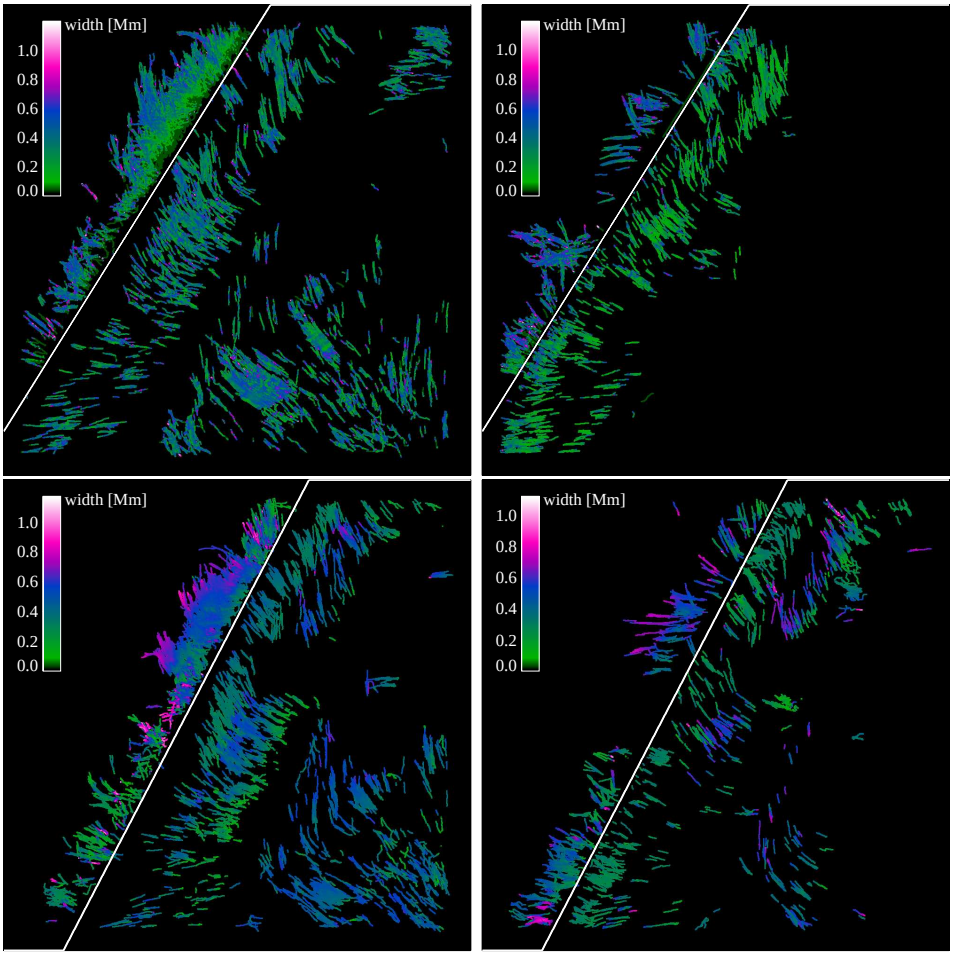


**Figure 4.22:** The variation of the physical width along each spicule. All spicules from one group are superimposed on one image, and the width occurring at one pixel position is computed as the average of all widths occurring on that pixel position. Top left: the blue-shifted spicules from the first dataset. Top left: the blue-shifted spicules from the first dataset. Top right: the red-shifted spicules from the first dataset. Bottom left: the blue-shifted spicules from the second dataset. Bottom right: the red-shifted spicules from the second dataset. All images: the image size is $59'' \times 59''$, the color bar indicates the width in mega-meters and the white inclined line marks the approximate position of the limb. The spicule lines are widened to 3 pixels in order to be more visible on paper.

**Table 4.1:** Table showing the variation of the physical widths from the intensity image in the first and second half of the spicules.

| **On-disk blue-shifted** | $\mu$ [Mm] | $M$ [Mm] | $\sigma$ [Mm] | Count |
|---|---|---|---|---|
| Top-point − Footpoint | 0.02 | 0.02 | 0.2 | 971 |
| Midpoint − Footpoint | −0.01 | 0.00 | 0.1 | ” |
| Top-point − Midpoint | 0.03 | 0.03 | 0.1 | ” |
| **On-disk red-shifted** | | | | |
| Top-point − Footpoint | 0.04 | 0.04 | 0.1 | 1277 |
| Midpoint − Footpoint | 0.00 | 0.01 | 0.1 | ” |
| Top-point − Midpoint | 0.04 | 0.03 | 0.1 | ” |
| **Off-limb blue-shifted** | | | | |
| Top-point − Footpoint | −0.05 | −0.06 | 0.2 | 162 |
| Midpoint − Footpoint | −0.07 | −0.07 | 0.2 | ” |
| Top-point − Midpoint | 0.02 | 0.02 | 0.1 | ” |
| **Off-limb red-shifted** | | | | |
| Top-point − Footpoint | −0.02 | −0.03 | 0.2 | 120 |
| Midpoint − Footpoint | −0.06 | −0.06 | 0.2 | ” |
| Top-point − Midpoint | 0.04 | 0.04 | 0.1 | ” |

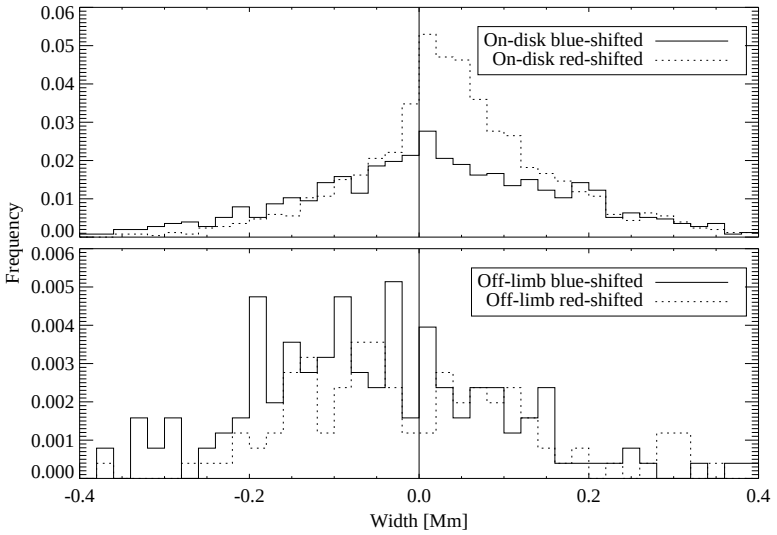


**Figure 4.23:** Difference in width between the top-point and the footpoint of the spicules calculated in the intensity images. The values are computed by averaging over 5 pixels.

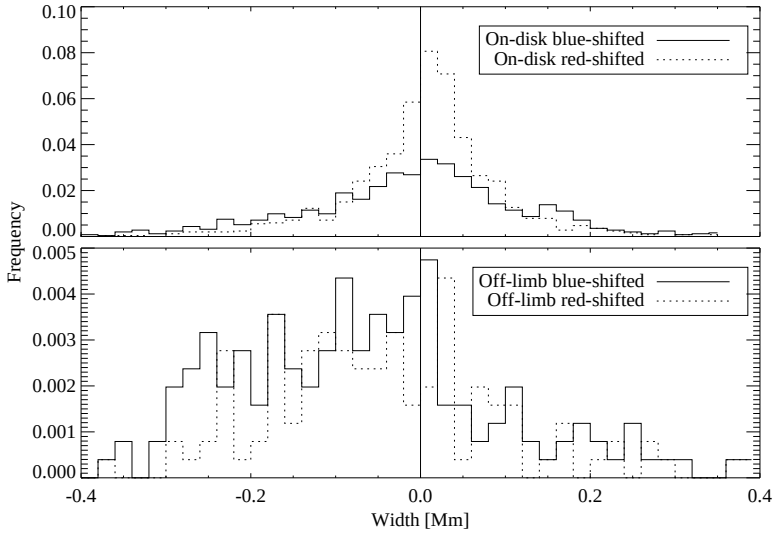


**Figure 4.24:** Difference in width between the middle and the footpoint of the spicules calculated in the intensity images. The values are computed by averaging over 5 pixels.

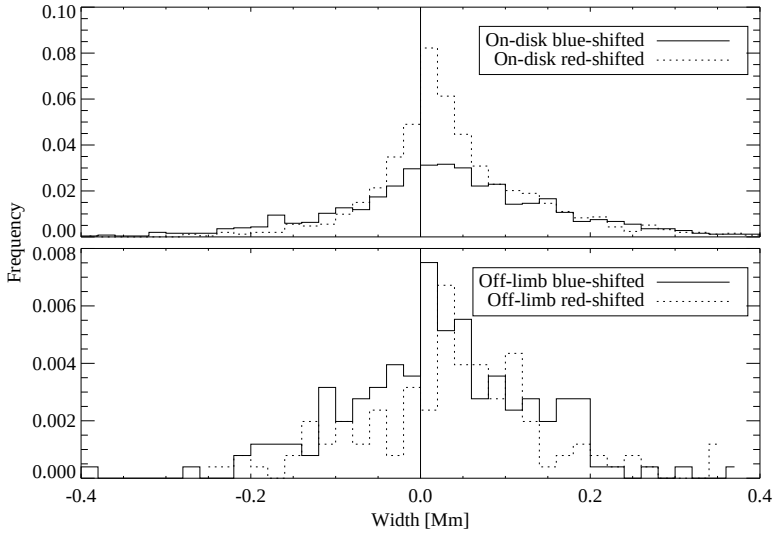


**Figure 4.25:** Difference in width between the top-point and the middle of the spicules calculated in the intensity images. The values are computed by averaging over 5 pixels.

**Table 4.2:** Table showing the variation of the physical width from the Doppler image along the length of the spicules.

| **On-disk blue-shifted** | $\mu$ [Mm] | $M$ [Mm] | $\sigma$ [Mm] | Count |
|---|---|---|---|---|
| Top-point − Footpoint | −0.02 | −0.02 | 0.1 | 971 |
| Midpoint − Footpoint | −0.03 | −0.02 | 0.1 | ” |
| Top-point − Midpoint | 0.004 | 0.0006 | 0.1 | ” |
| **On-disk red-shifted** | | | | |
| Top-point − Footpoint | −0.007 | 0.002 | 0.1 | 1277 |
| Midpoint − Footpoint | −0.009 | 0.0001 | 0.1 | ” |
| Top-point − Midpoint | 0.002 | 0.00000 | 0.1 | ” |
| **Off-limb blue-shifted** | | | | |
| Top-point − Footpoint | −0.002 | 0.005 | 0.1 | 162 |
| Midpoint − Footpoint | −0.005 | 0.003 | 0.1 | ” |
| Top-point − Midpoint | 0.003 | 0.004 | 0.1 | ” |
| **Off-limb red-shifted** | | | | |
| Top-point − Footpoint | 0.03 | 0.02 | 0.1 | 120 |
| Midpoint − Footpoint | −0.003 | 0.009 | 0.1 | ” |
| Top-point − Midpoint | 0.03 | 0.02 | 0.1 | ” |

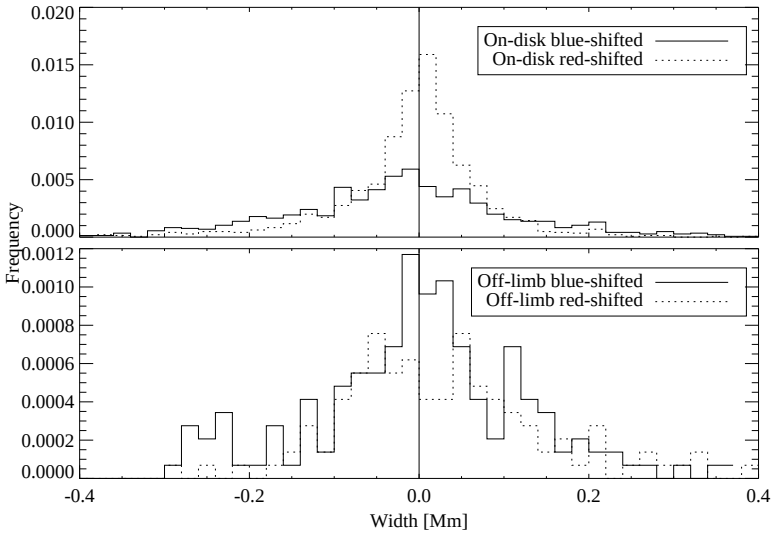


**Figure 4.26:** Difference in width between the top-point and the footpoint of the spicules calculated in the Doppler images. The values are computed by averaging over 5 pixels.

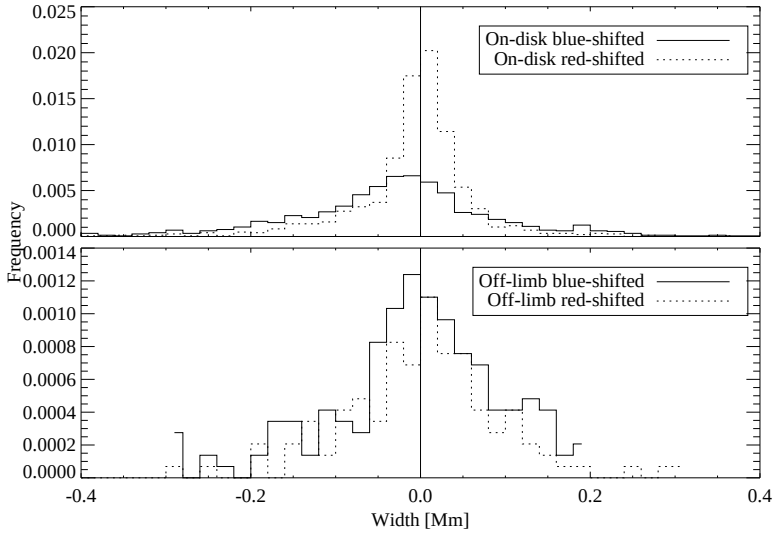


**Figure 4.27:** Difference in width between the midpoint and the footpoint of the spicules calculated in the Doppler images. The values are computed by averaging over 5 pixels.

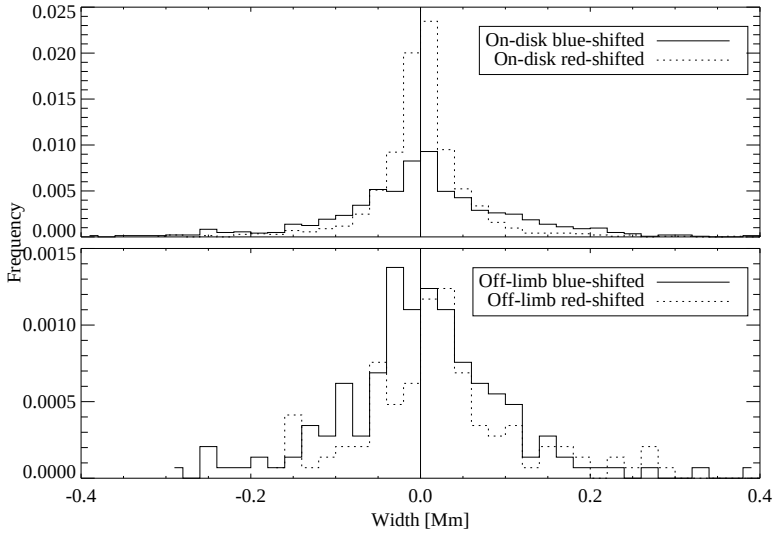


**Figure 4.28:** Difference in width between the top-point and the midpoint of the spicules calculated in the Doppler images. The values are computed by averaging over 5 pixels.

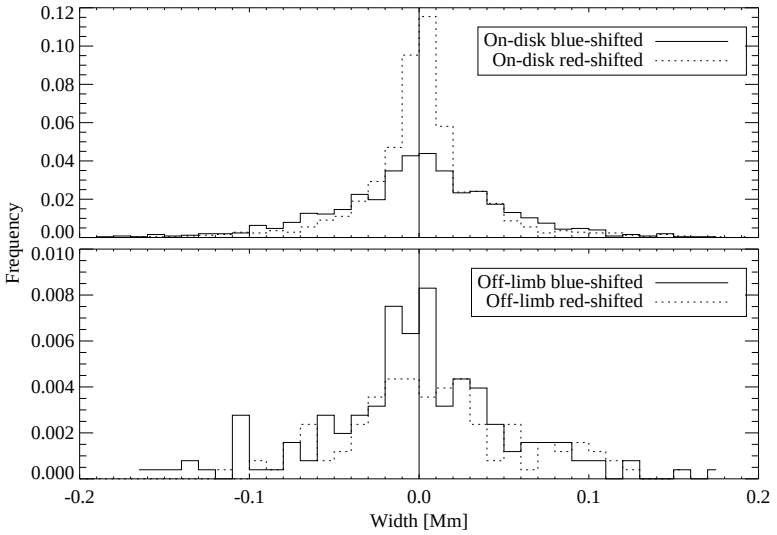


**Figure 4.29:** Average symmetry of the width profiles. The width symmetry of one pixel on the spicules line was computed as the difference between the distance from the maximum value to the half maximum values on either side. The average of the differences was computed only for spicules that had well defined width for more than 80 % of the pixels in the spicule line.

The average symmetry of the width profiles for each spicule is plotted in Fig. 4.29. The width symmetry of one pixel on the spicules line was computed as the difference between the distances from the maximum value to the half maximum values on either side. The average of the differences was computed only for spicules that had well defined width for more than 80 % of the pixels in the spicule line. The expectation value, median value, standard deviation and number of spicules in the histograms for the different groups are: on-disk blue-shifted: $-0.0009$ Mm, 0.0007 Mm, 0.05 Mm and 971. On-disk red-shifted: 0.001 Mm, 0.0003 Mm, 0.04 Mm and 1277. Off-limb blue shifted: $-0.003$ Mm, $-0.001$ Mm, 0.06 Mm and 162. Off-limb red-shifted: 0.006 Mm, 0.0003 Mm, 0.06 Mm and 120.

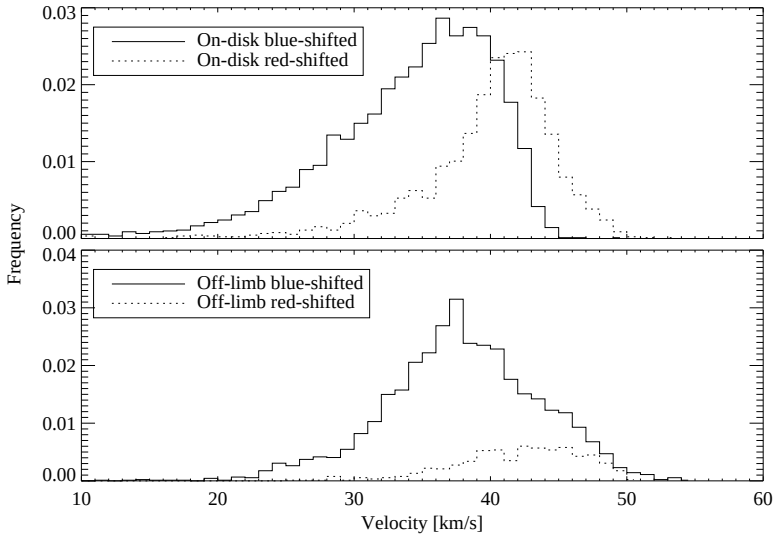


**Figure 4.30:** The average Doppler velocity for the spicules. The blue-shifted spicules are plotted with the absolute value of the velocity.

### 4.2.4 Doppler velocity

The average Doppler velocity for all the uniquely defined spicules is plotted in Fig. 4.30. The blue-shifted spicules are plotted with the absolute value of the velocity. The expectation value, median value, standard deviation and number of spicules in the histograms for the different groups are: on-disk blue-shifted: $-34$ km/s, $-35$ km/s, 6 km/s and 3385. On-disk red-shifted: 39 km/s, 41 km/s, 8 km/s and 1992. Off-limb blue shifted: $-38$ km/s, $-38$ km/s, 6 km/s and 3163. Off-limb red-shifted: 42 km/s, 43 km/s, 5 km/s and 605.

The variation of the Doppler velocity, for all spicules, along the length of each spicule is shown in Fig. 4.22. The velocity at one pixel position is the average value of all the velocities occurring on that pixel position.

The change of the Doppler velocity along the length of a spicule is plotted in Figs. 4.32, 4.33 and 4.34. These figures have the same differences plotted as Figs. 4.23, 4.24 and 4.25, respectively. The differences for the blue-shifted spicules have reversed sign, so a positive difference always means an increase in velocity. The difference is only calculated for spicules longer than 15 pixels. The statistical properties for the histograms are tabulated in table 4.3.

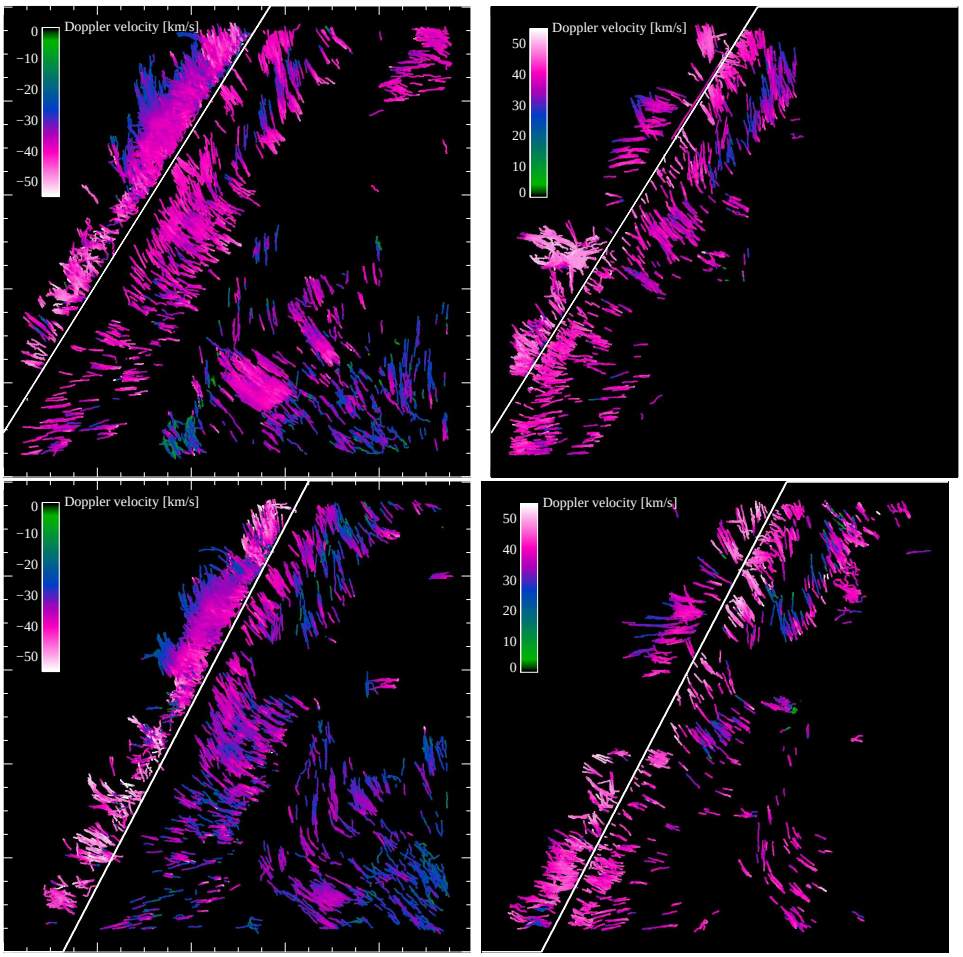


**Figure 4.31:** Variation of the Doppler velocity along the length of the spicules. All spicules from one group are superimposed on one image and the velocity at a pixel position is the average of all velocities occurring on that pixel position. Top left: the blue-shifted spicules from the first dataset. Top right: the red-shifted spicules from the first dataset. Bottom left: the blue-shifted spicules from the second dataset. Bottom right: the red-shifted spicules from the second dataset. All images: the image size is $59'' \times 59''$, the color bar indicates the velocities in km/s and the white inclined line marks the approximate position of the limb. The spicule lines are widened to 3 pixels in order to be more visible on paper.

**Table 4.3:** Table showing the variation of the Doppler velocity along the length of the spicules.

| **On-disk blue-shifted** | $\mu$ [km/s] | $M$ [km/s] | $\sigma$ [km/s] | Count |
|---|---|---|---|---|
| Top-point − Footpoint | −1.0 | −1.4 | 7.6 | 2985 |
| Midpoint − Footpoint | 0.8 | −0.1 | 6.5 | ” |
| Top-point − Midpoint | −1.8 | −1.6 | 5.3 | ” |
| **On-disk red-shifted** | | | | |
| Top-point − Footpoint | −1.5 | −1.5 | 7.0 | 1321 |
| Midpoint − Footpoint | −0.2 | −0.6 | 5.3 | ” |
| Top-point − Midpoint | −1.3 | −1.0 | 4.9 | ” |
| **Off-limb blue-shifted** | | | | |
| Top-point − Footpoint | −1.3 | −1.5 | 7.5 | 3047 |
| Midpoint − Footpoint | 0.7 | 0.3 | 5.3 | ” |
| Top-point − Midpoint | −1.9 | −1.7 | 5.0 | ” |
| **Off-limb red-shifted** | | | | |
| Top-point − Footpoint | 0.5 | −0.3 | 6.4 | 591 |
| Midpoint − Footpoint | 1.5 | 0.6 | 5.3 | ” |
| Top-point − Midpoint | −1.0 | −0.7 | 3.2 | ” |

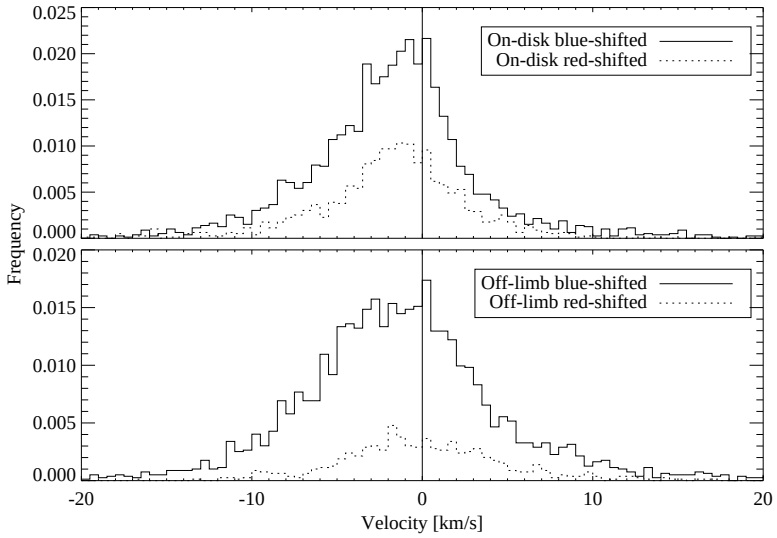


**Figure 4.32:** The change of the Doppler velocity between the top-point and the footpoint. The values are calculated by averaging over 5 pixels. The differences for the blue-shifted spicules have reversed sign, so a positive difference always means an increase in velocity.

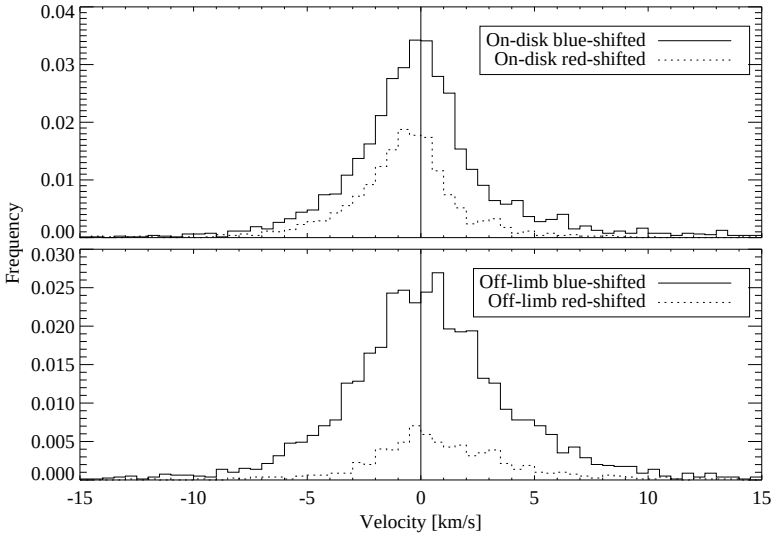


**Figure 4.33:** The change of the Doppler velocity between the midpoint and the footpoint. The values are calculated by averaging over 5 pixels. The differences for the blue-shifted spicules have reversed sign, so a positive difference always means an increase in velocity.

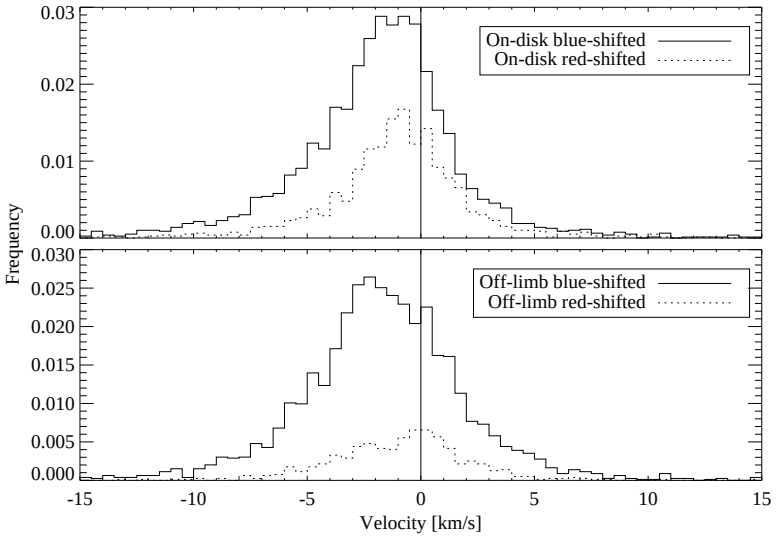


**Figure 4.34:** The change of the Doppler velocity between the top-point and the midpoint. The values are calculated by averaging over 5 pixels. The differences for the blue-shifted spicules have reversed sign, so a positive difference always means an increase in velocity.

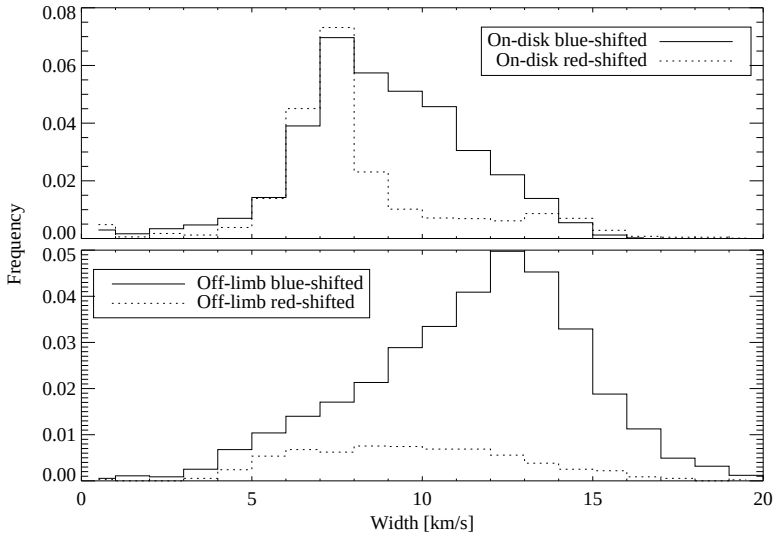


**Figure 4.35:** The average of the Doppler widths for each spicule. All unique spicules are included in the histograms.

### 4.2.5 Doppler width

The average of the Doppler widths for all unique spicules is plotted in Fig. 4.35 and the average is performed on all pixels in a spicule. The expectation value, median value, standard deviation and number of spicules in the histograms for the different groups are: on-disk blue-shifted: 8 km/s, 8 km/s, 2 km/s and 3385. On-disk red-shifted: 8 km/s, 7 km/s, 2 km/s and 1992. Off-limb blue shifted: 11 km/s, 11 km/s, 3 km/s and 3163. Off-limb red-shifted: 9 km/s, 9 km/s, 3 km/s and 605.

The variation of the Doppler width along the length of each spicule is shown visually in Fig. 4.36. The widths shown at one pixel location is the average value of all the widths occurring on that pixel position.

The change of velocity in the first and second half of each spicule is plotted in Figs. 4.37, 4.38 and 4.39. These figures have the same differences plotted as Figs. 4.23, 4.24 and 4.25, respectively. The difference is only calculated for spicules longer than 15 pixels. The statistical properties of the histograms for these figures are tabulated in table 4.4.

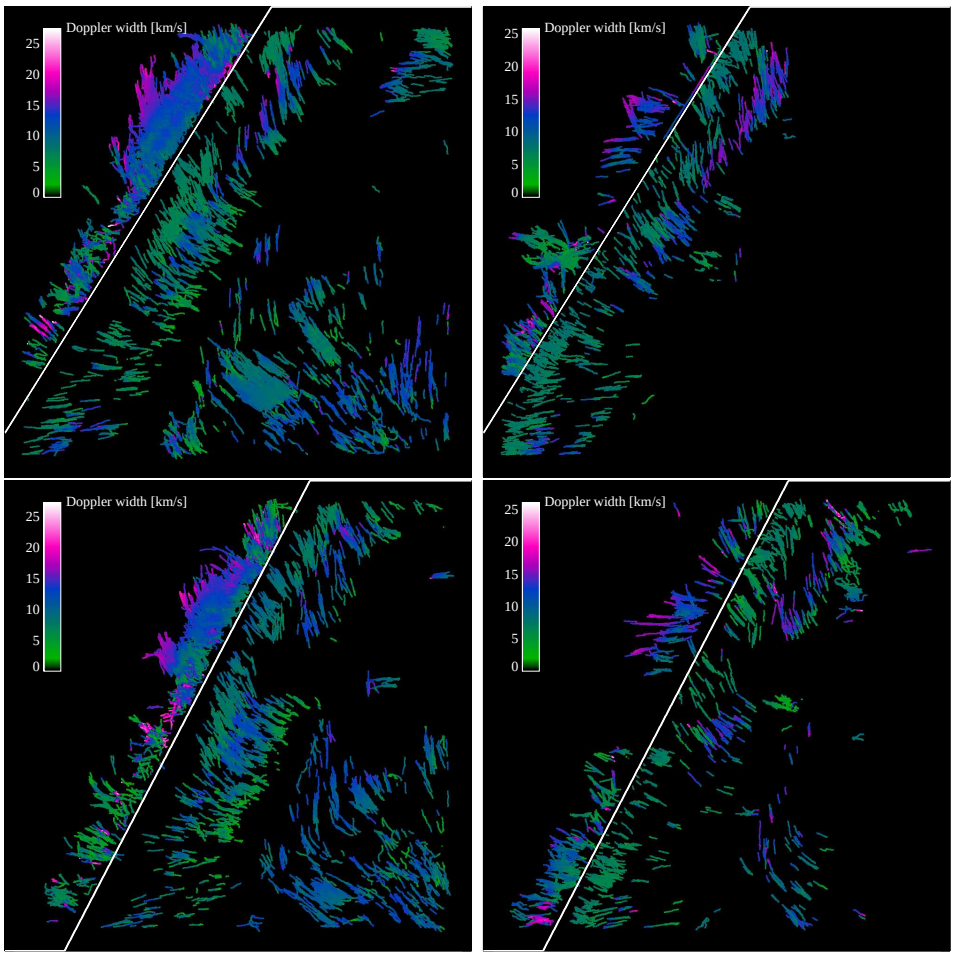


**Figure 4.36:** Variation of the Doppler width along the length for all spicules. All spicules from one group are superimposed on one image and the width shown at one pixel position is the average of all widths occurring on that pixel position. Top left: the blue-shifted spicules from the first dataset. Top right: the red-shifted spicules from the first dataset. Bottom left: the blue-shifted spicules from the second dataset. Bottom right: the red-shifted spicules from the second dataset. All images: the image size is $59'' \times 59''$, the color bar indicates the width in km/s and the white inclined line marks the approximate position of the limb. The spicule lines are widened to 3 pixels in order to be more visible on paper.

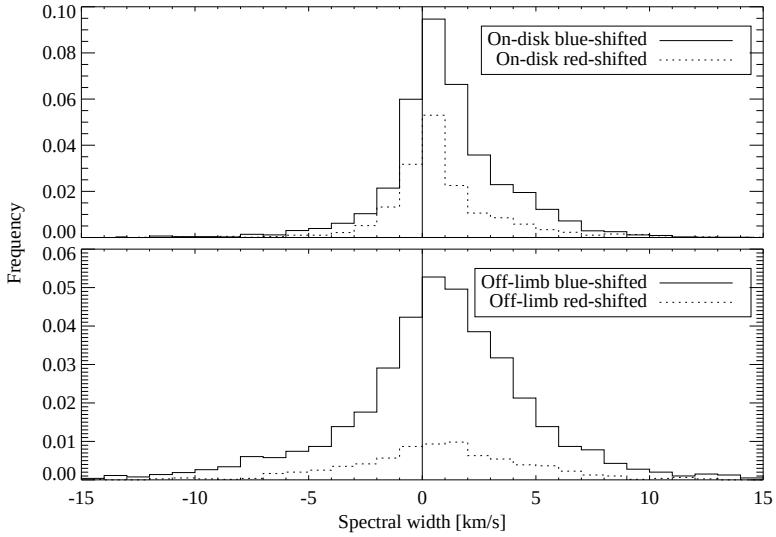


**Figure 4.37:** The difference in Doppler width between the top-point and the footpoint.

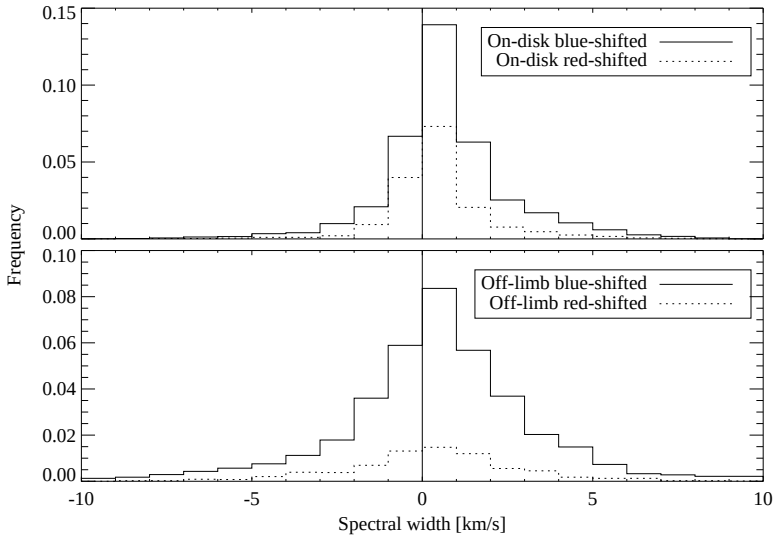


**Figure 4.38:** The difference in Doppler width between the midpoint and the footpoint.

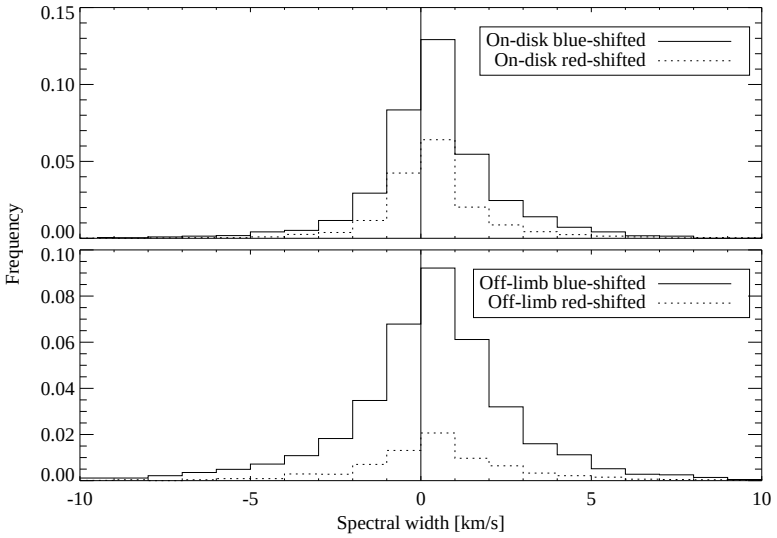


**Figure 4.39:** The difference in Doppler width between the top-point and the midpoint.

**Table 4.4:** Table showing the variation of the Doppler width along the length of the spicules.

| **On-disk blue-shifted** | $\mu$ [km/s] | $M$ [km/s] | $\sigma$ [km/s] | Count |
|---|---|---|---|---|
| Top-point − Footpoint | 1.1 | 0.8 | 2.7 | 2985 |
| Midpoint − Footpoint | 0.7 | 0.5 | 2.0 | ” |
| Top-point − Midpoint | 0.4 | 0.3 | 2.0 | ” |
| **On-disk red-shifted** | | | | |
| Top-point − Footpoint | 0.9 | 0.4 | 2.6 | 1321 |
| Midpoint − Footpoint | 0.5 | 0.3 | 1.7 | ” |
| Top-point − Midpoint | 0.4 | 0.2 | 1.9 | ” |
| **Off-limb blue-shifted** | | | | |
| Top-point − Footpoint | 0.7 | 0.9 | 4.4 | 3047 |
| Midpoint − Footpoint | 0.5 | 0.5 | 3.2 | ” |
| Top-point − Midpoint | 0.3 | 0.4 | 3.1 | ” |
| **Off-limb red-shifted** | | | | |
| Top-point − Footpoint | 0.8 | 0.8 | 4.0 | 591 |
| Midpoint − Footpoint | 0.3 | 0.3 | 2.9 | ” |
| Top-point − Midpoint | 0.5 | 0.4 | 2.7 | ” |

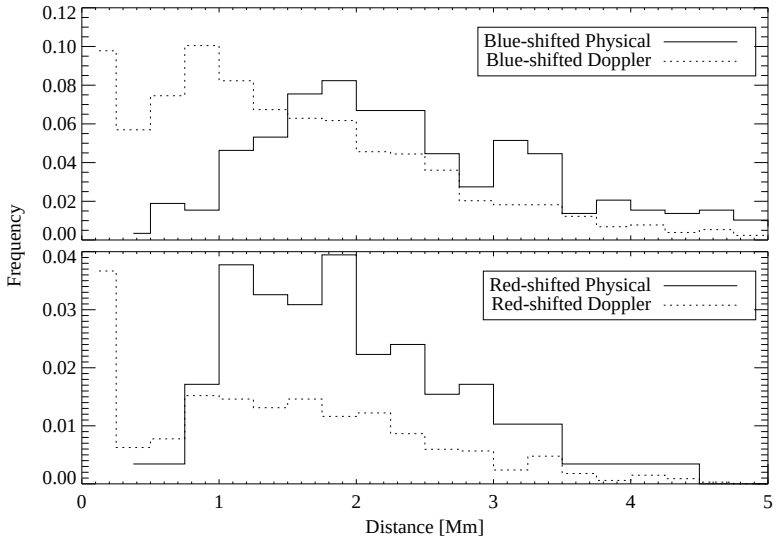


**Figure 4.40:** The footpoint-to-limb distances. Only the spicules that had well defined lengths are included in the histograms.

### 4.2.6 Limb distance

The footpoint-to-limb distances are plotted in Fig. 4.40. Only the spicules that had well defined lengths are included in the histograms. The expectation value, median value, standard deviation and number of spicules in the histograms for the different groups are: blue-shifted from intensity image: 2.5 Mm, 2.2 Mm, 1.2 Mm and 418. Blue-shifted from Doppler image: 1.5 Mm, 1.3 Mm, 1.1 Mm and 2799. Red-shifted from intensity image: 2.0 Mm, 1.8 Mm, 1.0 Mm and 165. Red-shifted from Doppler image: 1.4 Mm, 1.3 Mm, 1.1 Mm and 555.

The top-point-to-limb distance is plotted in Fig. 4.41. Only the spicules that had well defined lengths are included in the histograms. The expectation value, median value, standard deviation and number of spicules in the histograms for the different groups are: blue-shifted from intensity image: 3.8 Mm, 3.6 Mm, 1.3 Mm and 418. Blue-shifted from Doppler image: 2.8 Mm, 2.6 Mm, 1.2 Mm and 2799. Red-shifted from intensity image: 3.6 Mm, 3.4 Mm, 1.1 Mm and 165. Red-shifted from Doppler image: 2.9 Mm, 2.8 Mm, 1.2 Mm and 555.

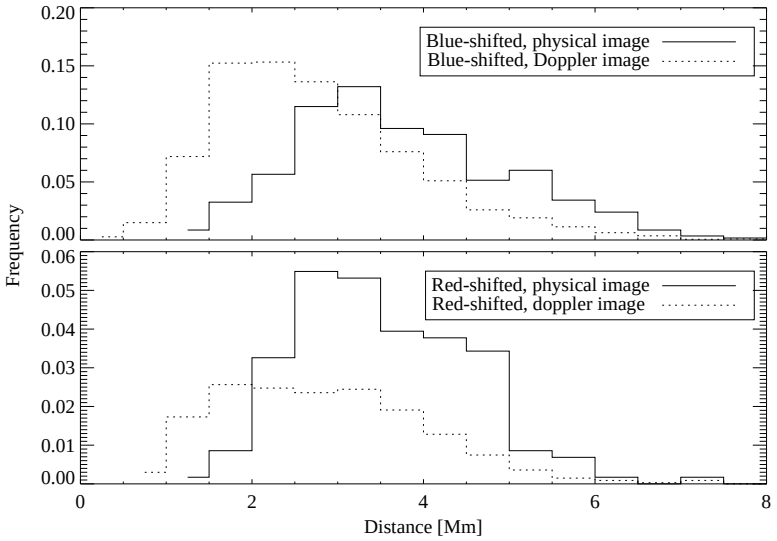


**Figure 4.41:** The top-point-to-limb distances. Only the spicules that had well defined lengths are included in the histograms.

### 4.2.7 Spicule angle with the limb

Each spicules angle with the limb normal is plotted in Fig. 4.42. A positive angle means the direction of the spicule is toward the top left of the image. The expectation value, median value, standard deviation and number of spicules in the histograms for the different groups are: on-disk blue-shifted: 13°, 17°, 30° and 3385. On-disk red-shifted: 6°, 7°, 31° and 1992. Off-limb blue shifted: 6°, 10°, 32° and 3163. Off-limb red-shifted: −4°, −10°, 29° and 605.

### 4.2.8 Spicule curvature

The difference in average angle between the first third and last third of the spicules is plotted in Fig. 4.43. The expectation value, median value, standard deviation and number of spicules in the histograms for the different groups are: on-disk blue-shifted: 14°, 9°, 15° and 3385. On-disk red-shifted: 10°, 6°, 13° and 1992. Off-limb blue shifted: 18°, 12°, 19° and 3163. Off-limb red-shifted: 15°, 10°, 17° and 605.

The difference in average angle between the first third and last sixth of the spicule is plotted in Fig. 4.43. The expectation value, median value, standard deviation and number of spicules in the histograms for the different groups are: on-disk blue-shifted: 17°, 13°, 17° and 3385. On-disk red-shifted: 14°,

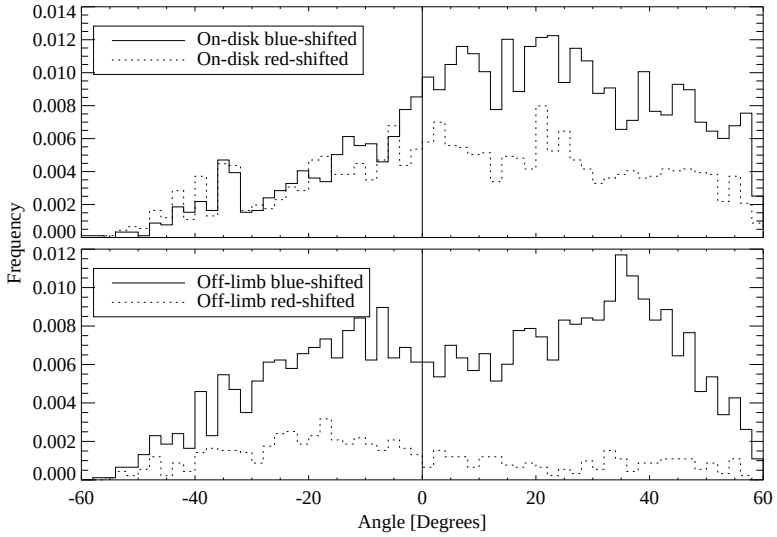


**Figure 4.42:** The spicules angle with the limb normal. A positive angle means the direction of the spicule is from toward the top left part of the image.

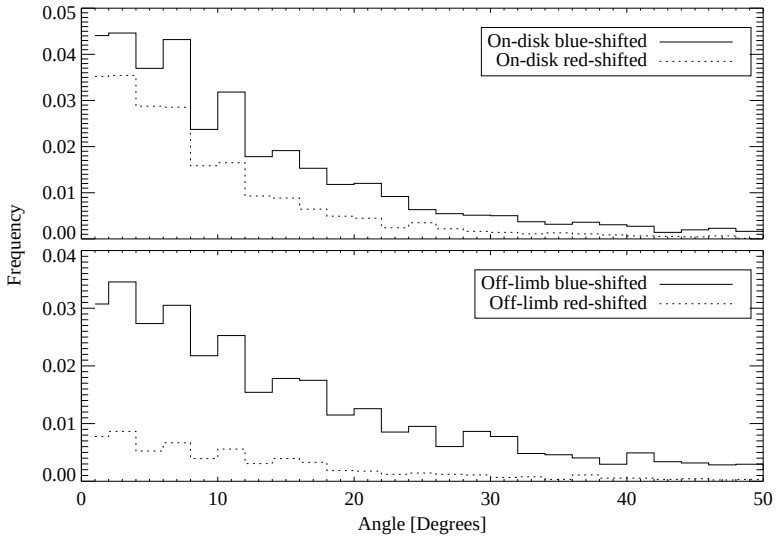


**Figure 4.43:** Difference in average angle between the first and last third of the spicule.

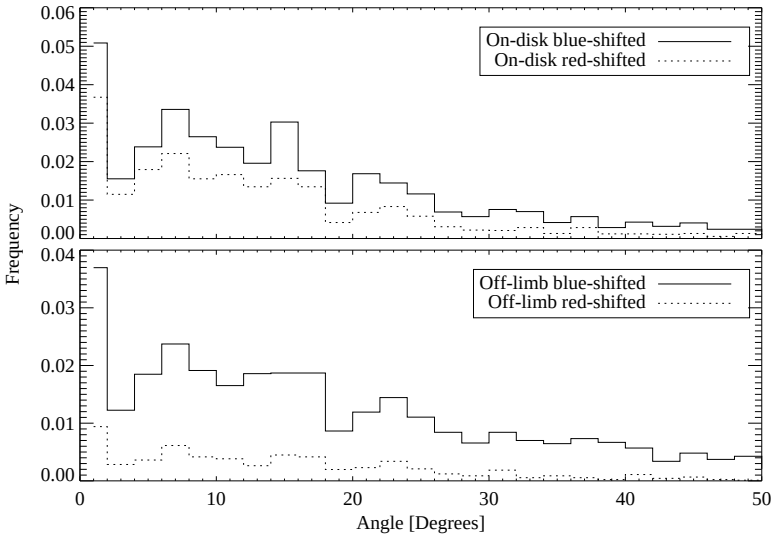


**Figure 4.44:** Difference in average angle between the first and last sixth of the segment.

11°, 16° and 1992. Off-limb blue shifted: 24°, 17°, 23° and 3163. Off-limb red-shifted: 19°, 14°, 21° and 605.

### 4.2.9 Lifetime

The lifetime of 160 spicules, 40 in each group, are plotted in Fig. 4.45. The expectation value, median value, standard deviation and number of spicules in the histograms for the different groups are: on-disk blue-shifted: 42 s, 38 s, 26 s and 40. On-disk red-shifted: 40 s, 25 s, 25 s and 40. Off-limb blue shifted: 63 s, 50 s, 42 s and 40. Off-limb red-shifted: 61 s, 50 s, 34 s and 40.

## 4.3 Spicule Type II Properties in the Literature

Since type II spicules were discovered with Hinode in 2006, no article published before 2006 contains statistics on the properties of type II spicules. Since the discovery, there have been published a few articles that provides spicule statistics and they are briefly discussed below.

**De Pontieu et al. (2007b)**

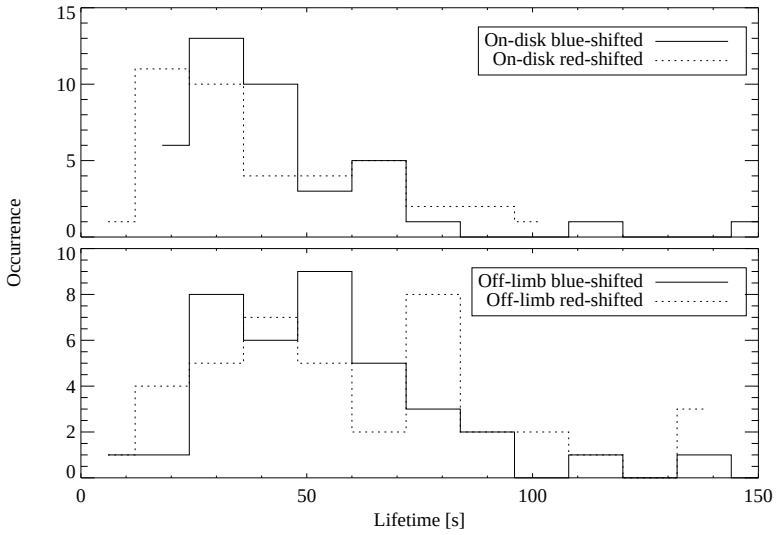


**Figure 4.45:** The lifetimes of 40 spicules in each group.

De Pontieu et al. (2007b) used observations from the Solar Optical Telescope (SOT) Broadband Filter Imager (BFI) on the Hinode satellite, to identify a new type of spicules, the type II spicules. The observations were made in the Ca II 3968 Å line at one spectral position with a spatial resolution of 0.16″. The FWHM of the transmission profile for the Ca II filter is fairly broad with a FWHM of 2.2 Å. The cadence was between 4 and 11.2 s and the observations were from an active region, a coronal hole and the quiet Sun. There is no information on the number of spicules that made up the statistics in the article.

### Bjølseth (2008)

Bjølseth (2008) measured the apparent mean velocities and lifetimes of 200 type II spicules from two different datasets taken by Hinode SOT/BFI in 2007 with a 5 s cadence. The observations were made in the Ca II 3968 Å line at one spectral position with a spatial resolution of 0.16″.

### Pasachoff et al. (2009)

Pasachoff et al. (2009) analyzed simultaneous data from the SST with the Solar Optical Universal Polarizer (SOUP) and from NASA's Transition Region and Coronal Explorer (TRACE; Handy et al., 1999) for the quiet Sun

at the limb from 2006. The spectral line H$\alpha$ was scanned at 5 line positions with a cadence of 49.2 s. The SOUP filter has a FWHM of the transmission profile of 7.8 pm in narrow mode. The reported resolution was 0.2″. The authors analyzed 40 spicule like events, in which 29 faded out at maximum height. Although the fading behavior is characteristic of type II spicules , the cadence is close to the reported average lifetime and therefore the data is not suitable for detailed study of the type II spicules. The results are consistent with previous spicules type I studies and type I spicules most likely make up the statistics with the possibility of overlapping type II spicules.

**Rouppe van der Voort et al. (2009)**

Rouppe van der Voort et al. (2009) studied RBEs on the disk in both the H$\alpha$ and the Ca II 8542 Å spectral line in observations obtained from the SST with CRISP. The authors achieved a spatial resolution of 0.17″ for Ca II and 0.23″ for at least half of the images in the datasets. The Ca II line was scanned at 29 positions and the H$\alpha$ line at 25 positions for each time step. The cadence was 6.7 s and 11 s for H$\alpha$ and Ca II, respectively. The authors identified 413 RBEs in the Ca II data and 608 in the H$\alpha$ data with an automatic detection algorithm, and the physical properties were measured for each RBE individually, and some properties on a subset manually. The target area was a coronal hole very close to the disk center.

**Anan et al. (2010)**

Anan et al. (2010) studied spicular jets over a plage region from the SOT/BFI instrument on Hinode in the Ca II H 3968 Å line from 2007 at one spectral line position. The resolution was 0.16″ and the cadence was 45 s. The authors identified 169 spicules among which 125 showed successive up and down motion, 22 faded out and 22 were "irregular". The authors disregarded the spicules with lifetimes shorter than 90 s. The cadence is insufficient for detailed study of type II spicules and combined with the disregarding of short lived spicules, type I spicules most like make up their statistics.

**Tavabi et al. (2011)**

Tavabi et al. (2011) analyzed polar spicules seen in Hinode SOT/BFI data from 2008. The observations are in the Ca II H 3968 Å line with a 8 second cadence and spatial resolution of 0.16″. The authors did not analyze the

spicules individually but measured widths using Fourier analysis on the intensity retrieved from a line parallel with the limb. This causes both type I and type II spicules to be in their statistics. The Fourier analysis can identify frequently occurring widths, but not provide constraints of the upper/lower width of the spicules.

#### Nishizuka et al. (2011)

Nishizuka et al. (2011) analyzed chromospheric spicules with Hinode SOT/BFI data on-disk and off-limb from 2006. The spatial resolution was 0.16″ and the cadence was 55 s. The authors analyzed 200 jets and the statistical properties found match well the reported properties of type I spicules. The cadence is too slow to resolve type II spicules temporally and study the type II spicules in detail.

## 4.4 Discussion of the Results

#### The Detected Number of Spicules and their Location

As seen in Fig. 4.14, 59 % of all the detected spicules were found on the disk of the Sun. This is contradictory to the visual impression one gets by looking at Fig. 3.7 where there seem to be more spicules off-limb. The reason for this bias is that the off-limb spicules often are overlapping one another. This creates detected spicule lines that start on one spicule and end on another. This line is often very curved and is removed by the curvature filter after the detection, illustrated in Fig. 3.5. The on-disk spicules appear often more separated from each other with less overlap, which is advantageous in the detection algorithm.

Of the detected spicules 72 % are blue-shifted. This bias is most profound off-limb where 84 % of the detected spicules are blue-shifted. Assuming spicules are moving outward in the solar atmosphere this bias was expected to be strongest on-disk, because the disk is facing the observers, not off-limb where the surface-normal is perpendicular to the line-of-sight direction. The hypothesis for the bias is a geometrical effect: assume that the spicules are moving outward in the atmosphere. Then the blue-shifted spicules and spicules with no Doppler-shift are closer to the observer along the line-of-sight, hiding the red-shifted spicules as illustrated in Fig. 4.46. This hypothesis is given observational support from Fig. 4.16. In the images on the left column showing the blue-shifted spicules, we see that off-limb there

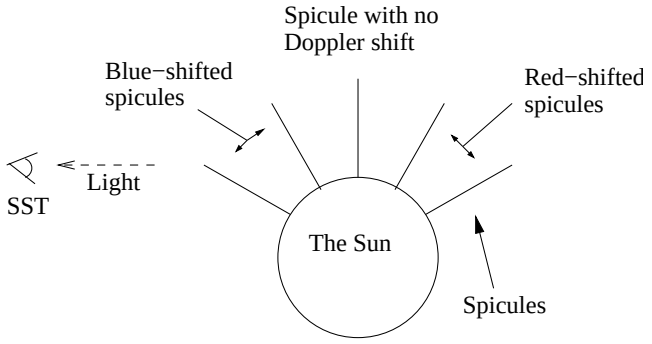


**Figure 4.46:** Drawing for the hypothesis of why there are so few red-shifted spicules detected. Features not drawn in relative scale.

are more spicules in the upper half of the images than in the lower half. This is opposite for the red-shifted spicules; more red-shifted spicules are detected where there are fewer blue-shifted spicules.

As illustrated in Fig. 4.16 almost no red-shifted spicules are detected in the bottom right corner where the active region is. This comes as no surprise because red-shifted spicules detected there were masked out due to coronal rain that was detected as spicules. However, the effect of the masking is that the red-shifted spicules on-disk are primarily from regions with little magnetic activity, the quiet Sun, while the blue-shifted spicules are from both the active region in the corner and the quiet Sun elsewhere. De Pontieu et al. (2007b) reported that the spicule properties were different in active regions compared to the quiet Sun, which means that this observation is important for the discussion of the physical properties measured on-disk. No active region appeared after some days when the position of the limb on the day of the observations had rotated closer to disk center, which means that the off-limb spicules came from the quiet Sun.

Measurements in the intensity images yielded the most amount of spicules with ill-defined lengths and ill-defined widths compared to measurements in the Doppler images, especially off-limb, where nearly all spicules had ill-defined lengths and widths. The reason for this is that the off-limb spicules often have the footpoint where the intensity from the limb is on the same level as half the maximum intensity of the spicule, preventing the intensity of the spicule to drop below its half maximum value. This also causes the widths of often more than 20 % of the pixels on the spicule line to be ill-defined, with the result that the spicule is flagged as having ill defined (average) width. As described in section 3.4.1, when one of the end points could not be found by the FWHM procedure, the corresponding end point from the detected line was used. Therefore the lengths of the spicules shown

in Figs. 4.16, 4.22, 4.31 and 4.36 must not be taken as *the* projected lengths of the spicules, but rather as an estimate. However, the detected line provided a good measure of the length with a small difference compared to the length when measured with the FWHM procedure.

### Projected physical length

The different groups of spicules have approximately the same mean length, although the on-disk red-shifted spicules have a slightly shorter mean length, and the off-limb red-shifted spicules a slightly longer mean length. Almost no spicules are longer than 3 Mm; most spicules are between 1 Mm and 2.5 Mm in length.

De Pontieu et al. (2007b) observed that spicules type II were shortest in active regions, with typical lengths between 1 and 2 Mm, and longer in coronal holes and in the quiet Sun where they could reach lengths of several megameters. Taking into account that the red-shifted spicules on-disk are mostly from the quiet Sun, this is contradictory to what is shown in Fig. 4.17. However, one can observe in Fig. 4.16 that the red-shifted spicules on-disk appears to be located closer to the limb compared to the blue-shifted spicules. Close to the limb the fibrils and spicules are directed almost parallel with the line-of-sight direction resulting in a small projected length which could explain this discrepancy.

Rouppe van der Voort et al. (2009) measured the lengths of RBEs to be a symmetrical distribution centered on 3.2 Mm with almost all RBEs between 2.5 and 4.5 Mm. The measured lengths in this thesis correspond well with the lengths reported by De Pontieu et al. (2007b) and Rouppe van der Voort et al. (2009). The longer lengths for the RBEs in Rouppe van der Voort et al. (2009) compares well because their target area was a coronal hole where the spicules are reported to be longer by De Pontieu et al. (2007b).

The detection length-threshold of 15 pixels, corresponding to the length of 0.65 Mm, is clearly seen in Fig. 4.17, but spicules could become shorter when measuring the positions of their half maximum values of the end points. Both on-disk and off-limb, the histograms with the top point closer to 0.65 Mm have the steepest slope on the left side and a more asymmetrical histogram compared to the histograms where the top point is further away from 0.65 Mm. This indicates that many shorter spicules were rejected by the length threshold and this was confirmed by visual inspection of the Doppler images.

The difference in length when measured in the intensity image and in the Doppler image provides an indication on how accurate the measurements in

the intensity images are. On-disk, the expectation value of the difference is just below zero and the histogram is fairly symmetric, while off-limb it is above zero and very asymmetrical; the intensity length is longer than the Doppler length.

From the results it can be concluded that most spicules are between 1 and 2.5 Mm in length, irrespective of their location in either active regions or quiet Sun, and that almost no spicules are longer than 4 Mm. Due to the length-threshold and projection effects no lower limit can be found for the length.

### Projected physical width

The spicules on-disk have the smallest mean width with the red-shifted spicules being the narrowest. In the histograms there is a sharp cutoff close to 0.1 Mm for the on-disk spicules. This width corresponds to about three pixels, and three pixels are the minimum amount one need in order to create a width intensity profile that can be detected as a spicule. The appearance of extremely thin spicules not detected in the images and the sharp cutoff in the histograms indicates that the lower boundary for the widths cannot be found due to limitations by the spatial resolution of the SST.

The smallest width for the off-limb spicules is 0.2 Mm, a higher minimum value than compared with on-disk spicules. The maximum width is the same for all groups and is about 0.7 Mm. The spicules are in general between 0.25 and 0.55 Mm in width except for the on-disk red-shifted which are between 0.15 and 0.35 Mm. The hypothesis for the wider average widths off-limb is that the large amount of off-limb spicules causes many of them to be so close side by side in appearance that the intensity value does not drop below the half maximum value between the spicules in the width intensity profiles. When measuring the width with the FWHM procedure one therefore measures on more than one spicule.

A crude way to determine whether the width was measured on multiple spicules appearing as one was introduced with the measurement of the average width profile symmetry (section 3.4.1) plotted in Fig. 4.29. By visual inspection of some isolated spicules on-disk it was found that the average width profile was fairly symmetrical. If however, two spicules are close together side by side, the distance from the maximum value to the side with the neighboring spicule will be longer than the distance from the maximum values to the side with no extra spicule. The outcome of the extra spicule will be an extra count in a bin in the histogram away from zero. In the symmetry histograms off-limb there are taller bins with a distance larger than

$\pm 0.05$ Mm from zero than for the on-disk histograms. This is interpreted as follows: off-limb spicules are more often so close together that the width measurement done in this thesis often measures the width on more than one spicule at the same time as compared to spicules on-disk.

De Pontieu et al. (2007b) observed the widths of type II spicules to be $\leq$ 200 km. However, it is not specified in detail in the article how these widths were measured, where on the spicule they measured or on how many spicules that were measured on. Tavabi et al. (2011) measured widths with Fourier analysis along a line parallel to the limb. The authors found peaks in the amplitude spectra corresponding to widths of 220 km and 360 km and claim that this corresponds to spicules of type II.

There is on average very little change in width in the first and second half of a spicule. Many spicules show a change of width, to larger or smaller widths, but the expectation value for the change is close to zero. These measurements were performed on all unique spicules. The symmetry histograms, Fig. 4.29, indicate that on many off-limb spicules the width of one spicule was computed including the spicules appearing close by. Consequently, the computed change in width is less accurate for the off-limb spicules.

The width as function of location and Doppler shift is shown in Fig. 4.22. The most pronounced visible effect is the narrow widths of the on-disk red-shifted spicules from the first dataset, but this visual effect is not present in the second dataset. The blue-shifted spicules off-limb in the top half of the image they appear to become wider with increasing limb distance. This is partly due to the width being exactly equal to one close to the limb, which is the fallback width if the width could not be determined at a pixel position on the spicule line. No particular trend in increase or decrease of the widths can be seen and this corresponds to the results displayed in table 4.1

It is difficult to directly compare measurements made in different spectral lines and with different techniques. Although the widths reported here are wider, they fit well with the previously reported widths. Due to the large amount of spicules that have been studied systematically and individually, these widths provide better constraints than the previous studies.

### Doppler velocity

All groups of spicules have close to the same mean Doppler velocity. The spicules on-disk has a long tail toward zero velocity and a more steep tail towards higher velocities. The hypothesis for this long tail is a geometrical effect. Assume spicules are moving with roughly the same velocity with

different directions compared to the line-of-sight direction. Then the movements will create a continuous range of velocities from high, when parallel to line-of-sight, to low, when perpendicular to line-of-sight. If the general direction of the spicules are outward, not to far away from the surface normal, this effect will be strongest on-disk where a range of surface normals exists, compared to on-limb where there is only one.

The spectral wavelength range for these observations was $\pm 1.2$ Å, corresponding to $\pm 55$ km/s. It is quite possible that this spectral range is not far enough out in the wing of the H$\alpha$ to resolve the fastest spicules. Because the spicule spectra were fairly symmetric the expectation value often coincides, or are very close, to the maximum value of the spectra. An improvement would be to add a test-check that a maximum value on the spectra exists. This, along with the improvement suggested in the next section, will make it possible to exclude spicules from the statistics that don't have well resolved spectra.

Although many spicules show a change in Doppler velocity in the first and second half, both to higher and lower velocities, the expectation value for the changes are close to zero. No clear trend of different velocities in different areas is apparent in Fig. 4.31. The spicules off-limb in the lower half of the images appear to have a higher Doppler shift, but this may well be related to local conditions in the area, not necessarily an indication of a systematic effect.

Rouppe van der Voort et al. (2009) measured the Doppler velocities of RBEs to be a symmetric distribution centered around 35 km/s, with most velocities between 28 km/s and 42 km/s. The measured Doppler velocities in this thesis fit very well with these reported ones. However, due to the limited spectral range no upper limit on the Doppler velocities can be found.

### Doppler width

The histograms with the Doppler widths, Fig. 4.21, look different for each of the groups. On-disk the red-shifted spicules have a more narrow histogram and off-limb the blue-shifted spicules peaks at a wider width compared to the red-shifted spicules. The narrow histogram of the on-disk red-shifted spicules is due to the countermeasure made to prevent the limb darkening affecting the spicule spectra. In Fig. 4.16 it is seen that the red-shifted spicules on-disk are on average appearing closer to the limb compared to the blue-shifted spicules, and the effect of the subtraction is clearly visible in Fig. 4.36. The result is an aggregation of more narrow widths.

As mentioned, the spectral range of the CRISP scan was ±1.2 Å, corresponding to ±55 km/s. This range is not large enough to fully contain a spectrum from a spicule with a higher Doppler-shift than ∼ 40 km/s, because due to the width of the profile, some values of the spectrum will be larger than ±55 km/s. As a result, spicules with such high velocities will get a narrow computed Doppler width. This artificially induced correlation is clearly visible in Fig. 4.47 and means that the lower limit of the Doppler widths cannot be determined by computing the width by using the standard deviation, this is because that method cannot determine whether the spectra was fully contained in the spectral range or not. As a result, the spicules with not fully resolved spectra cannot be isolated and removed from the statistics. Still, most spicules detected have velocities lower than 40 km/s which means that spicules with well resolved spectra dominates the statistics.

One improvement which could be implemented in order to compensate for the limb darkening and also help finding the lower limit on the Doppler width, is to compute the Doppler widths with the FWHM procedure instead of as the standard deviation of the profile. The advantage of this procedure is that it is less affected by a long tail as seen by the dashed line in Fig. 3.10 and it can determine whether the spectra was resolved or not by checking the existence of both half maximum values. The standard deviation measure was used in Rouppe van der Voort et al. (2009) and was also used in this thesis in order to directly compare the results.

Rouppe van der Voort et al. (2009) measured the widths to be a symmetric distribution centered around 13 km/s having the bulk of the spicules between 9 km/s and 16 km/s. The measurements of the Doppler width here fit in well with what Rouppe van der Voort et al. (2009) reported.

### Limb distance

As explained in section 4.4, the bright limb causes problems when measuring the length and width of a spicule off-limb that is close to the limb. This explains the sharp cutoff of the minimum footpoint-to-limb distance measured in the intensity images close to 0.8 Mm. When measuring the distance in the Doppler image there appears to be no minimum footpoint-to-limb distance. This was expected because at the limb we see spicules from a range of distances from us, along the line-of-sight, all being superimposed on an image from the plane of the sky. The area right below these spicules are both on the visible part of the disk and behind the limb. With no means of determining the area on-disk below a spicule it is not possible to determine a minimum footpoint-to-limb distance, if such a distance exists.

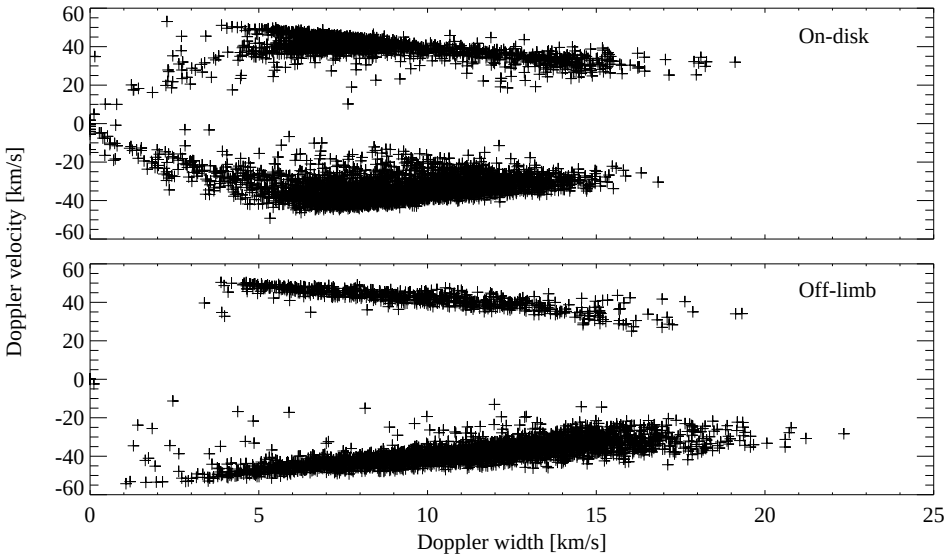


**Figure 4.47:** Plot showing the artificially induced correlation between the Doppler width and the Doppler velocity due to the limited spectral range of the CRISP scan of ±1.2 Å. Top panel: on-disk spicules. Bottom panel: off-limb spicules.

The maximum footpoint-to-limb distance appears to be around 5 Mm with most spicules having the footpoint closer than 3.5 Mm. The maximum top-point-to-limb distance is about 8 Mm, with nearly all top-points being closer than 6 Mm to the limb.

The distances to the limb are highly dependent on the definition of the position of the limb. In this thesis the limb was defined to be where the disk intensity had dropped to half its average disk value at the spectral position −1.2 Å. The estimated distance from where the limb has disk intensity to where is has off-limb intensity is about 1.3 Mm.

From Figs. 4.40 and 4.41 it can be concluded that most spicules have their footpoint closer than 3.5 Mm to the limb and their top-point between 2.5 Mm to 5.5 Mm from the limb.

### Spicule direction and curvature

The average direction of all groups of spicules, not including the off-limb red-shifted spicules, are toward the top left in all images. Off-limb there are more spicules in the direction toward the bottom left of the image. No clearly preferred angles, or range of angles, are visible in the histograms.

The mean direction of the detected spicules is similar to the mean direction of the fibrils seen in spectral positions closer to the line center. This can be seen by combining Fig. 3.9 and Fig. 4.16. The naturally occurring separation line on-disk, overplotted by a straight line in Fig. 3.9, which separates the active region from the quiet Sun close to the limb is also observed in Fig. 4.16 as a thin region parallel to the limb where no spicules are detected. Rouppe van der Voort et al. (2009) commented that the path of the RBEs was roughly aligned with the fibrils, but that there was no one-to-one relation.

The inclination data from this thesis is only valid for the small FOV observed and cannot be generalized to outside the FOV. Pasachoff et al. (2009) comment that it would be interesting to consistently measure the inclinations of spicules over a solar-activity cycle, and to compare the distribution with the expected magnetic field geometry in the overlying corona. The observations in this thesis were from 2009 when the Sun was in a minimum in the activity cycle.

The majority of the spicules have a curvature less then 30° when using the average angle of the first and the last third of the spicule. The histograms in Fig. 4.43 has the shape of an exponential distribution with the maximum value close to 0°. To check if the spicules are arched or winded, at least at the ends, the histograms where the average angle between the first and last sixth of the spicule are also showed. The relative similar appearance of the histograms in Figs. 4.43 and 4.44 is an indication that the spicules only are arched and not winded.

### Lifetime

The lifetimes measured range from 6.4 s, the cadence of the observations, to a maximum of about 150 s, with the bulk of the spicules having lifetimes between 10 s and 100 s.

De Pontieu et al. (2007b) measured the lifetimes to be between 20 s and 110 s in a coronal hole and also commented that the lifetimes are shorter in active regions; having an average of around 35 s. Rouppe van der Voort et al. (2009) measured lifetimes of coronal hole RBEs to be between 6.7 s, the cadence of their observations, to about 70 s. The lifetimes measured in this thesis from the quiet Sun compares well with the previous results. The short lifetimes measured here, in De Pontieu et al. (2007b), in Bjølseth (2008) and Rouppe van der Voort et al. (2009) emphasizes the importance of having high cadence when observing spicules.

# Chapter 5

# Conclusion and Outlook

We have analyzed spicules in the wings of the spectral line H$\alpha$ with the CRISP instrument at the SST. In both the blue and red wing of H$\alpha$ we observe the spicules on-disk as thin, dark and elongated streaks that appear suddenly, have high apparent longitudinal velocities and often exhibit transverse displacement before disappearing quickly. This characteristic motion is similar to what Langangen et al. (2008b) and Rouppe van der Voort et al. (2009) reported for RBEs close to disk center. Langangen et al. (2008b) suggested the RBEs as the on-disk counterpart of the Hinode type II spicules seen off-limb. This suggestion was based on similarities in lifetime, spatial extent, sudden disappearance, location near the network and the observation that RBEs only show absorption in the blue wing corresponding to an up flow of gas. By using observations with a higher spatial and temporal resolution, Rouppe van der Voort et al. (2009) made the connection between the type II spicules and RBEs much stronger. The authors showed, that in addition to the similarities found by Langangen et al. (2008b), the transverse velocity, apparent longitudinal velocity, occurrence rate and increase in Doppler velocity from the footpoint to the top-point were similar to what De Pontieu et al. (2007b) had reported for type II spicules. The authors use of an automatic detection code which greatly increased the number of spicules in the statistics available, and the authors also provided measurements of the Doppler velocity and Doppler width of the spectral profile for the spicules.

The similarities of the physical properties for the spicules seen on-disk in this thesis compare well with what Rouppe van der Voort et al. (2009) reported. This includes: apparent length, Doppler velocity, Doppler width, lifetime and direction similar to the fibrils that are visible closer to the line center. With all the properties measured for spicules in this thesis closely resembling

the RBE properties, and having the characteristic motion identical to RBEs, this further strengthens the case that RBEs are the on-disk counterpart of Hinode type II spicules. This verification concludes primary goal 1 of this thesis.

The observations analyzed in this thesis made it possible to simultaneously study the on-disk spicules and the off-limb spicules. The off-limb spicules appear as thin, bright and elongated streaks that show the same characteristic motion as the spicules on-disk. All the measured physical properties for the off-limb spicules match very well with the properties for the on-disk spicules. We therefore conclude that off-limb spicules seen in the wings of H$\alpha$ are the same type of spicules as seen on-disk in H$\alpha$. This strongly indicates that the off-limb spicules are the same phenomena as the Hinode type II spicules, and this completes primary goal 2 of this thesis. The thesis hypothesis, which stated that all spicules seen in the wings of H$\alpha$ are the type II spicules seen by Hinode, holds true.

From our data we are confident of the following facts concerning spicules type II from active regions and the quiet Sun:

- The projected lengths are shorter than 3.5 Mm.
- The projected widths are less than 0.6 Mm.
- The footpoints are closer than 5 Mm to the limb.
- The top-points are closer than 7 Mm to the limb.
- Spicules are curved.
- Spicules have lifetimes shorter than 150 s. This is only valid for quiet Sun spicules.

It is quite possible that the detection algorithm excludes certain classes of spicules. The detection is better at picking out more isolated spicules, as they have larger gradients and the short spicules are removed with the length threshold. This means that the properties measured here should not be measured as *the* properties of spicules.

There are many details concerning the type II spicules that are still unknown. For instance what the regional differences of the properties are in the quiet Sun, active regions and coronal holes, what the change of the properties along the length of the spicules are and what the time-dependence of the physical properties are.

On-disk, the red-shifted spicules detected were mostly from the quiet Sun, while the blue-shifted spicules were from both the quiet Sun and from the active region. From the small differences seen between the red and blue-shifted on-disk spicules we found the following indications:

- Quiet Sun spicules appear narrower than active region spicules.
- Quiet Sun spicules appear to have a higher Doppler velocity than active region spicules.
- Quiet Sun spicules and active region spicules appear to have the same average Doppler width.

Regional differences are mentioned by De Pontieu et al. (2007b), in particular that spicules from the quiet Sun have shorter lifetimes and longer lengths as compared to spicules from active regions. In order to investigate if spicules have different properties depending on the region, one should study many different regions on different locations on the Sun, from the limb to the disk center. The change of location is important to determine the effect of the curvature of the Sun and possible radiation transfer effects on the properties due to line-of-sight effects.

The change of the width, Doppler velocity and Doppler width along the length of the spicules were briefly studied in this thesis. The results showed that the expectation values for the changes are close to zero. These results are not conclusive due to a number of reasons: the change was measured on spicules from different parts of their temporal evolution, the procedure for obtaining the spicule spectra at each pixel is crude, and within the Doppler statistics the spicules with unresolved spectra are not removed from the statistics creating an artificial correlation in the data. In order for these measurements to become more conclusive, the spicules with a close neighbor should not be included and a larger spectral range is needed. The symmetry of the width profiles is an indication of that a spicule has a close neighbor, but this is maybe not the case for all.

To study the time dependence of the physical properties on a large sample of spicules, one should improve the detection algorithm. A suggestion for a new algorithm is to use a combination of two detection algorithms, each with its own purpose. The current algorithm can be used to locate spicules in the images and another algorithm can use that as input to perform a new detection in the close vicinity of the detected spicules, and in a range of time steps around the detected spicule. This will search out the detected spicule in the time steps before and after it was detected with the current algorithm. Another suggestion is to search for bright areas in the images in

addition to searching for gradients in the image. Verification tests can then be performed on the spectra of the pixels inside the bright areas to search for absorption in one of the wings. This algorithm can possibly be adapted to search out the "black beads" briefly studied in Rouppe van der Voort et al. (2009). The black beads are roundish darkenings found in images from the spectral line wing with many similar characteristics as RBEs, except the visual appearance. This led the authors to the idea that these round darkenings are RBEs moving in direction of the observer. Some of the black beads are probably detected in the current algorithm, but are discarded due to their short length after thinning is applied.

It has become evident in the recent years that the sudden fading of the type II spicules are due to heating (De Pontieu et al., 2011). It is not clear which mechanisms that heats the spicules or how it happens. By studying in detail how the spicules fade can give valuable hints on how the spicules are heated. The spicules often disappear between two or three consecutive time steps, which means that the cadence of the observations analyzed in this thesis of 6.4 s, is not sufficient to resolve the exact nature of the fading. To increase the cadence, the number of spectral positions in the CRISP scan must be reduced. A proposed scanning sequence, to maximize the cadence, is to scan H$\alpha$ at three spectral positions, for instance with the offsets from line center as: [$-1.2$ Å, 0, $+1.2$ Å]. The wing positions are on opposite sides in order to construct the Doppler images to perform the detection on. The theoretical cadence of this sequence is 0.8 s. Its disadvantage is that a full spectrum is not obtained. A compromise between the fast scanning sequence and the scan used in this thesis, is a scan with less spectral positions close to the line center. These spectral positions remained mostly unused in this thesis. The scan range should be increased to about $\pm 1.6$ Å, and possibly even more, to fully resolve faster spicules. By having for instance 6 positions in the wings, from $|1.6|$ Å to $|0.6|$ Å the theoretical cadence of a scan is 3 s. The 6 positions in the wings, coupled with fitting a Gaussian curve, can provide a sufficiently accurate spicule spectrum to deduce the Doppler velocities and Doppler widths from. This can further be optimized for red or blue-shifted spicules by only having 6 positions in one wing and one in the opposite wing. This sequence has a theoretical cadence of 1.5 s and at the same time it obtains the spectra for spicules.

Recently, Judge et al. (2011) proposed a new theory saying that some populations of spicules and fibrils corresponds to warps in 2D sheet-like structures. This is an alternative theory to the conventional picture of mass-flow in tube-like structures. If true, this theory can have profound consequences for the established models of the solar atmosphere. However, the theory is untested both observationally and in advanced simulations and the results from this thesis support the conventional picture of spicules. With

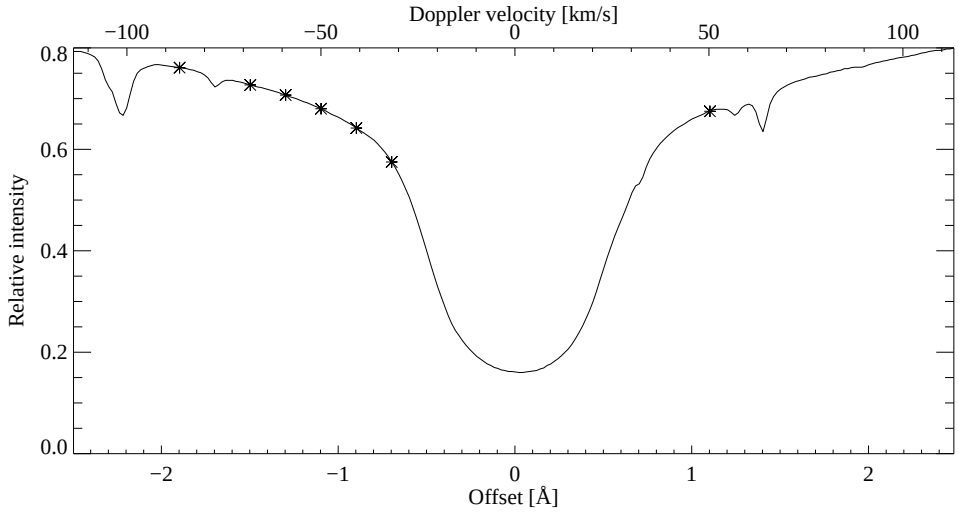


**Figure 5.1:** A proposed fast scanning sequence with CRISP to obtain spicule spectra and resolve the fading of spicules in more detail.

the discovery of a possible new driving mechanism for type II spicules by Martínez-Sykora et al. (2010), it is clear that the chapter on spicules is not finished, and much work remain in order to fully understand their nature and role in the solar atmosphere. Both new observations and numerical simulations will be an essential part in unraveling the mysteries concerning type II spicules.

# Bibliography


Anan, T. et al.: 2010, "Spicule Dynamics over a Plage Region", *PASJ* **62**, 871–

Ardeberg, A.: 1984, "Observatorio del Roque de LOS Muchachos - The Swedish experience", in A. Ardeberg & L. Woltjer (Ed.), *European Southern Observatory Conference and Workshop Proceedings*, Vol. 18 of *European Southern Observatory Conference and Workshop Proceedings*, 73–93

Athay, R. G., and T. E. Holzer: 1982, "The role of spicules in heating the solar atmosphere", *Astrophys. J.* **255**, 743–752

Beckers, J.: 1968, "Solar Spicules", *Sol. Phys.* **3**, 367–433

Beckers, J. M.: 1964, *Ph.D. thesis*, University of Utrecht

Bjølseth, S.: 2008, "Spicules",, *Master's thesis*, University of Oslo

Cavallini, F.: 2006, "IBIS: A New Post-Focus Instrument for Solar Imaging Spectroscopy", *Sol.Phys.* **236**, 415–439

De Pontieu, B., R. Erdélyi, and S. P. James: 2004, "Solar chromospheric spicules from the leakage of photospheric oscillations and flows", *Nature* **430**, 536–539

De Pontieu, B., V. H. Hansteen, L. Rouppe van der Voort, M. van Noort, and M. Carlsson: 2007a, "High-Resolution Observations and Modeling of Dynamic Fibrils", *ApJ* **655**, 624–641

De Pontieu, B. et al.: 2007b, "A Tale of Two Spicules: The Impact of Spicules on the Magnetic Chromosphere", *PASJ* **59**, 655–

De Pontieu, B. et al.: 2011, "The Origins of Hot Plasma in the Solar Corona", *Science* **331**, 55–

Edlén, B.: 1941, *Ark. Mat. Astr. Och. Fys* **28B**, No. 1

Edlén, B.: 1942, *Z. Astrophys* **22**, 30

Grotrian, W.: 1939, *Naturwissen* **27**, 214

Handy, B. N. et al.: 1999, "The transition region and coronal explorer", *Sol.Phys.* **187**, 229–260

Hansteen, V. H., B. De Pontieu, L. Rouppe van der Voort, M. van Noort, and M. Carlsson: 2006, "Dynamic Fibrils Are Driven by Magnetoacoustic Shocks", *ApJ* **647**, L73–L76

Judge, P. G., A. Tritschler, and B. Chye Low: 2011, "Thermal Fine Structure and Magnetic Fields in the Solar Atmosphere: Spicules and Fibrils", *Astrophys. J. Lett.* **730**, L4

Kosugi, T. et al.: 2007, "The Hinode (Solar-B) Mission: An Overview", *Sol.Phys.* **243**, 3–17

Langangen, Ø., M. Carlsson, L. Rouppe van der Voort, V. Hansteen, and B. De Pontieu: 2008a, "Spectroscopic Measurements of Dynamic Fibrils in the Ca II $\lambda$8662 Line", *Astrophys. J.* **673**, 1194–1200

Langangen, Ø. et al.: 2008b, "Search for High Velocities in the Disk Counterpart of Type II Spicules", *Astrophys. J. Lett.* **679**, L167–L170

Langangen, Ø., L. Rouppe van der Voort, and Y. Lin: 2008c, "Measurements of Plasma Motions in Dynamic Fibrils", *Astrophys. J.* **673**, 1201–1208

Martínez-Sykora, J., V. Hansteen, and F. Moreno-Insertis: 2010, "On the origin of the Type˜{\sc ii} spicules - dynamic 3D MHD simulations", *ArXiv e-prints*

Neckel, H., and D. Labs: 1984, "The solar radiation between 3300 and 12500 A", *Sol.Phys.* **90**, 205–258

Nishizuka, N., T. Nakamura, T. Kawate, K. A. P. Singh, and K. Shibata: 2011, "Statistical Study of Chromospheric Anemone Jets Observed with Hinode/SOT", *Astrophys. J.* **731**, 43–

Ostlie, D. A., and B. W. Carroll: 1996, *An Introduction to Modern Stellar Astrophysics*, Pearson Addison Wesley

Parker, E. N.: 1958, "Dynamics of the Interplanetary Gas and Magnetic Fields.", *Astrophys. J.* **128**, 664–

Pasachoff, J. M., W. A. Jacobson, and A. C. Sterling: 2009, "Limb Spicules from the Ground and from Space", *Sol.Phys.* **260**, 59–82

Pneuman, G. W., and R. A. Kopp: 1978, "Downflow in the supergranulation network and its implications for transition region models", *Sol.Phys.* **57**, 49–64

Rouppe van der Voort, L., J. Leenaarts, B. De Pontieu, M. Carlsson, and G. Vissers: 2009, "On-disk Counterparts of Type II Spicules in the Ca II 854.2 nm and H$\alpha$ Lines", *ApJ* **705**, 272–284

Rouppe van der Voort, L. H. M., B. De Pontieu, V. H. Hansteen, M. Carlsson, and M. van Noort: 2007, "Magnetoacoustic Shocks as a Driver of Quiet-Sun Mottles", *Astrophys. J. Lett.* **660**, L169–L172

Rutten, R. J.: 2007, "Observing the Solar Chromosphere", in P. Heinzel, I. Dorotovič, & R. J. Rutten (Ed.), *The Physics of Chromospheric Plasmas*, Vol. 368 of *Astronomical Society of the Pacific Conference Series*, 27–

Rutten, R. J. et al.: 2004, "The Dutch Open Telescope on La Palma", in A. V. Stepanov, E. E. Benevolenskaya, & A. G. Kosovichev (Ed.), *Multi-Wavelength Investigations of Solar Activity*, Vol. 223 of *IAU Symposium*, 597–604

Scharmer, G. B.: 2006, "Comments on the optimization of high resolution Fabry-Pérot filtergraphs", *A&A* **447**, 1111–1120

Scharmer, G. B., K. Bjelksjö, T. K. Korhonen, B. Lindberg, and B. Petterson: 2003a, "The 1-meter Swedish solar telescope", in S. L. Keil & S. V. Avakyan (Ed.), *Society of Photo-Optical Instrumentation Engineers (SPIE) Conference Series*, Vol. 4853 of *Presented at the Society of Photo-Optical Instrumentation Engineers (SPIE) Conference*, 341–350

Scharmer, G. B., P. M. Dettori, M. G. Löfdahl, and M. Shand: 2003b, "Adaptive optics system for the new Swedish solar telescope", in S. L. Keil & S. V. Avakyan (Ed.), *Society of Photo-Optical Instrumentation Engineers (SPIE) Conference Series*, Vol. 4853 of *Presented at the Society of Photo-Optical Instrumentation Engineers (SPIE) Conference*, 370–380

Scharmer, G. B., P. M. Dettori, M. G. Löfdahl, and M. Shand: 2003c, "Adaptive optics system for the new Swedish solar telescope", in S. L. Keil & S. V. Avakyan (Ed.), *Society of Photo-Optical Instrumentation Engineers (SPIE) Conference Series*, Vol. 4853 of *Presented at the Society of Photo-Optical Instrumentation Engineers (SPIE) Conference*, 370–380

Secchi, P.: 1877, *Le Soleil, Gauthiers-Villars, Paris* **2**, Ch. II

Starck, J., F. D. Murtagh, and A. Bijaoui: 1998, *Image Processing and Data Analysis*, Cambridge University Press

Sterling, A. C.: 2000, "Solar Spicules: A Review of Recent Models and Targets for Future Observations - (Invited Review)", *Sol.Phys.* **196**, 79–111

Stix, M.: 2004, *The Sun : An Introduction*, Springer

Tavabi, E., S. Koutchmy, and A. Ajabshirizadeh: 2011, "A statistical analysis of the SOT-Hinode observations of solar spicules and their wave-like behavior", *New Astronomy* **16**, 296–305

Tsuneta, S. et al.: 2008, "The Solar Optical Telescope for the Hinode Mission: An Overview", *Sol.Phys.* **249**, 167–196

Tziotziou, K.: 2007, "Chromospheric Cloud-Model Inversion Techniques", in P. Heinzel, I. Dorotovič, & R. J. Rutten (Ed.), *The Physics of Chromospheric Plasmas*, Vol. 368 of *Astronomical Society of the Pacific Conference Series*, 217–

van Noort, M., L. Rouppe van der Voort, and M. G. Löfdahl: 2005, "Solar Image Restoration By Use Of Multi-frame Blind De-convolution With Multiple Objects And Phase Diversity", *Sol.Phys.* **228**, 191–215

van Noort, M., and L. H. M. Rouppe van der Voort: 2008, "Stokes imaging polarimetry using image restoration at the Swedish 1-m solar telescope", *A&A* **489**, 429–440

Vernazza, J. E., E. H. Avrett, and R. Loeser: 1981, "Structure of the solar chromosphere. III - Models of the EUV brightness components of the quiet-sun", *Astrophys. J. Suppl. S.* **45**, 635–725

Withbroe, G. L.: 1983, "The role of spicules in heating the solar atmosphere Implications of EUV observations", *Astrophys. J.* **267**, 825–836